



FACULTÉ DES SCIENCES
DÉPARTEMENT DE PHYSIQUE - UNITÉ DE RECHERCHE CESAM
GROUP FOR RESEARCH AND APPLICATIONS IN STATISTICAL PHYSICS

Droplet dynamics on curved substrates

Dissertation présentée par

JOSÉPHINE VAN HULLE

*en vue de l'obtention du titre de
Docteur en Sciences*

ANNÉE ACADÉMIQUE 2024-2025

Jury Members

Pr. Thierry Bastin	PRESIDENT
Pr. Laurent Dreesen	SECRETARY
Pr. Nicolas Vandewalle	SUPERVISOR
Dr. Eric Opsomer	
Dr. Alexis Duchesne	
Pr. Zhao Pan	

Acknowledgements

Ces années de thèse ont été une aventure autant intellectuelle qu'humaine, rythmée par des découvertes, des défis et des moments précieux. Ce chemin n'aurait pas été le même sans les personnes que j'ai eu la chance de rencontrer et avec qui j'ai partagé cette expérience. Que ce soit par leur soutien, leurs conseils, leur expertise ou simplement leur présence, chacune d'elles a contribué, à sa manière, à l'aboutissement de ce travail. Je tiens à les remercier ici, en espérant n'oublier personne.

First of all, I want to thank each member of my jury, Nicolas Vandewalle, Thierry Bastin, Laurent Dreesen, Eric Opsomer, Alexis Duchesne and Zhao Pan. I feel honored that you accepted the invitation and took the time to read my work. I hope my work meets the expectations.

Un merci tout particulier à mon promoteur, Nicolas Vandewalle, sans qui cette aventure n'aurait pas été possible. Il m'a guidée à travers le monde fascinant des gouttes sur fibres et a toujours été présent pour me conseiller avec pédagogie et patience. Il m'a transmis la passion pour la mécanique des fluides dès ma première année à l'université. Il a continué à éveiller ma curiosité scientifique tout au long de cette thèse de doctorat. Merci de m'avoir fait confiance pour être l'assistante de vos cours. Merci de m'avoir ouvert de belles opportunités, telles que les conférences, le stage de recherche et de m'avoir permis de travailler dans une ambiance stimulante. J'ai appris énormément. Merci !

Durant ce parcours, j'ai eu la chance d'être entourée par une belle équipe de graspiens, bien plus que des collègues, des amis. Merci à Jean et Charlotte, qui m'ont accueillie avec tant de bienveillance dans leur bureau durant mes premières années de doctorat. Merci à Jean pour les histoires au suspense insoutenable, et la liste des "il faudrait que" qui ne désemplit jamais. Merci à Charlotte d'avoir mis de la couleur dans nos vies et pour son sourire communicatif. Merci d'avoir entraîné la troupe dans la découverte des meilleurs restaurants de Liège. Merci à Megan, de m'avoir accueillie dans son bureau pour ma dernière année de thèse. J'ai découvert une belle personne, pleine d'ambition et de passion pour la science. Merci aux crollés du bureau d'à côté, Adrien et Matteo. Merci à Florence, d'avoir partagé avec moi ce parcours universitaire, de la première bac à la dernière année de thèse. Quel plaisir d'avoir découvert ses nombreux talents artistiques. Merci d'être cette acolyte toujours prête à danser et à enchérir dans les idées un peu folles. Merci à Floriane, cette voisine sportive, qui m'a transmis son savoir et guidée avec bi-

enveillance à mes débuts. Merci à Sébastien, un ami de longue date, avec qui les discussions sont toujours passionnantes. Merci d'avoir contribué à ma culture liégeoise. J'espère que mes phrases sont suffisamment courtes. Merci à Ylona, ma partenaire de master avec qui j'ai ensuite eu la chance de partager mes quatre premières années de thèse. Moins merci pour l'initiation au cross fit. Merci mère Noël ! Merci à Stéphane pour le goût de la bonne musique mais surtout pour l'aide précieuse lors des moments de doute, sa curiosité scientifique contagieuse, et ses conseils d'expérimentateur chevronné. Les kroepoeks ont désormais une saveur particulière. Merci à Christophe, au-delà de sa ponctualité légendaire et de sa capacité à nous immerger dans des mondes fantastiques, merci pour les découvertes musicales, les blagues douteuses et son expertise sur les poissons. Merci à Béatrice et Cyril d'avoir égayé les fins de journées. Merci à Thomas et Klette pour les pédantix. Merci à Nicolas de nous aider pour les pédantix. Merci à Galien pour les montages photos mémorables, pour Smaug le dragon et le château gonflable. Merci à Martin pour les "On part à l'aventure...", la légende de la salle de sieste et le vert. Merci à Alexis, mon parrain de physique. Merci à Geoffroy pour les bonjours aux grands sourires. Merci à Eric pour ses coucous en passant et pour ses mélodies qui égayent aussi notre bureau. Merci à l'atelier, Sam, Med, Oli et Mich pour votre aide pratique et toujours disponible. Merci à Chouaib, mon coach sportif. Merci à Martial, David, Nathan, Luisa, Salvatore, Hervé, Jean-Yves, Jacqueline, Anne, Jean-Marc, Christelle, Christine, Alexis, Corby, PX, Julie et Thomas.

Il est venu le temps de remercier la bien grande bande de petits pédestres, Jean, Julie, Luca, Svet, Maxime, Giulia, Guillaume, Antoine, Thomas, Marin, Meriem et Sébastien. Merci de rester à mes côtés même quand retentit le fameux "Alors ouai, je me la raconte"... Un long santé à nos nouveaux ans, nos soirées jeux de société (mais pitié, plus de Galerapagos), à la Bretagne des Covid-dead et tout ce qui nous attend. Merci à mes amies de bancs d'université Lyne et Hélène, je suis heureuse que notre amitié traverse les années. Merci à Félicie, ma cokoteuse préférée pour tous ces souvenirs, des tabliers étudiants en passant par les Disney, la côte d'Opale et les restos mais également les anecdotes croustillantes. Merci à Cathy et Alice, toujours un plaisir de vous revoir notamment pour les marchés de Noël et les coucous au Decath'. Merci à Lara de m'avoir fait découvrir Bruxelles sur 20 km mais surtout d'être cette cousine formidable.

Enfin, je remercie ceux dont le soutien a rendu tout cela possible. Merci à mes parents de m'avoir toujours soutenue, d'avoir été là pour m'aider et m'encourager dans tous mes accomplissements. Je vous suis profondément reconnaissante pour tout ce que vous avez fait pour moi. Merci à Augustin, ce frère au grand coeur, qui n'a de cesse de prouver qu'avec de la ténacité on peut arriver à tout. Merci à mes grands-parents pour tout ce que vous m'avez appris et pour ces beaux souvenirs. Merci à mamie Huguette de toujours prendre soin de nous. Faute de fleurs bleues, j'ai mis des gouttes bleues. Merci à mon parrain, ma marraine, tante Fabienne et tonton Christian pour votre soutien. Merci à ma belle-famille pour son accueil plus que chaleureux, les repas conviviaux et le chaudeau. Enfin, je tiens à remercier celui qui est resté à mes côtés chaque jour de cette thèse. Merci Ben d'avoir supporté avec moi les hauts et les bas. Merci pour ton soutien, ton aide et ton écoute. Tu as le pouvoir d'illuminer mes journées.

Abstract

Understanding the dynamics of droplet motion on curved substrates is crucial for optimizing water collection technologies, particularly in environments where atmospheric water harvesting is essential. This study experimentally investigates the behavior of droplets on various macroscopic structures, including flat surfaces with curved grooves, vertical cylindrical fibers, and conical fibers. Through experimental observations, the research reveals that factors such as convex grooves, fiber twists, gradient radii and pre-existing wetting conditions significantly influence droplet spreading, dynamics and shape transitions. Specifically, droplets within convex grooves spread faster than those in concave ones. The descent of droplets along vertical fibers is characterized by a self-supply mechanism, where the liquid film left behind the droplet contributes to the formation of subsequent droplets. On twisted fibers, droplets follow a helical path governed by the groove geometry. Droplets on conical fibers spontaneously move towards the base of the cone, with their dynamics influenced by their shape. The findings of this work contribute to the design of more efficient substrates for droplet drainage, offering practical applications in the development of optimized fog collectors composed of fiber meshes.

Résumé

Comprendre la dynamique du mouvement des gouttes de liquide sur des substrats courbés est essentiel pour optimiser les technologies de collecte d'eau, en particulier dans les environnements où la récolte de l'eau atmosphérique est primordiale. Cette étude examine expérimentalement le comportement des gouttes sur diverses structures macroscopiques, y compris des surfaces planes avec des rainures courbes, des fibres cylindriques verticales et des fibres coniques. À travers des observations expérimentales, la recherche révèle que des facteurs tels que les rainures convexes, les torsions entre fibres, les rayons croissants et les conditions de mouillage préexistantes influencent significativement l'étalement, la dynamique et les transitions dans la forme des gouttes. En particulier, les gouttes dans les rainures convexes s'évalent plus rapidement que celles dans les rainures concaves. La descente des gouttes le long des fibres verticales se caractérise par un mécanisme d'auto-alimentation, où le film liquide laissé à l'arrière de la goutte contribue à la formation des nouvelles gouttes. Sur les fibres torsadées, les gouttes suivent un chemin hélicoïdal gouverné par la géométrie de la rainure. Les gouttes sur les fibres coniques se déplacent spontanément vers la base du cône, leur dynamique étant influencée par leur forme. Les résultats de ce travail contribuent à la conception de substrats plus efficaces pour le drainage des gouttes, offrant des applications pratiques dans le développement de collecteurs de brouillard optimisés composés de maillages de fibres.

Contents

0	Introduction	1
1	State of the Art	5
1.1	Droplets	5
1.1.1	Surface tension	5
1.1.2	Laplace pressure	7
1.1.3	Rayleigh-Plateau instability	8
1.2	Droplets on a substrate - Statics	9
1.2.1	Wetting and contact angle	9
1.2.2	Bond number	11
1.3	Droplets on a substrate - Dynamics	12
1.3.1	Viscosity	12
1.3.2	Capillary and Weber numbers	13
1.3.3	Spreading dynamics	13
1.3.4	Influence of textures	15
1.4	Droplets on cylindrical fiber	18
1.4.1	Droplet geometries and wetting	18
1.4.2	Fluid coating : Landau-Levich-Derjaguin theory	20
1.4.3	Rayleigh-Plateau instability	21
1.4.4	Liquid film flowing down a fiber	23
1.4.5	Motion of droplet on a fiber	25
1.4.6	Several fibers	26
1.5	Droplets on conical fiber	29
1.5.1	Surface tension imbalance	29
1.6	Water collection	31
1.6.1	Difference between fog and dew	31
1.6.2	Bio-inspiration	32
1.6.3	Fog collectors	35
1.7	Foundations and Launch Pad	39
2	Droplet spreading inside curved grooves	41
2.1	Motivations	42
2.2	Experimental setup	43
2.3	Spreading characterization	45
2.3.1	Hypocycle - concave	45

2.3.2	Epicycle - convex	47
2.3.3	Analysis	48
2.4	Application	49
2.5	Grooved fibers	51
2.6	Conclusion	52
3	Multiple droplets on a cylindrical fiber	53
3.1	Introduction	54
3.2	Methods	55
3.3	Results	56
3.4	Discussion	57
3.4.1	Mother droplet	57
3.4.2	Daughter droplet	60
3.4.3	Granddaughter droplets	64
3.5	Conclusion	66
4	Droplets on twisted cylindrical fibers	69
4.1	Introduction	70
4.2	Experimental section	70
4.3	Results	73
4.4	Discussion	76
4.4.1	Regime I	78
4.4.2	Regime II	79
4.4.3	Analysis	79
4.5	Application: Manipulation and fog collection	80
4.6	Conclusion	82
5	Droplets on a conical fiber	83
5.1	Motivations	84
5.2	Methods	86
5.3	Results	87
5.4	Discussion	88
5.4.1	Barrel shape	90
5.4.2	Clamshell shape	92
5.4.3	Analysis of the models	93
5.5	Discussion: Grooved conical fibers	96
5.6	Application for fog collection	99
5.7	Conclusion	100
6	General conclusion and perspectives	103
6.1	Conclusion	103
6.2	Perspectives	105

Publications

J. Van Hulle, F. Weyer, S. Dorbolo, and N. Vandewalle, *Capillary transport from barrel to clamshell droplets on conical fibers*, Phys. Rev. Fluids **6**, 024501 (2021).

J. Van Hulle, and N. Vandewalle, *Effect of groove curvature on droplet spreading*, Soft Matter **19**, 4669 (2023).

M. Leonard, J. Van Hulle, F. Weyer, D. Terwagne and N. Vandewalle, *Droplets sliding on single and multiple vertical fibers*, Phys. Rev. Fluids **8**, 103601 (2023).

J. Van Hulle, C. Delforge, M. Leonard, E. Follet, and N. Vandewalle, *Droplet helical motion on twisted fibers*, under review (2024).

J. Van Hulle, N. Vandewalle, and Z. Pan, *Multiple droplets on a cylindrical fiber*, In preparation (2024).

Introduction

*"Je t'offrirai des perles de pluie,
venues de pays où il ne pleut pas"*

Jacques Brel

Fresh water is a vital resource for life. It is a treasure that many people are, unfortunately, struggling to access, and global warming is accentuating these discrepancies [1]. Predominant sources of fresh water include rainfall, groundwater and lakes, yet, their availability is diminishing. Consequently, the development of innovative methods for providing fresh water is becoming a crucial challenge. One often overlooked source is atmospheric water, the water naturally present in the air, such as dew or fog. Remarkably, numerous natural examples are supplied with water through moisture, like the one shown in Fig. 0.1. [2]. For instance, every morning, the spider webs are covered with pearls of water [3]. Certain insect-trapping plants, cacti and mosses use their conical hairs or spines to condense water droplets at their tips [4, 5, 6]. In arid deserts, some insects have specialized evolved structures, bumps or spikes, to harvest moisture during specific times of the day [7, 8]. These fascinating natural mechanisms have recently received huge attention and inspired the creation of novel, passive technologies for fog and dew collection. These techniques are demonstrating a promising efficiency of up to ten liters per square meter per day for fog-based techniques [9, 10] and up to 0.1 liter per square meter per night for dew-based techniques [11, 12].

Nature, through selection, has optimized the most effective water collection strategies for each species. Studying the specific traits of plants and animals proficient in dew or fog collection can unveil key features. These biological structures typically involve rough surfaces, textured fibers, and grooved conical fibers. In these systems, one observes a combination of both macroscopic structures like surfaces, fibers, and cones, and microscopic structures like roughness with bumps or grooves.

Current fog and dew condensers mimic these characteristics, employing substrates with roughness or grooves for dew collection, and intertwining meshes or conical structures for fog harvesting [13, 14, 15].

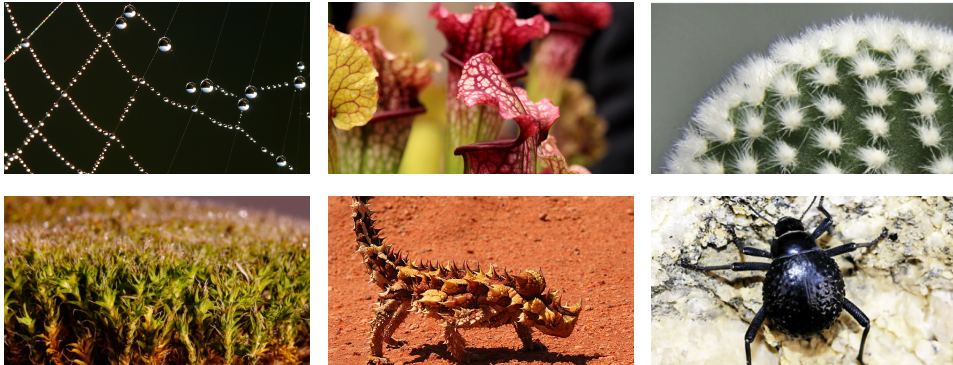


Figure 0.1: Examples of animals and plants achieving water collection from atmospheric water, such as dew and fog. Every morning spider webs are covered with pearls of water (credit: Luc Viatour). Certain species of insect-trapping plants (*Sarracenia*) (credit: Sonja-Kalee), cacti (*Opuntia microdasys*) [16] and mosses (*Syntrichia caninervis*) [6] (credit: Splash Lab) collect water thanks to their conical and grooved hairs. Animals in arid regions such as lizards (*Moloch horridus*) (credit: Bärnas) and beetles (*Stenocara gracilipes*) [16] have textures on their backs that collect and transport water.

This thesis aims to expand our understanding of liquid spreading on both macroscopic structures like fibers and cones, as well as macroscopic substrates decorated with grooves. Understanding the dynamics of droplet spreading is fundamental for improving the efficiency of water collection technologies. By analyzing how droplets interact with various surfaces, one can design more effective methods to direct droplets towards collection points. Efficient drainage is crucial in water collection systems, aiming to maximize the droplet motion to reduce re-entrainment and evaporation.

In this work, we analyze the motion of droplets on three distinct macroscopic structures: flat substrates, vertical fibers, and horizontal cones. For flat substrates, we have characterized droplet spreading within curved grooves. For vertical fibers, we examined both the descending motion of droplets on smooth and grooved fibers. Lastly, for conical fiber, we have described the spontaneous motion of droplets along them. An overview of our achievements in the framework of droplet spreading is highlighted in Fig. 0.2. In this figure, we make divisions between the three main macroscopic structures (substrates, fibers, cones) and the substructures (smooth or grooves). We believe this additional knowledge will humbly contribute to advancing water collection technologies.

The thesis is structured as follows. Chapter 1 provides an exploration of key concepts and a review of previous studies concerning the properties of droplets. In Chapter 2, we focus on the behavior of droplets as they spread within curved grooves etched on flat substrates. In Chapter 3, we investigate droplets on cylindrical fibers, particularly emphasizing the film liquid left behind the moving droplet.

Chapter 4 analyzes the motion of a droplet along a bundle of two twisted fibers. The bundle of two fibers exhibits a grooved substructure. In Chapter 5, one examines the shape and motion of droplets on conical fibers. The thesis closes with a conclusive chapter that not only provides a comprehensive take-home message but also suggests several directions for further research in the field of droplet spreading.

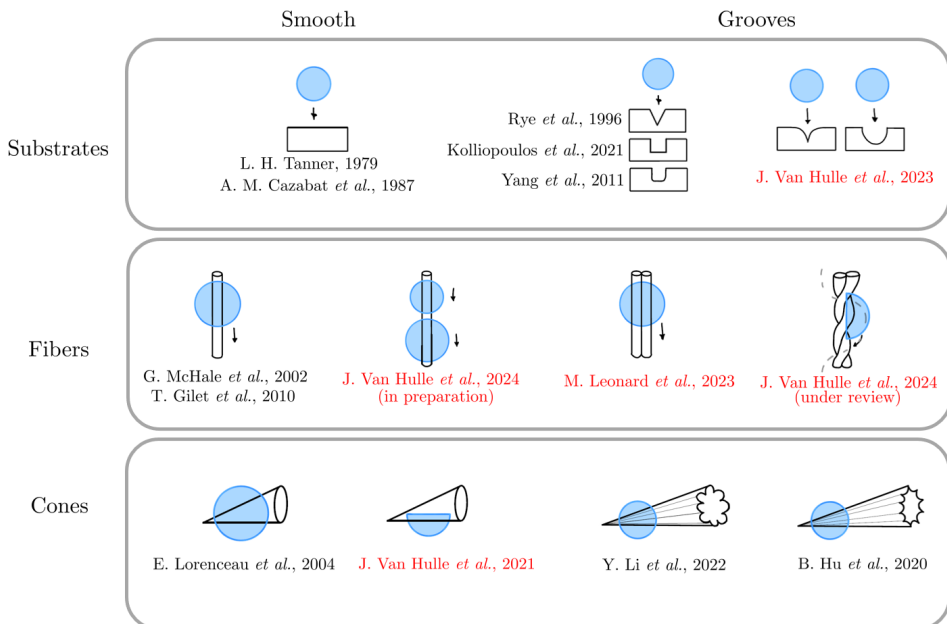


Figure 0.2: Schematic overview of the topics addressed in the thesis. The main study is to focus on droplet spreading on various surfaces. From top to bottom, the geometry of the surface changes. From left to right, a substructure is added on the macroscopic surface. Previous studies are written in black. The red-colored references are our contributions that will be presented in the thesis.

State of the Art

1.1 Droplets

Before studying the behavior of droplets on complex substrates, it is crucial to clarify fundamental concepts about suspended droplets in the air. For example, a droplet suspended in a gas is like a raindrop falling from the sky. The droplet maintains a spherical shape as long as the wind gently blows [17]. This spherical shape results from the surface tension acting along the droplet's surface.

1.1.1 Surface tension

A suspended droplet constitutes a small amount of liquid surrounded by gas, as depicted in Fig. 1.1. It establishes a boundary between the two immiscible phases, liquid and gas, which defines a liquid-gas interface. The interface behaves like a tensioned membrane that prevents any surface deformations of the spherical droplet. The surface tension property of the interface can be explained from both a thermodynamical and a mechanical point of view.

Thermodynamical point of view The origin of surface tension lies at the microscopic level. In a liquid droplet, a molecule located deep within the bulk is symmetrically surrounded by neighboring molecules. Conversely, a molecule near the interface encounters nearly half the number of interactions compared to its counterpart in the bulk of the fluid. This reduction in neighboring molecules results in an uneven distribution of interactions around the molecule, as depicted in Fig. 1.2 [18]. The figure illustrates both attractive and repulsive forces acting on a molecule in the bulk and at the interface. Attractive forces exert over longer ranges, while repulsive forces, isotropic in nature, operate over shorter distances. In the bulk, balanced forces emerge due to the symmetric molecular density surrounding

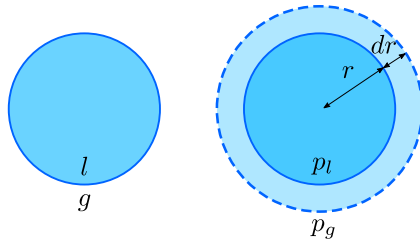


Figure 1.1: (left) A suspended liquid (l) droplet in a gas phase (g). The boundary between the two immiscible phases is called the liquid-gas interface. (right) A suspended droplet with an increased radius r by dr . The pressure in the liquid phase is denoted p_l and the pressure in the gas phase is p_g .

each molecule. Conversely, at the interface, molecules experience an asymmetric distribution of neighbors, leading to higher energy levels compared to those within the bulk. Consequently, any deformation that enlarges the surrounding surface area of the droplet results in an increase in its energy.

Expanding the surface area A by a small increment dA , and consequently increasing the volume V by an amount dV , necessitates a work δW [19]. This work is given by

$$\delta W = \gamma dA - p_l dV_l - p_g dV_g, \quad (1.1)$$

where γ is the surface tension at the liquid/gas interface, p_g and p_l represent the pressures in the gas and liquid phases respectively. dV_l is the incremental change in the liquid's volume and dV_g refers to the decrease in the surrounding gas volume. The first term describes the work needed to increase the droplet's surface, while the latter two terms describe the work needed to modify the droplet's volume. The work brought to the system is similar to an increase in the system's free energy F at a given temperature T , containing N particles. This leads to

$$\gamma = \left(\frac{\partial F}{\partial A} \right)_{T,N}, \quad (1.2)$$

for a droplet of surface A that surrounds a volume V , this is the thermodynamic description of the surface tension. The units of γ are J/m^2 , representing the energy necessary to increase the surface of one unit. Minimization of energy drives the suspended droplet to adopt a spherical shape, which is the minimum surface area for a given volume.

Mechanical point of view Returning to the microscopic viewpoint, molecules positioned at the interface undergo a scarcity of neighboring molecules. In the vertical direction, the attractive interaction precisely offsets the repulsive interaction, as depicted in Fig. 1.2. However, in the horizontal direction, the attractive force is larger than the isotropic repulsive force which maintains a similar magnitude to that in the vertical direction [18]. The balance generates a resultant attractive force per unit length at the liquid interface, known as surface tension.

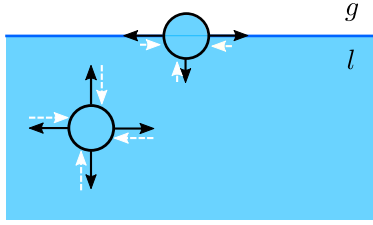


Figure 1.2: Sketch depicting two liquid molecules. Solid black arrows represent attractive forces, while dotted white arrows indicate repulsive forces. Molecules within the bulk experience balanced attractive and repulsive forces. However, molecules near the interface encounter a scarcity of neighboring liquid molecules, resulting in higher energy levels compared to bulk molecules (thermodynamic approach). Additionally, this deficit induces a horizontal force component (mechanical approach).

Expressing the work required to increase the droplet's surface expressed in Eq. (1.1) as a function of the radius r increased by dr , with $dA = 8\pi r dr$ and $dV = 4\pi r^2 dr$ while $dV_g = -dV_l$, yields

$$\delta W = 8\pi r \gamma dr + 4\pi r^2 (p_g - p_l) dr. \quad (1.3)$$

This equation describes the work done by the capillary force (first term) and the pressure force (second term) [19]. The work done by the capillary force can be rewritten as $F_\gamma dr$ with F_γ the surface tension force, one has $F_\gamma = 8\pi r \gamma = \gamma L$ and L the length on which this force apply. One can rewrite surface tension as

$$\gamma = \frac{F_\gamma}{L}, \quad (1.4)$$

and conclude that surface tension is also a force per unit of length.

1.1.2 Laplace pressure

For a spherical droplet, there is a pressure difference across the interface due to surface tension. The equilibrium condition implies $\delta W = 0$. Therefore Eq. (1.3), that describes the incremental work necessary to increase the radius r of a spherical droplet by dr , becomes

$$\Delta p = p_l - p_g = 2 \frac{\gamma}{r}. \quad (1.5)$$

The pressure difference is higher in smaller droplets. A generalized form of this expression is provided by,

$$\Delta p = \gamma \left(\frac{1}{r_1} + \frac{1}{r_2} \right) \quad (1.6)$$

where r_1 and r_2 are the principal radii of curvature of the surface. This relationship is known as the Laplace pressure law [19, 20].

1.1.3 Rayleigh-Plateau instability

We now explore the Rayleigh-Plateau instability, a crucial phenomenon that influences the shape adopted by liquid [21, 22]. When using tap water, the resulting flow rate determines whether a continuous cylinder of water (at high flow rates) or a series of small suspended water droplets (at low flow rates) is formed, as illustrated in Fig. 1.3.

This instability is ruled by the minimization of surface area. To examine the surface evolution between a cylinder and a series of beads, consider a cylinder of water with a radius R and a length L . Then, using the same amount of liquid, create a succession of n spherical droplets each with a radius r . With the volume conservation, one can express this relationship as

$$\pi R^2 L = \frac{4}{3} \pi r^3 n. \quad (1.7)$$

The ratio of the surface area of n beads A_b to the surface area of the cylinder A_c is given by

$$\frac{A_b}{A_c} = \frac{n 4 \pi r^2}{2 \pi R L} = \frac{3R}{2r} \quad (1.8)$$

using Eq. (1.7). Thus, when

$$\frac{3R}{2r} < 1, \quad (1.9)$$

the cylinder becomes unstable and breaks into a series of small water droplets due to surface area minimization [19].

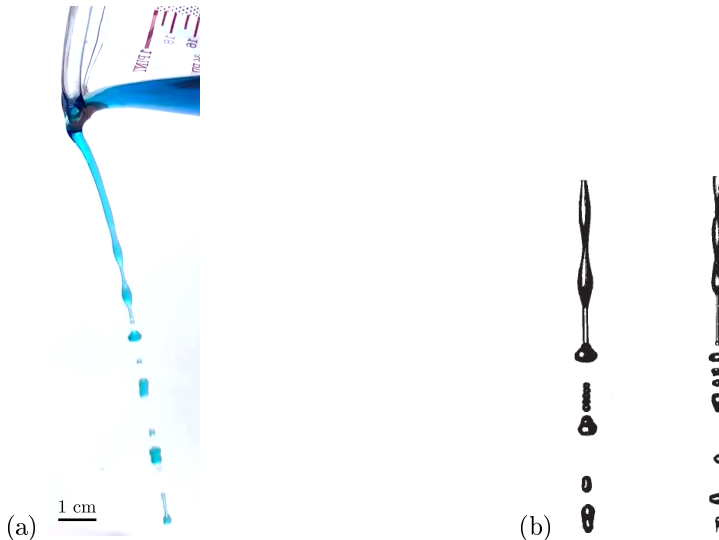


Figure 1.3: (a) Picture of poured blue dyed water that destabilizes from a cylinder flow to a succession of water beads flow (credit: J. Van Hulle). This is the Rayleigh-Plateau instability. (b) Pictures of Lord Rayleigh. Taken from [23].

1.2 Droplets on a substrate - Statics

During rainfall, raindrops impact solid surfaces, like plant leaves or windows, creating droplets on these substrates. The morphology of a droplet on a substrate depends on the properties of the substrate.

1.2.1 Wetting and contact angle

A droplet on a substrate can exhibit either complete or partial spreading on the surface. The spreading parameter, denoted S , defines the energy difference between a dry substrate and a wetted substrate, represented as

$$S = \gamma_{sg} - (\gamma_{ls} + \gamma), \quad (1.10)$$

with γ_{sg} , γ_{ls} and γ the surface tension between different interfaces, respectively, solid/gas, liquid/solid, and finally liquid/gas. When the spreading parameter is positive or zero, the liquid droplet tends to spread entirely to minimize its energy, resulting in a liquid film formation with a pancake surface shape [24]. However, if S is negative, the droplet minimizes its energy by forming a spherical cap. The droplet depicts a contact angle θ at the meeting with the substrate. If the contact angle θ is smaller than 90° , the surface is qualified as wettable. For contact angles larger than 90° , the substrate is categorized as non-wettable, and the droplet adopts a nearly perfect spherical shape. In the case of water, a wettable surface is termed hydrophilic, while a non-wettable surface is called hydrophobic. All these different wetting are depicted in Fig. 1.4.

The contact angle is the result of all surface tensions between the solid and gas, liquid and gas, liquid and solid. One defines the contact line as the fictive boundary where all three phases meet. Balancing the various surface tensions acting upon it results in

$$\gamma \cos(\theta) = \gamma_{sg} - \gamma_{ls}. \quad (1.11)$$

This equation defines a unique contact angle, the equilibrium contact angle, determined by the properties of the liquid and the substrate, assuming the substrate is perfectly smooth. However, experimental observations reveal varying contact angles due to substrate roughness and the method of droplet deposition.

Consider a substrate with defects and a droplet placed upon it, as in Fig. 1.5 (a). By tilting the substrate at the maximal inclination without inducing motion of the droplet, two distinct contact angles are observed: (i) the maximal contact angle at the lowest point of the droplet, called the advancing contact angle θ_a , and (ii) the minimal contact angle at the highest point of the droplet, referred to as the receding contact angle θ_r . This situation is sketched in Fig. 1.5 (b). The two angle values define the contact angle hysteresis. This hysteresis occurs because the contact line is pinned to the imperfections (roughness or textures) on the surface of the substrate [25, 26, 27]. This hysteresis effect explains why raindrops can cling to inclined plant leaves or vertical windows without sliding down [28]. As the droplet remains static, the contact angles at both the front and rear of the raindrop are within the range dictated by the contact angle hysteresis and the applied capillary

force is balancing the weight. However, when the contact angle at the front equals θ_A and at the rear equals θ_R , the droplet initiates its descent, as shown in Fig. 1.5 (c) [29].

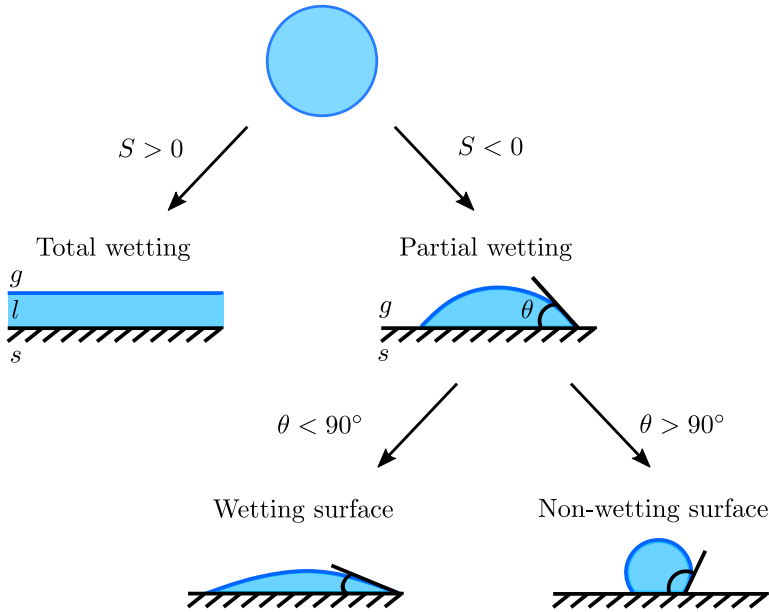


Figure 1.4: A droplet on a substrate either totally wets the surface ($S > 0$), creating a thin film, or partially wets the surface ($S < 0$), forming a spherical cap. In the case of partial wetting, one may encounter two different situations depending on the liquid/solid affinity. If the contact angle is smaller than 90° , the surface is wettable. If the contact is larger than 90° , then the surface is non-wettable.

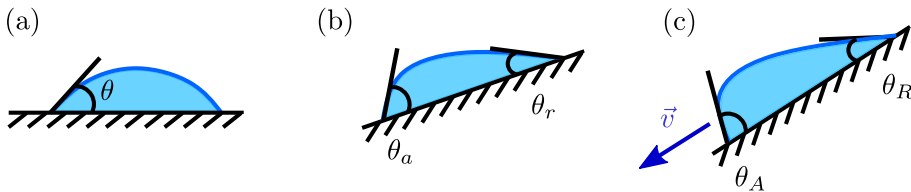


Figure 1.5: (a) A droplet adopting a spherical cap on a substrate. The contact angle is referred to as the equilibrium contact angle. (b) The surface is tilted while keeping the contact line static. In such a configuration, the droplet exhibits two contact angles, the advancing contact angle θ_a and the receding contact angle θ_r . (c) The surface is inclined enough to promote the motion of the droplet with a maximal advancing contact angle θ_A and a minimal receding contact angle θ_R .

1.2.2 Bond number

Until now, gravitational effects have been neglected. However, gravity can significantly influence the shape adopted by a droplet. It is observed that many raindrops eventually form puddles. Particularly, on a non-wettable surface, as the volume of the droplet increases, its shape changes from nearly spherical to a more flattened form resembling a puddle, as shown in Fig. 1.6. In the case of water, the droplet begins to deform when its size exceeds 2.7 mm. This transition occurs when gravitational forces surpass surface tension forces. To characterize this transition, a non-dimensional number called the Bond number (Bo) is defined. This number compares the influence of both forces.



Figure 1.6: Picture of two blue-dyed water droplets on a hydrophobic solid surface (credit: J. Van Hulle). (left) A small volume, $\Omega = 3 \mu\text{l}$, adopts a spherical shape ($\text{Bo} < 1$). (right) A larger volume, $\Omega = 500 \mu\text{l}$, adopts a puddle-like shape ($\text{Bo} > 1$).

Dimensionless numbers serve to compare the relative importance between two quantities. They are dimensionless ratios aiding in discerning dominant or negligible quantities within a phenomenon. When the ratio approaches 1, both quantities bear significant importance in the observed phenomenon. In our context, three dimensionless numbers are defined: the Bond number, the capillary number, and the Weber number. The Bond number is described here under while the capillary and Weber numbers are defined in the next section after the introduction of liquid velocity and viscosity.

The Bond number, Bo , represents the competition between gravitational and surface tension effects. The Bond number is expressed as

$$\text{Bo} = \frac{\rho g r^2}{\gamma} = \frac{\text{Gravity}}{\text{Surface tension}}, \quad (1.12)$$

where ρ is the liquid density, g is the gravitational acceleration and r stands for the characteristic length of the system. A droplet exhibiting a spherical shape corresponds to a Bo smaller than 1, indicating surface tension dominance over gravity, as it is the case in Fig. 1.6 (left). Conversely, a droplet with a flattened shape possesses a Bo larger than 1, signifying gravity overcoming surface tension, see Fig. 1.6 (right). At the transition point where both effects are equivalent, one defines the capillary length as

$$l_c = \sqrt{\frac{\gamma}{\rho g}}. \quad (1.13)$$

For water, the capillary length is 2.7 mm. Therefore, any droplet with a characteristic length r smaller than l_c adopts a spherical shape.

1.3 Droplets on a substrate - Dynamics

We transition from discussing static droplets to exploring the dynamics of droplet spreading on a substrate. In this section, we introduce the concept of fluid viscosity, the capillary and Weber numbers, along with spreading dynamics on both smooth and textured substrates.

1.3.1 Viscosity

When a fluid is in motion, it dissipates energy due to friction between its different layers, a property known as viscosity. A straightforward analogy illustrating viscosity is the comparison between water and honey. Honey exhibits higher internal friction between its layers compared to water. Consequently, when subjected to the same external force (such as tilting a spoon), honey flows more slowly than water. Let's give a quantitative definition of the viscosity by examining two adjacent fluid layers moving relative to each other, as illustrated in Fig. 1.7. Assuming the top layer moves faster, it exerts a force F on the bottom layer. According to Newton's third law, the bottom layer exerts an equal force F' with an opposite direction on the top layer, tending to slow it down. A force F acting tangentially on a surface A defines shear stress, $\tau = F/A$. This stress is proportional to the gradient velocity, we have

$$\tau = \eta \frac{\partial v}{\partial z}, \quad (1.14)$$

where η is the dynamic viscosity [30]. It leads to a quantitative expression for the dissipating force due to viscosity,

$$F = A\eta \frac{\partial v}{\partial z}. \quad (1.15)$$

Alternatively, instead of the dynamical viscosity η , kinematic viscosity ν can be defined as the ratio of the dynamical viscosity to density ρ ,

$$\nu = \frac{\eta}{\rho}. \quad (1.16)$$

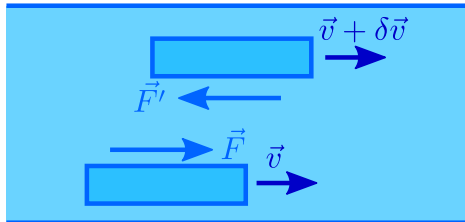


Figure 1.7: Illustration of two adjoining liquid layers interacting and inducing dissipation in the fluid flow. The upper layer moves faster than the lower one and tends to pull the lower layer with it through a force F exerted on the lower layer. Consequently, the lower layer tends to slow the upper layer with an equal and opposite force $\vec{F}' = -\vec{F}$ on the upper layer.

1.3.2 Capillary and Weber numbers

In the case of moving droplets, two new physical quantities play important roles, the viscosity and the speed. One can define several non-dimensional numbers comparing surface tension effects to viscous effects or inertial ones.

The capillary number, Ca , assesses the ratio of viscous effects to surface tension effects and is expressed as

$$Ca = \frac{\rho\nu v}{\gamma} = \frac{\text{Viscosity}}{\text{Surface tension}}, \quad (1.17)$$

where ν is the kinematic viscosity and v is the speed of the system. When Ca is less than 1, surface tension overcomes dissipation caused by viscosity.

The Weber number, We , compares inertial to surface tension forces. It is defined as

$$We = \frac{\rho r v^2}{\gamma} = \frac{\text{Inertia}}{\text{Surface tension}}, \quad (1.18)$$

where r stands for the characteristic length of the system. In both previous non-dimensional numbers, the speed of the droplet is used. For instance, a falling droplet with a small Weber number keeps a spherical shape while it bursts creating smaller droplets when the Weber number is higher [31]. One will continue the State of the Art with the case of the dynamical spreading of droplets on substrates.

1.3.3 Spreading dynamics

When a droplet is deposited on a surface, it initially undergoes a spreading process before attaining its equilibrium shape described previously. During this phase, the droplet spreads along the surface with a circular contact line. In cases where wetting is complete ($S > 0$), the droplet continues to spread until it forms a thin liquid film that covers the substrate. In such instances, the contact angle decreases gradually, eventually approaching the equilibrium value of $\theta \rightarrow 0$. The contact angle associated with a moving contact line is termed the dynamical contact angle, denoted as θ_D . A spreading droplet is depicted in Fig. 1.8 (a). We consider a small droplet, meaning that the Bond number is smaller than the unity, thus gravity is neglected. In such a case, the dynamical contact angle evolves with time following a relationship expressed as

$$\theta_D \sim t^{-3/10}. \quad (1.19)$$

Additionally, as the dynamical contact angle decreases, the radius r of the droplet increases, as shown in Fig. 1.8 (a), following this scaling [32]

$$r \sim t^{1/10}. \quad (1.20)$$

These scalings can be explained by considering the forces acting on the contact line. In case of total wetting, a precursor film forms ahead of the observable contact line [27, 33]. This precursor film was observed through an ingenious experiment by Hardy in 1919 [19, 34]. He utilized a thin glass stick, positioned at equilibrium with a finite angle on the substrate, solely supported by the friction between the

solids. When a droplet was deposited nearby, he noted that the stick fell before the observable contact line arrived. This precursor film exists upstream of the contact line and it has a sub-micron range thickness [33, 35]. The precursor film can be observed and studied thanks to ellipsometry, interferometry or other microscopy techniques (electron microscopy, polarized reflection microscopy) [36], it establishes first with an adiabatic rate ($\sim t$) at short times and then with a diffusive rate ($\sim \sqrt{t}$) at later times [37, 38]. As a result, the droplet spreads not on the solid substrate directly, but rather on its own precursor film [39]. The driving force per unit length on the contact line is therefore

$$f_\gamma = \gamma - \gamma \cos \theta_D \approx \gamma \frac{\theta_D^2}{2}. \quad (1.21)$$

Opposing the driving force is the dissipation force caused by the fluid's viscosity f_η (per unit length). The main dissipation occurs in the liquid wedge of contact angle θ_D , sketched in Fig 1.8 (b). The contact line of the droplet moves with a velocity U . The total power loss per unit length is given by [40]

$$P_{loss} = f_\eta U = \int_0^\infty dx \int_0^\zeta dz \eta \left(\frac{dv}{dz} \right)^2. \quad (1.22)$$

The velocity profile in the wedge, as sketched in Fig. 1.8 (b), is described with

$$v_x(z) = \frac{3}{2} \frac{U}{\zeta^2} (-z^2 + 2\zeta z), \quad (1.23)$$

where ζ is a given thickness in the wedge and is expressed as $\zeta = \theta_D x$. The theoretical development leading to this expression is detailed in Appendix A. Consequently, the power loss is rewritten as

$$P_{loss} = 3\eta \frac{U^2}{\theta_D} \int_0^\infty \frac{1}{x} dx, \quad (1.24)$$

However, this integral diverges. To solve this issue, two cutoff lengths need to be introduced [40]. The maximum value taken by x is the size of the droplet L and the smallest value is the molecular size a . This leads to an expression for the dissipation force per unit length

$$f_\eta = 3\eta \frac{U}{\theta_D} \Gamma, \quad (1.25)$$

with $\Gamma = \ln\left(\frac{L}{a}\right)$. Hoffman showed that Γ is of the order of 15 when the liquid spreads on a dry surface [41], whereas Bico and Qu  r   found that Γ is of the order of 5 when the liquid spreads on a wet surface [42]. Balancing both forces yields the speed U of the moving contact line,

$$U = \frac{1}{6\Gamma} \frac{\gamma}{\eta} \theta_D^3, \quad (1.26)$$

which can be rewritten by considering the droplet's volume conservation,

$$U \sim \frac{\gamma}{\eta} \frac{\Omega^3}{r^9}. \quad (1.27)$$

In fact, the shape of the droplet is a spherical cap whose volume is $\Omega \sim r^2 h$ and the contact angle is $\theta_D \sim h/r$, leading to $\theta_D \sim \Omega/r^3$ [43]. Finally, solving Eq. (1.27), leads to

$$r(t) \sim \Omega^{3/10} \left(\frac{\gamma}{\eta} t \right)^{1/10}. \quad (1.28)$$

This is the spreading equation of a totally wetting droplet, known as Tanner's equation [44]. Consequently, the dynamical contact angle given by $\theta_D \sim \Omega/r^3$ leads to

$$\theta_D \sim \Omega^{1/10} \left(\frac{\gamma}{\eta} t \right)^{-3/10}. \quad (1.29)$$

The exact expression of Tanner's law is

$$r(t) = r_0 \left(1 + \frac{40}{\pi^3 r_0^{10}} \frac{\gamma}{\eta} \Omega^3 t \right)^{1/10}. \quad (1.30)$$

with r_0 the radius at the initial time [45].

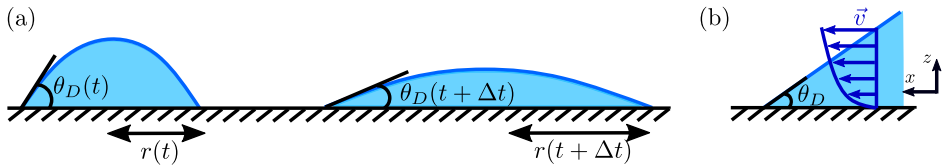


Figure 1.8: (a) Illustration of a droplet spreading on a substrate. As the droplet spreads, the radius increases and the dynamical contact angle decreases. The precursor film is not represented in this illustration. (b) Advancing corner of fluid with a dynamical contact angle θ_D . The velocity profile v of the fluid layers is parabolic according to Eq. (1.23).

The spreading described above is governed by capillary forces and bulk dissipation. However, the scaling can vary with the dominant driving and dissipative forces. In situations where gravitational forces surpass capillary influences, the spreading follows a scaling power of $1/8$ [46]. Additionally, an alternative dissipation mechanism to the previously mentioned bulk dissipation could be significant, specifically, dissipation at the contact line. When contact line dissipation overcomes bulk dissipation, while still capillarity-driven, the spreading dynamics have a scaling exponent of $1/7$ [38].

1.3.4 Influence of textures

Enhancing the spreading rate of a droplet can be achieved by incorporating grooves into the surface, which confines the droplet within the groove, thereby reducing its contact area with the surface. This modified spreading behavior can exhibit different temporal power laws, influenced by the specific geometry of the grooves [47]. The utilization of textured surfaces, including grooves, is a strategy observed in nature and is briefly discussed in the Introduction section, with a more detailed exploration provided in section 1.6.

A closed groove can be described as a cylindrical capillary. When such a capillary tube comes into contact with a liquid reservoir, the liquid rises following a power law

with an exponent $1/2$, i.e. $x \sim t^{1/2}$. This relation is commonly referred to as the Lucas-Washburn equation [48, 49] or the Bell-Cameron-Lucas-Washburn (BCLW) equation [50]. In this case, the volume inside the groove is not conserved as it increases as the liquid ascends. To explain this behavior, one considers a cylinder with an inner radius R , the height of the fluid in the capillary is described with z and the fluid has an equilibrium contact angle θ_E . One neglects the weight of the liquid column, this is a valid assumption either at the initial stages of the liquid rise or when the capillary is oriented horizontally. Furthermore, inertial effects are also neglected. Balancing the driving capillary force with the viscous dissipation yields,

$$2\pi R\gamma \cos \theta_E = 8\pi\eta x\dot{x}. \quad (1.31)$$

Therefore one obtains the following dynamics for the rising meniscus

$$x(t) = \left(\frac{1}{2} \frac{\gamma R \cos \theta_E}{\eta} \right)^{1/2} t^{1/2}. \quad (1.32)$$

This diffusive behavior has been observed not only in the invasion from a reservoir of open rectangular grooves [4, 51] and curved grooves [52], but also across a variety of patterned surfaces [53] and micropillars [54, 55, 56]. Subsequently, this diffusive behavior had been extended to dynamics of imbibing porous media going from textiles [57], soils [58] to foams [59]. Moreover, other dynamics were also found. Reyssat [60] showed that in divergent tubes with axial shape variations, the scaling exponent could vary, taking values such as $1/4$, $1/7$, or even $1/10$. Conversely, in certain converging tubes, the exponent can exceed $1/2$ [61]. The influence of gravity on the meniscus shape within a corner leads to a consistent power of $1/3$, regardless of whether the corners are curved [62, 63] or V-shaped grooves [64]. In the context of porous media imbibition, the scaling exponent is a function of the porosity, leading to values smaller than $1/2$ [65]. Additionally, other textured surfaces showed a scaling power of $1/3$, as evidenced in the study of Obara *et al.* [66].

Returning to the case of droplet spreading, it is important to note that the total volume of liquid is constant. The spreading is constrained by the conservation of droplet volume. On a smooth surface, if capillarity dominates the motion, the droplet spreads with a power law of time $t^{1/10}$, as explained previously. Surface roughness significantly influences this spreading, with exponent ranging between 0.25 and 0.5 [43, 67]. Introducing grooves onto the surface further modifies the spreading dynamics by confining the droplet within the groove. For droplets in V-shaped micro-grooves [68] and rectangular micro-grooves [69] the spreading follows a power law with an exponent of $1/2$. Warren also calculated several spreading power laws, in V-shaped grooves, the theoretical calculations predict an exponent of $2/5$ [70]. Droplets spreading across a forest of micropillars [55, 71], follows diffusion dynamics like BCLW law.

All the scaling provided here above are for intermediate stages of spreading when the inertial effects are neglected. Table 1.1 summarizes all the scaling laws found in literature.

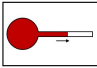
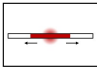
Volume	Structure	Scaling	
Not conserved	Cylindrical tube [48, 49, 50], Porous substrate [54, 55, 53, 56], Rectangular groove [52, 51], Curved groove [52]	$t^{1/2}$	
		Curved corners [62, 63], V-shaped groove [64], Porous substrate [66]	$t^{1/3}$
	Diverging conical [60], Converging conical [61]	t^n	
Conserved	Rough substrate [43, 67], V-shaped groove [68], Rectangular groove [69], Micropillars substrate [55, 71]	$t^{1/2}$	
		V-shaped groove [70]	$t^{2/5}$
	Flat substrates [44, 45], Flat substrates [46], Flat substrates [38]	$t^{1/10}$ $t^{1/8}$ $t^{1/7}$	

Table 1.1: Table comparing studies about the scaling found for the spreading rate dynamics. Literature can be divided into two categories, studies with a reservoir that fills the structure (where the volume is not conserved) and studies with a droplet spreading on the structure (where the volume is constant). The exponent n depends on the axial variation of the groove.

1.4 Droplets on cylindrical fiber

Let's come back to the storyline of raindrops falling from the sky that encounter a substrate. In the previous section, we described the behavior of a droplet on a flat substrate. However, a droplet may fall onto a curved surface such as branches of trees, stems of plants, or fibers of spider webs. In the following, we describe the behavior of droplets on cylindrical fibers, focusing on their shapes and spreading dynamics.

1.4.1 Droplet geometries and wetting

A droplet on a cylindrical fiber can adopt three different shapes depending on the fluid properties and the fiber characteristics. The droplet may spread completely along the fiber forming a thin film on the surface. Alternatively, the droplet could envelop the fiber with a barrel-like shape, such as droplets observed on spider webs. Lastly, the droplet may have a clamshell shape, resting on one side of the fiber, such as droplets on plant stems.

In the preceding section, we introduced the spreading parameter S , which evaluates the energy balance between a dry and a wet surface. For a droplet to spread completely on a flat substrate, S must be positive, as expanding the liquid-air interface corresponds to a reduction of the liquid-solid interface. However, when considering a cylindrical fiber, the spreading condition is different due to the larger surface area of the liquid-air compared to the solid-liquid interface [24]. For a droplet to achieve a complete spreading on a cylindrical fiber, the spreading parameter S must exceed a critical threshold S_c . This critical value is given by

$$S_c = \frac{3}{2}\gamma \left(\frac{a}{r_f}\right)^{2/3}, \quad (1.33)$$

with a the size of the molecules of the fluid and r_f the fiber radius [24]. This implies that wetting fluids ($\theta \approx 0^\circ$) can form a droplet on fibers while a liquid film on flat substrates.

When the spreading parameter is smaller than S_c , a droplet on a cylindrical fiber may adopt two distinct shapes, the barrel shape or the clamshell shape. The barrel shape surrounds the fiber entirely maintaining an axisymmetrical shape around the fiber [72]. The clamshell shape is characterized by a droplet covering only a portion of the fiber cross-section, not encircling it completely [73, 74]. Both shapes are illustrated in the Figure 1.9 (a). For a given fiber material and a given fluid, the barrel shape is generally adopted when the fiber radius is small or the volume of the droplet is large. On the other hand, the clamshell configuration appears for thicker fibers and smaller volumes of droplets. To predict the droplet's configuration on the fiber, one can employ the reduced volume V^* defined as

$$V^* = \frac{\Omega}{r_f^3}, \quad (1.34)$$

where Ω is the volume of the droplet and r_f the radius of the fiber [74]. A large reduced volume typically results in a barrel shape, whereas a smaller reduced volume

produces a clamshell shape droplet, see the diagram in Fig. 1.9 (b) [75].

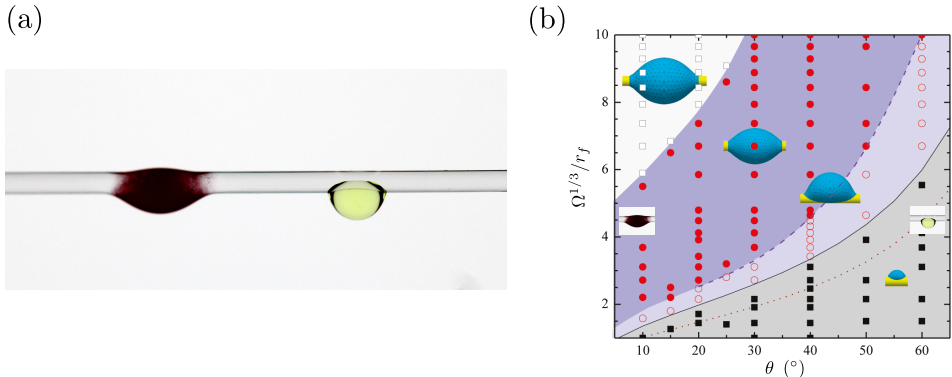


Figure 1.9: (a) Picture of a silicone oil droplet with a barrel shape (left) and a glycerol droplet with a clamshell shape (right) (credit: J. Van Hulle). Both droplets have the same volume, $\Omega = 1 \mu\text{l}$ and are on the same nylon fiber with a diameter of $d = 450 \mu\text{m}$. (b) Diagram of the reduced diameter $\Omega^{1/3}/r_f$, with Ω the droplet volume and r_f the fiber radius, as a function of the contact angle θ , that shows geometry adopted by the droplet (without gravity). Barrel shapes (■) and clamshell shapes (□) are depicted on the diagram and the region of coexistence of both shapes is represented with (●) and (○), respectively. From [75]. The pictures in (a) are added to this graph at the corresponding estimated positions.

In addition to the fiber radius and the droplet volume, the contact angle θ of the liquid on the fiber plays a crucial role in determining the droplet's shape [75, 76]. Fluids that exhibit less wetting characteristics ($\theta \gg$) are inclined to form clamshell shapes, while wetting fluids frequently adopt barrel shapes, as shown in Fig. 1.9 (b). Notably, in the case of such wetting fluids forming barrel shapes, an inflection point can be noticed on the surface of the droplet [77]. Altering any key parameter (droplet volume, fiber radius or contact angle), can trigger a transition from the clamshell shape to the barrel shape. For example, increasing the volume of a water droplet initially in a clamshell shape can cause it to transform into a barrel shape. This transition is called the roll-up transition [78].

The mathematical expression of the barrel shape profile can be derived theoretically by assuming a totally wetting liquid droplet with a constant pressure inside the droplet, a constant curvature of the surface and negligible gravity effects [72]. Under such circumstances, the Laplace overpressure inside a barrel-shaped droplet is given by

$$\Delta P = \frac{2\gamma}{r_f + r}. \quad (1.35)$$

This pressure depends on both the radius of the fiber r_f and the radius of the droplet r . In the case of the clamshell shape, as the geometry is asymmetric, no analytical solution for the mathematical profile expression is reported for cylindrical fibers. Only numerical solutions using Surface Evolver are available [73, 74, 79].

Finally, the droplet shape is influenced by gravity when the droplet size is larger than the capillary length l_c . In such case, the symmetric barrel shape is deformed and adopts an asymmetric barrel shape, as shown in Fig. 1.10 [75, 76, 80].



Figure 1.10: Pictures of silicone oil droplets on a horizontal fiber whose radius is $r = 12 \mu\text{m}$. From left to right the volume of the droplet increases $\Omega = 0.01, 0.10, 0.23, 0.32$ and $0.52 \mu\text{l}$. From [80].

1.4.2 Fluid coating : Landau-Levich-Derjaguin theory

With a wetting fluid, it is possible to uniformly coat a cylindrical fiber with a thin liquid film. The most conventional method for achieving such a coating is to withdraw the fiber vertically from a liquid bath at a constant speed, as illustrated in Fig. 1.11. The final thickness of the deposited film is influenced by several factors: the radius of the fiber, the viscosity and surface tension of the fluid, and the speed at which the fiber is pulled. This phenomenon was analyzed theoretically by Landau, Levich, and Derjaguin for a solid plate, giving rise to what is known as the LLD theory. The principles of the LLD theory have since been adapted and applied to a variety of substrate geometries, as discussed in further detail by Quéré [81].

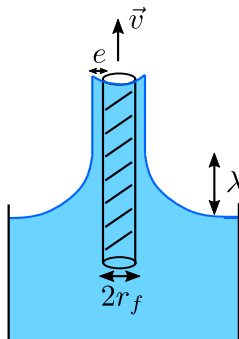


Figure 1.11: Illustration of a fiber pulled out of a liquid bath with a velocity v . The radius of the fiber is r and the resulting coating film thickness is e . The region where the meniscus is deformed is the dynamic meniscus and it has a characteristic length λ .

As the fiber is pulled out from the liquid bath at a speed v , a film with thickness e forms around the fiber. Close to the liquid bath, the liquid forms a dynamic meniscus characterized by a length λ (see Fig. 1.11). This characteristic length is determined by balancing the Laplace pressure, defined in Eq. (1.6) of the static and dynamic menisci. In a static meniscus, the Laplace pressure is zero if the fiber radius is smaller than the capillary length. In the moving meniscus, the pressure

contains two terms representing the curvature of the fiber and the curvature of the fluid profile [81]. Matching both pressures leads to

$$\frac{\gamma}{r_f + e} - \frac{\gamma e}{\lambda^2} \sim 0. \quad (1.36)$$

In the approximation of thin films ($e \ll r_f$), this equation simplifies to provide the characteristic length of the dynamic meniscus as

$$\lambda \sim \sqrt{er_f}. \quad (1.37)$$

In meniscus dynamics, the flow generated by the curvature of the film and the subsequent Laplace pressure can be approximated as $\Delta P \sim \gamma/r_f$ (with $e \ll r_f$). This flow is counteracted by viscous forces, leading to a dimensional balance expressed as

$$\frac{\eta v}{e^2} \sim \frac{1}{\lambda} \frac{\gamma}{r_f}. \quad (1.38)$$

Incorporating Eq. (1.37), one obtains the expression of the liquid film thickness,

$$e \approx r_f \left(\frac{\eta v}{\gamma} \right)^{2/3}. \quad (1.39)$$

The precise formulation of the LLD (Landau-Levich-Derjaguin) law for a fiber withdrawn from a liquid bath is

$$e = c_{dry} d \text{Ca}^{2/3} \quad (1.40)$$

where Ca is the capillary number, $c_{dry} = 0.67$ is a theoretical prefactor and d is the fiber diameter. This relationship provides an approximation for the film thickness based on the fiber radius, the fluid's viscosity, the withdrawal speed, and the surface tension.

1.4.3 Rayleigh-Plateau instability

When such a liquid film coats a cylindrical fiber, it's common to observe the film undergoing spontaneous destabilization, leading to surface minimization. This process is depicted in Fig. 1.12 and is attributed to the Rayleigh-Plateau instability, a phenomenon closely aligned with the instability discussed in section 1.1.3. In both instances, surface tension acts as the driving force behind the observed behavior. Considering a liquid film of initial thickness e_0 surrounding a fiber of radius r_f , the destabilization is marked by a characteristic wavelength λ and an average film thickness e^* [19]. The variation in the film thickness along the x axis can be modeled as $e = e^* + \delta e \cos(qx)$, where q represents the wave vector related to the wavelength $\lambda = 2\pi/q$. By expressing the volume conservation of the fluid over a single wavelength, the following relationship is established

$$\lambda\pi (r_f + e_0)^2 = \lambda\pi \left((r_f + e^*)^2 + \frac{\delta e^2}{2} \right). \quad (1.41)$$

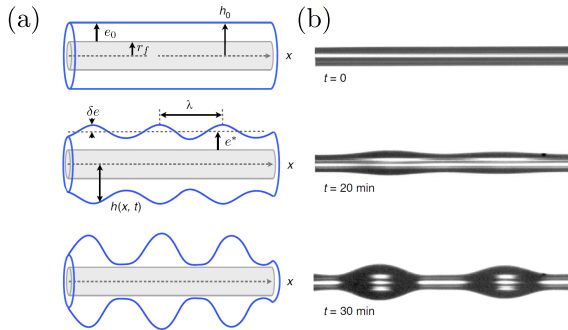


Figure 1.12: (a) Illustration and (b) pictures of the Rayleigh-Plateau instability occurring when a thin liquid film coats a cylindrical fiber. These figures are taken from [82]. The fiber is made of glass and the liquid is polystyrene. The radius of the fiber is $9.6 \pm 1 \mu\text{m}$ and the initial liquid film thickness is $e_0 = 13.2 \pm 1 \mu\text{m}$.

With the assumption of minor variations of the interface, one obtains the expression of the mean thickness

$$e^* = e_0 - \frac{\delta e^2}{4(r_f + e_0)}. \quad (1.42)$$

The mean thickness, during the destabilization, is smaller than the initial thickness, one can therefore have the intuition that the modulation of the film reduces the surface and, consequently, the energy of the system. To quantify the change in energy, ΔE , we focus only on surface energy, neglecting gravitational effects which are insignificant for thin films. The energy difference over one wavelength is

$$\Delta E = \int_0^\lambda 2\pi(r_f + e)\gamma ds - 2\pi(r_f + e_0)\gamma\lambda, \quad (1.43)$$

with s the curvilinear abscissa. The first term is the surface energy of the modulated film, and the second term corresponds to the surface energy of the initial non-destabilized cylindrical film. By considering small deviations of the surface, i.e. $ds \approx dx(1 + 1/2(de/dx)^2)$, we integrate the first term to find the difference in energy between the modulated and the cylindrical films,

$$\Delta E = \frac{\pi}{2}\lambda\gamma\frac{\delta e^2}{(r_f + e_0)}(q^2(r_f + e_0)^2 - 1). \quad (1.44)$$

A negative ΔE implies that the destabilized film is energetically favored, it is the case when the wave vector q satisfies the inequality $q(r_f + e_0) < 1$. This inequality yields

$$\lambda > 2\pi(r_f + e_0), \quad (1.45)$$

meaning that destabilization is inevitable for wavelengths exceeding the perimeter of the initial cylinder. Among the possible wavelengths satisfying this criterion, the one selected is the most amplified one. Its value is determined with a linear stability analysis under the lubrication approximation of thin films ($e_0 \ll r_f$). This analysis, detailed in Appendix B, leads to the wavelength of Rayleigh-Plateau

$$\lambda_{RP} = 2\pi\sqrt{2}r_f, \quad (1.46)$$

which is the most unstable wavelength that dictates the regular pattern of bead formation along the fiber. Furthermore, the growth time is given by

$$\tau_{RP} = 12 \frac{\eta r_f^4}{\gamma e_0^3}. \quad (1.47)$$

Quéré's observations on vertical fibers reveal that under certain conditions, the cylindrical film remains stable [83]. Indeed, with a vertical fiber, the liquid drains downwards, creating a velocity profile across the film thickness, that may inhibit the instability. In such scenarios, no droplet forms because the characteristic time of the gravitational flow τ is shorter than the characteristic time of the instability τ_{RP} . The characteristic time τ is given by a characteristic speed that compares gravitational to viscous effects, $v \sim \rho g e^2 / \eta$ that moves the fluid along a distance having the order of the instability wavelength $\lambda_{RP} \sim r_f$. The characteristic time of the instability τ_{RP} is given by Eq. (1.47). Applying the condition $\tau < \tau_{RP}$, one finds

$$e_0 < c_c \frac{d^3}{l_c^2} \quad (1.48)$$

with $c_c = 0.175$ a coefficient and d the fiber diameter. In other words, the threshold film thickness below which the Rayleigh-Plateau instability is suppressed in vertical fiber is $e_c = c_c d^3 / l_c^2$. However, when the film thickness is larger than this critical value, various behaviors are observed, as explained here below.

1.4.4 Liquid film flowing down a fiber

In experiments focusing on uniform liquid films descending along a vertical fiber, the fluid is introduced at a constant flow rate Q . The interplay between the flow rate, fiber radius and nozzle diameter determines the emergence of several regimes [84, 85, 86, 87, 88]. These regimes are destabilization of the film caused by the Rayleigh-Plateau instability, driven by surface tension, and can be categorized into three distinct regimes: (a) The isolated droplet regime or dripping state where primary droplets spaced evenly move at a constant speed and coalesce with smaller secondary beads (secondary breakup of the thin film) in a cyclic pattern [89]; (b) The steady Rayleigh-Plateau regime where a regular sequence of short-spaced and periodic droplets is observed descending the fiber at constant speed and spacing without any collisions; (c) The unsteady and convective regime is characterized by random coalescence events where primary droplets merge to form larger droplets, which then coalesce with subsequent primary beads, the overall bead pattern is irregular. These three regimes are shown in Fig. 1.13. In the isolated droplet and Rayleigh-Plateau regimes, beads move at a constant speed and spacing, demonstrating absolute instability. Conversely, the convective regime is marked by coalescence events occurring at irregular distances from the nozzle, indicative of convective instability [90]. Adjusting the incoming flow rate, while maintaining the same fiber radius and nozzle diameter, transitions between these regimes. By increasing the flow rate, the regime transitions from the isolated to Rayleigh-Plateau and then to convective. Similarly, increasing the fiber diameter with a fixed flow rate triggers the same sequence of regime changes. Modifying the nozzle diameter,

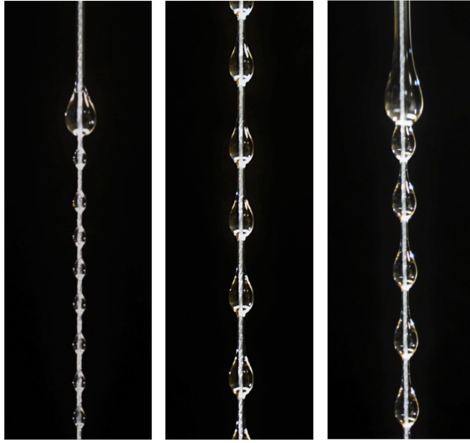


Figure 1.13: Experimental pictures of a liquid film flowing down a vertical fiber. Three regimes can be observed, (left) isolated regime, (middle) Rayleigh-Plateau regime and (right) convective regime. From [88].

the fluid's properties, or the fiber cross-section, can also influence these transitions [87, 91, 92, 93, 94]. High surface tension fluids ($\gamma > 50$ mN/m) or large fiber radii can lead to asymmetrical droplets in these regimes [92], as shown in Fig. 1.14. Asymmetrical droplets may also form from liquid films influenced by lateral winds [95]. In scenarios where inertia dominates surface tension effects (large flow rates), the Rayleigh-Plateau instability is supplanted by the Kapitza instability leading to the formation of capillary wave trains along the liquid film [96]. These various regimes and transitions underscore the rich complexity of fluid behavior on vertical fibers.

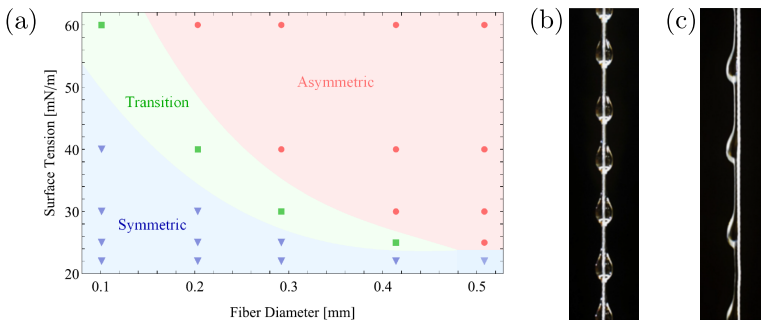


Figure 1.14: (a) Diagram describing the shape adopted by a liquid flow on a vertical fiber in the Rayleigh-Plateau regime. It depends on the surface tension of the liquid used and the fiber diameter. The droplet geometry is either symmetrical or asymmetrical. (b) Experimental pictures of the symmetrical configuration and (c) the asymmetrical morphology. From [92].

1.4.5 Motion of droplet on a fiber

In this section, we analyze the motion of a barrel-shaped droplet descending along a vertical dry fiber. A droplet on a fiber, as on an inclined surface, exhibits two different contact angles at the front and the rear of the droplet [97]. The motion of the droplet is triggered when these angles overcome a critical value. This descending motion on a vertical fiber is the focus of the work of Gilet *et al.*, where they establish a balance between the droplet's weight and its viscous dissipation [98].

To describe the viscous dissipation occurring in a droplet on a vertical fiber, we can refer to the study of Lorenceau and Quéré [99]. They analyze the dissipation in both the liquid wedge, defined near the advancing contact line, and the bulk of the global macroscopic droplet wedge for droplets on cylindrical fibers. The dissipation in the viscous and dynamic liquid wedge is given by Tanner's law, with the contact angle described as $\theta \sim (\Gamma\eta v/\gamma)^{1/3}$ (see Eq. (1.26)). This leads, according to Eq. (1.25), to the following expression for the dissipation force

$$F_{wedge} \sim \gamma r_f \left(\frac{\eta v \Gamma}{\gamma} \right)^{2/3}. \quad (1.49)$$

In the case where the dissipation occurs in the global droplet, the contact angle is related to the width l and length L of the droplet, with the wedge described as $\theta \sim l/L$. Under these conditions and according to Eq. (1.25), the dissipation force can be expressed as

$$F_{global} \sim \eta r_f \Gamma v \left(\frac{L}{l} \right). \quad (1.50)$$

In the case study of Gilet, the viscous dissipation occurs mainly in the bulk of the droplet and is quantified as

$$F_\eta = \xi \eta d v \quad (1.51)$$

where ξ is a coefficient taking both geometric aspects and the ratio of the droplet's length to its width (indicative of the dynamical contact angle), where d is the fiber diameter and v is the droplet speed. Gilet *et al.* express ξ as $\xi = \pi C_v \Gamma \frac{L}{l}$ with L and l denoting respectively the length and width of the droplet [98], and C_v being a numerical drag coefficient of the order unity for cylinders. Applying Newton's third law, while disregarding inertia, yields

$$0 = \rho g \Omega - F_\eta, \quad (1.52)$$

which leads to the expression of the speed, when taking $\dot{z} = v$,

$$\dot{z} = \frac{1}{\xi} \frac{\rho g \Omega}{\eta d}. \quad (1.53)$$

As the droplet descends along the dry fiber, it leaves a liquid film behind (LLD theory), diminishing its volume. The volume loss rate is captured by

$$\dot{\Omega} = -\pi d e \dot{z}, \quad (1.54)$$

where the left film thickness e is specified according to the LLD theory (see Eq. (1.40)). By solving the differential equation formed by Eqs. (1.53) and (1.54), the evolution of the droplet position z as function of time t is obtained,

$$z = \frac{\dot{z}_0^{1/3} - \left(\dot{z}_0^{-2/3} + \frac{2}{3}wt\right)^{-1/2}}{w/3}, \quad (1.55)$$

where \dot{z}_0 is the initial speed of the droplet and where w is a parameter that depends on physical constants

$$w = \frac{c_{dry}}{C_v \Gamma} \frac{l}{L} \left(\frac{\eta}{\gamma}\right)^{2/3} \frac{\rho g d}{\eta}. \quad (1.56)$$

This theoretical model alongside experimental data is illustrated in Fig. 1.15 (a). The model depicts well the observed droplet motion.

A metastable shape, both observed in [98] and [100], of a clamshell shape droplet descending on a vertical fiber even though its reduced volume exceeds unity, as shown in Fig. 1.15 (b). Nevertheless, this clamshell configuration is unstable and transitions to the barrel shape, at which point the descent speed decreases by a factor 3 [98].

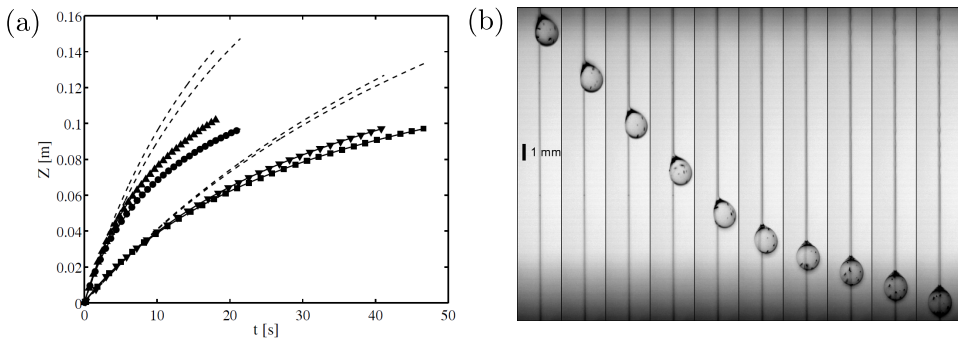


Figure 1.15: (a) Graph of the position z along time t of a barrel shape droplet descending along a vertical fiber. Experimental parameters : $d = 0.25$ mm, (●) $\nu = 10$ cSt, (▲) $\nu = 20$ cSt, (■) $\nu = 50$ cSt and (▼) $\nu = 100$ cSt. The dashed line corresponds to Eq. (1.55) with $c_{dry} = 0.67$ (the predicted value from the LLD theory) and the solid line is with $c_{dry} = 1.5$. (b) Experimental picture of an initially clamshell shape droplet ($\nu = 100$ cSt), descending a vertical fiber ($d = 160$ μ m), that shifts to the barrel shape (the stable configuration). The change in shape induces a sudden decrease in the vertical speed. Both images are taken from [98].

1.4.6 Several fibers

Arranging several fibers in different manners offers fascinating possibilities for droplet manipulations. By employing a combination of vertical and horizontal fibers, one can either suspend a droplet or allow it to pass through, leaving behind a small portion of its volume at the intersection, it is illustrated in Fig. 1.16 (a). This stop-and-go behavior is influenced by both the fiber radius and the droplet

volume [101]. Such interactions have led to the development of fiber-based systems capable of creating compound droplets, highlighting advancements in fluid manipulation techniques [102]. Moreover, by positioning two perpendicular fibers at an incline, it becomes possible to direct a droplet from one fiber to another by selecting the slope and the fiber diameter [103].

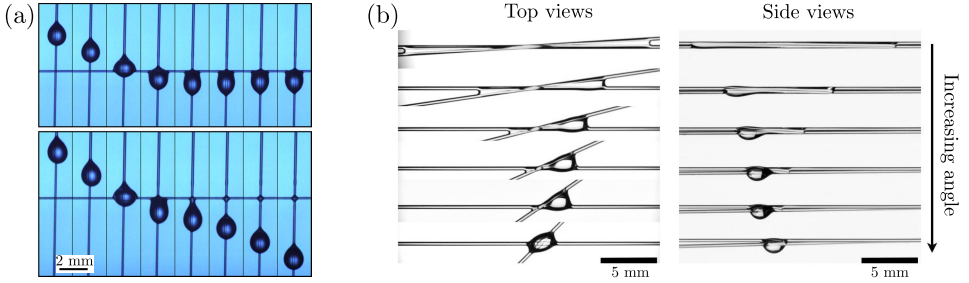


Figure 1.16: (a) Network of fibers created by a vertical fiber and a horizontal fiber, both fibers are in contact. A barrel shape silicone oil droplet descends along the vertical fiber. At the crossing, the droplet is either pinned and hung at the junction or the droplet crosses the horizontal fiber and leaves a thin liquid droplet at the junction. From [101]. (b) Silicone oil droplet at the node formed by two crossing fibers. Depending on the angle between the fibers, the droplet adopts three different shapes: a column morphology, a mixed shape with a droplet formed on one side of the column, and a single drop at the node. From [104].

From a static point of view, the shape adopted by a droplet depends on the angle made by the two horizontal fibers. When starting from two parallel fibers and gradually increasing the angle between them, the droplet transitions from a columnar morphology with a droplet spread between the fibers, to a mixed shape with a droplet formation on one side of the column, to a single drop at the intersection as shown in Fig. 1.16 (b) [104]. With vertical fibers, the separating angle significantly affects water droplet retention, with the optimal volume retention occurring at an angle of 36° between fibers [105]. The spacing between parallel fibers also plays a critical role. Close proximity leads to an elongated liquid column, whereas greater distances result in a compact, hemispherical droplet shape [106]. These two droplet shapes are illustrated in Fig. 1.17 (a). In setups with elastic fibers spaced apart, the fibers are seen, as in Fig. 1.17 (b), to being deflected inwards due to the action of the liquid droplet [107]. This is the same phenomenon occurring in a brush of fibers withdrawn from a liquid bath where the fibers are clustered together (see Fig. 1.17 (c)), as paint brushed or human long hairs after a heavy rain [108, 109].

A recent study by Khattak *et al* [110] demonstrates how varying the spacing between two horizontal rigid fibers can drive droplet motion. The droplet moves towards narrower gaps [111], a principle ingeniously applied using a saw-tooth pattern and a moving straight fiber to enable movement over extended distances, as shown in Fig. 1.18 (a). Additionally, when a constant liquid flow is applied between two vertical and parallel fibers, two different behaviors emerge, such as self-sustaining sheets or liquid bridge droplets [93], see Fig. 1.18 (b). Adding to the complexity these bridge droplets can rotate around an axis formed by two he-

lical spaced fibers, as illustrated in Fig. 1.18 (c). These examples showcase the potential for droplet manipulation using innovative multifiber configurations. We will explain in section 1.6 of this State of the Art, the application of fiber-based structures to harvest water in foggy environments.

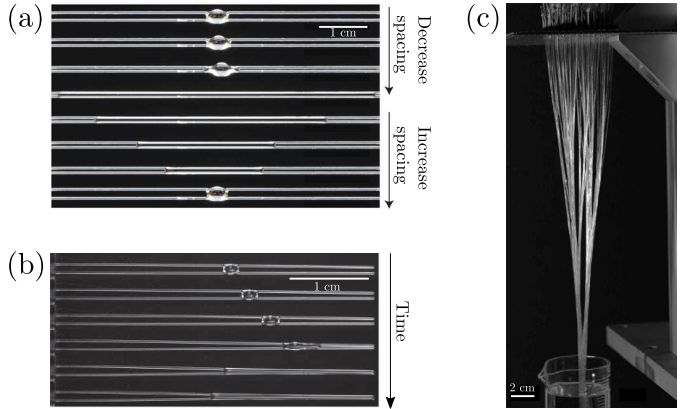


Figure 1.17: The spacing between two parallel fibers dictated the adopted shape. (a) The fibers are rigid and horizontal. For relatively large spacing, the droplet has the usual compact hemispherical shape while for less spaced fibers, the shape is a long liquid column. From [106]. (b) The fibers are elastic and vertical. Both fibers are fixed at one end (left part) and free at the other (right side). A droplet is deposited on the fibers and spontaneously moves towards the free end of the fibers, making the fibers to coalesce and the droplet to spread. From [107]. (c) Brush of several fibers withdrawn from a liquid bath. The same elongated droplet geometry is observed as in (b). From [109].

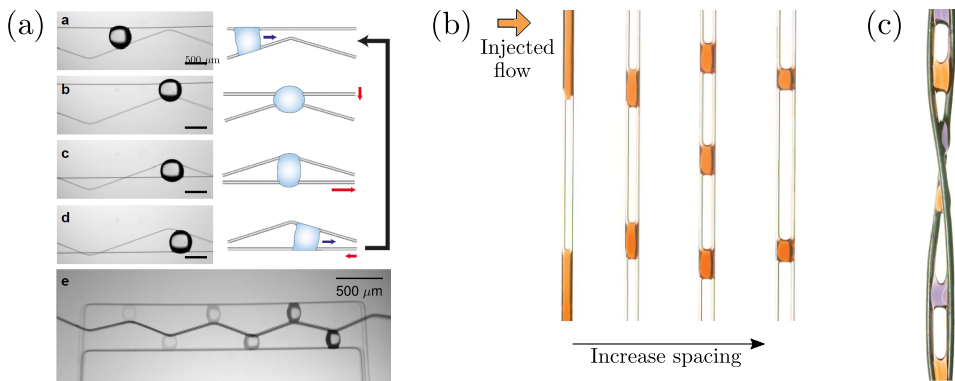


Figure 1.18: (a) Droplet motion induced by a reduced gap between two fibers. The droplet migrates towards narrow gap. By using a saw-tooth fiber and a straight fiber that cyclically translates above and under the saw-tooth fiber, the droplet can travel long distances. From [110]. (b) Constant liquid flow rate applied between two vertical fibers. Increasing the spacing induces the liquid sheet pattern to transition into a bridge droplet shape. From [93]. (c) Same experiment as in (b) with two helical spaced fibers. The bridge droplets rotated around their central axis. From [93].

1.5 Droplets on conical fiber

Lastly, the substrate on which the droplet sits can be a conical fiber. Such fibers are encountered in nature with cactus spines, pine needles, moss barbs, or plant hairs. This geometry introduces a gradient in the fiber radius. In this section, we provide an overview of the spontaneous motion of droplets that may occur on conical fibers.

1.5.1 Surface tension imbalance

A droplet on a conical fiber may exhibit a barrel or a clamshell shape, influenced by several physical parameters such as radius, volume and contact angle, as reviewed previously in section 1.4.1. In both geometries, the droplet encounters different radii on either side. This may lead to the motion of the droplet towards lower radii of curvature to minimize its liquid/vapor interface [112, 113]. This mechanism is entirely passive, as the droplet moves spontaneously without any external energy input into the system.

A pioneering study on the motion of droplets on conical fibers was conducted by Lorenceau and Qu  r   [99]. They studied the behavior of thin silicone oil barrel-shaped droplets that spontaneously move along horizontal conical copper fibers, towards the larger radius of the fiber, see Fig. 1.19. The droplet velocity is observed to decrease as it moves towards larger radii. This motion is due to the difference in the Laplace pressure inside the droplet, which is given by

$$\left. \frac{dP}{dz} \right|_{\Omega} = - \frac{2\gamma}{(r_f + h)^2} \left(\frac{dr_f}{dz} + \frac{dh}{dz} \right) \Big|_{\Omega}, \quad (1.57)$$

according to Eq. (1.35), where z is the distance from the tip of the fiber along the axis of the cone, h the height of the droplet taken from the fiber center and r_f is the local fiber radius.

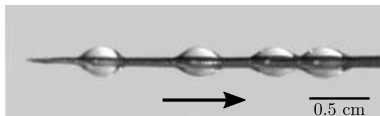


Figure 1.19: Superposition of pictures of a silicone oil droplet moving on a conical copper fiber. The picture time interval is constant, 1.6 s. The droplet moves towards large radii and its speed decreases along the motion. From [99].

Depending on the size of the droplet, the height h varies. For large droplets, h is constant and given by $R_0 = (\frac{3\Omega}{4\pi})^{1/3}$, while for small droplets, the geometry is very flat and the height tends towards the radius of the fiber, see Fig. 1.20. Considering these geometrical considerations [99, 114], the pressure gradient reduces to,

$$\left. \frac{dP}{dz} \right|_{\Omega} = \begin{cases} - \frac{2\gamma}{(r_f + R_0)^2} \alpha & \text{if } r_f < R_0 \text{ (large droplet),} \\ - \frac{\gamma}{r_f^2} \alpha & \text{if } r_f > R_0 \text{ (small droplet),} \end{cases} \quad (1.58)$$

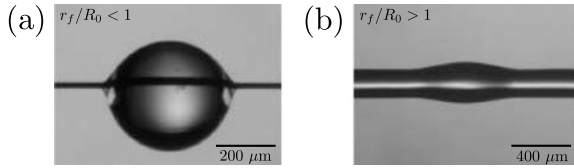


Figure 1.20: Silicone oil droplet having a radius R_0 on a fiber with a radius r_f . (a) Case of a large droplet, $r_f < R_0$, with $r = 12 \mu\text{m}$ and $R_0 = 200 \mu\text{m}$. (b) Case of a small droplet, $r_f > R_0$, with $r_f = 100 \mu\text{m}$ and $R_0 = 80 \mu\text{m}$. Both pictures are from [99].

with α the half-angle of the conical fiber and R_0 the radius of the droplet. The driving force is proportional to the pressure gradient,

$$F_{driving} \sim \frac{dP}{dz} \Omega. \quad (1.59)$$

Opposing the driving force is a dissipation force. In the experiments of [99], the droplets are small, and the dissipation is seen to occur mainly in the bulk of the droplet. The dissipation is thus given by Eq. (1.50). This leads to the description of the droplet velocity which is given by

$$v \sim \frac{\gamma}{\eta\Gamma} \left(\frac{h - r_f}{L} \right) \left(\frac{\Omega}{r_f^3} \right) \alpha. \quad (1.60)$$

With an increasing fiber radius, driving force decreases and the dissipation force increases. It explains why the droplet slows down as it moves towards thicker regions of a conical fiber [99, 115]. As the droplet moves, it leaves a liquid film at the rear [116, 117]. If the conical fiber is pre-wetted, the droplet moves faster due to reduced frictional force between the liquid and the solid [116, 118]. A larger lubricating film induces a faster droplet motion [118]. The prewetting liquid film may also destabilize due to Rayleigh-Plateau instability, forming droplets that spontaneously move along the cone [99, 119].

As the droplet moves, it increases the liquid/solid surface area. An equilibrium position is reached when the energy reduction from increased liquid/solid surface area balances the energy cost of extending the liquid/vapor interface. At this position of minimal energy, the droplet stops. This equilibrium position is observed theoretically and experimentally and depends on contact angle hysteresis, droplet volume, cone half-angle, and contact angle [120]. Droplets are expected to move further along the cone with larger volume or smaller half-angle and contact angle. Without contact angle hysteresis, the droplet undergoes shape instability, transitioning from a barrel to a clamshell shape [112, 118]. The clamshell shape droplets always move towards the base of the conical fiber, independent of wettability, as shown in Fig. 1.21 [121]. There is no equilibrium position for the clamshell-shaped droplets, meaning they continue moving towards lower curvature indefinitely. Under gravitational effects, both barrel and clamshell droplets reach an equilibrium position that minimizes the energy of the system [112]. To enhance droplet motion on conical fibers, concave or convex grooves can be added to the cone surface, enabling faster droplet movement [122, 123].

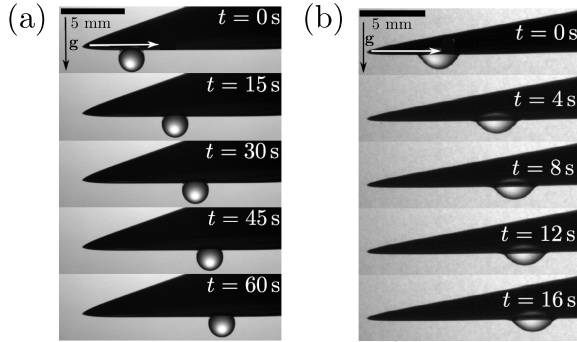


Figure 1.21: A water droplet with a clamshell shape ($\Omega = 4 \mu\text{L}$) on a slippery liquid-infused porous surface (SLIPS) conical fiber. (a) The coating liquid is silicone oil, which creates a non-wetting surface for water droplets with an apparent contact angle $\theta_{app} \approx 105^\circ$. The cone half-angle is 10° . (b) The coating liquid is decanol, creating a wetting surface for water droplets with an apparent contact angle $\theta_{app} \approx 45^\circ$. The cone half-angle is 5° . In both experiments (a) and (b), the water droplet spontaneously moves towards the base, irrespective of surface wettability. From [121].

1.6 Water collection

This final section of the State of the Art aims to describe a promising application of this thesis: enhancing atmospheric water collection. This involves capturing water present in steam flows, clouds, or humidity. Such harvesting is based on interactions between droplets and fibers to catch tiny droplets, to make them grow and to drain them towards a reservoir. The basic of water collection processes is explained here below.

1.6.1 Difference between fog and dew

An important distinction to establish is the difference between fog and dew. Water vapor can be cooled to create liquid water, this phase transition is induced by temperature variations while keeping constant volume and pressure. The temperature at which water vapor reaches its saturated vapor pressure is known as the dew point, at this temperature, excess vapor condensates. Both fog and dew result from water condensation but occur under different conditions. Fog forms when the air near the ground is cooled, creating clouds with suspended water droplets from, theoretically, homogeneous nucleation, and in practice, from heterogeneous nucleation on dust particles, pollen, pollution for instance [124]. Dew forms when a surface cools enough to cause surrounding water vapor in the air to condense upon it, this is a heterogeneous nucleation on the surface [12].

Fog and dew collection employ fundamentally different techniques [125]. For fog collection, water droplets have already nucleated, and a structure is required to capture the microscopic droplets. Such techniques mainly depend on aerodynamics and multiphase flows. In contrast, dew collection, also termed condensation collection, requires cooling a surface to facilitate the phase transition to liquid and

employ specific surface properties for nucleation. Despite these differences, both techniques necessitate the evacuation of collected water droplets. For dew collectors, the nucleation site must be freed of the collected water to allow the subsequent nucleation. For fog harvesters, water must also be evacuated because droplets on the structure decrease efficiency, as will be explained in the next section.

Moving the droplets, referred to as drainage, is a goal of this thesis, which aims to improve the displacement of liquid droplets. This is why water collection is an important perspective of our work. More specifically, this thesis focuses on fiber-based structures which are particularly suitable for fog collection. For dew collection, these structures are less suitable because of cooling challenges.

1.6.2 Bio-inspiration

In most arid regions like deserts, plants and animals have developed specific strategies in order to survive long periods without rain [126]. Among others, one can cite the *Stipagrostis sabulicola* Namib desert grass [127], the *Opuntia microdasys* cactus [5], the *Syntrichia caninervis* moss [6], the *Sequoia sempervirens* tree [128] or the *Sarracenia* insect trapping plant [4]. Other examples are spider web [3], *Phrynosoma cornutum* lizard [7] and the *Physasterna cribripes* Namib darkling beetle [8]. All the species have developed organs to harvest water: they have spikes, bumps, spines or hairs that are able to collect tiny drops of water from air, fog or rain.

From these various examples, we describe more particularly the *Opuntia microdasys* cactus, the *Sarracenia* insect trapping plant and the *Stipagrostis sabulicola* grass as these plants have interesting features further analyzed in the thesis.

The *Opuntia microdasys* cactus This cactus can collect fog droplets thanks to its spines [5]. The spines are clustered in small groups that appear white in Fig. 1.22 (a) and display a configuration with spines in various directions. Each hydrophilic spine has an average half-angle of 6° and at the tip, smaller conical bards can be observed, as shown in Fig. 1.22 (b) and (c) [114, 5]. The middle part of the spine features gradient grooves that are closer together near the tip and wider at the base, see Fig. 1.22 (c). At the base, there are trichomes, tiny hairs with a belt structure (Fig. 1.22 (d)). The fog collection process consists of three steps. First, collection: some fog droplets deposit on the small barbs and the spine tip, where they coalesce into larger droplets (see Fig. 1.22 (b)). Second, transportation: as the droplets grow large enough to sense the gradient radius, they move towards the base of the spine (see Fig. 1.22 (b)). This motion is driven by the gradient radius and the grooves. Finally, upon reaching the base, the droplets encounter the trichomes that rapidly absorb them. All these steps are sketched in Fig. 1.22 (d). The cycle then repeats as the spine, now free of the larger droplets, begins to collect new fog droplets. Note that droplets on inclined spines are also observed to move towards the plant [114, 5].

The *Sarracenia* insect-trapping plant This plant is an insect-trapping plant that lives in marshlands [4]. This plant consists of a pitcher, a long vertical tube with a peristome at the top, resembling a mouth, and an operculum, or lid, covered

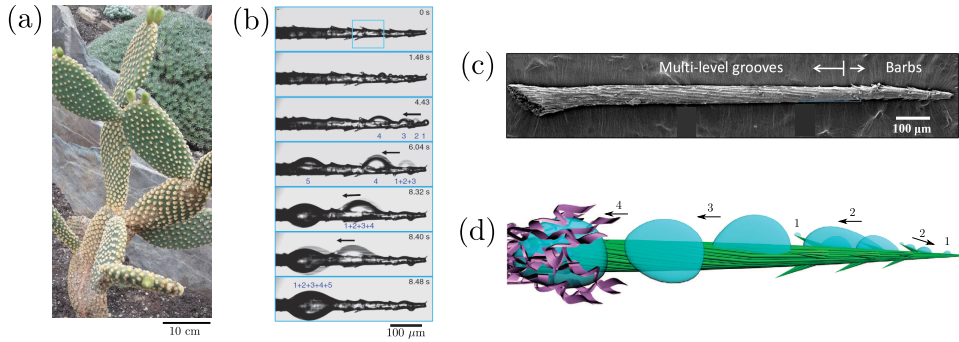


Figure 1.22: (a) Picture of the *Opuntia microdasys* cactus. The white dots are clusters of spines. (credit: J. Van Hulle). (b) A spine of the *Opuntia microdasys* cactus in a saturated fog flow. One observes the collection of the fog droplet thanks to the conical barbs at the tip of the spine, which coalesce to form larger droplets (0 s to 4.43 s). As the droplet grows, it moves towards the base of the conical fiber and thus the plant (6.04 s to 8.48 s). (c) A spine analyzed with a scanning electron microscope, showing the barbs at the tip of the spine and the grooves in the middle part. (d) Schematic illustration of the fog collection process, composed of three steps, the collection (droplets 1 and 2), the transportation (droplet 3) and the absorption (droplet 4). Images (b), (c) and (d) are from [5].

with tiny hairs, the trichomes, as shown in Fig. 1.23 (a). This plant collects water from the humid environment through its trichomes, which are grooved conical fibers. These hairs collect water in order to keep the peristome wet and highly slippery, thereby trapping insects [129]. The water collection is composed of two modes. Mode I, shown in Fig. 1.23 (b), involves the formation of a thin liquid film on the trichome surface. Small harvested water droplets coalesce and move towards the larger radius of the trichome. Once this film is formed, Mode II begins, characterized by the high-speed motion of continuous small droplets sliding on the thin liquid film. Mode II is illustrated in Fig. 1.23 (c). This motion reached about $11700 \mu\text{m/s}$, which is three orders of magnitude larger than the droplet motion observed on cactus spines. This rapid motion is attributed to the specific structure of the trichome. The trichome has an overall conical shape, as shown in Fig. 1.23 (d). The apex angle is about 17° at the tip, and the diameter increases slightly from $10 \mu\text{m}$ around the tip to $60 \mu\text{m}$ near the base. On its surface, ribs and microchannels are observed, as shown in Fig. 1.23 (e) to (h). The ribs vary in height, and their number increases closer to the base. Near the tip, there are typically 1 or 2 low ribs (Fig. 1.23 (f)), increasing to 4 or 5 near the base (Fig. 1.23 (h)). When the trichome harvests fog, the process starts by forming a thin liquid film inside the microchannels between the low ribs. After this film is formed, subsequent harvested droplets slide on this film and between two high ribs. The fast motion is driven by the capillary force exerted by the hierarchical microchannels.

The *Stipagrostis sabulicola* grass This grass is found in the Namib Desert of southwestern Africa, where regular fog events occur [127]. The plant, composed of long thin culms and leaves as shown in Fig. 1.24 (a), relies upon fog for water

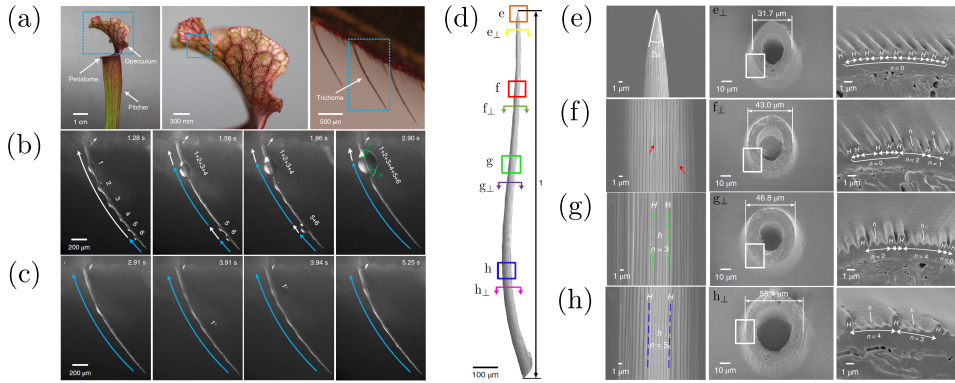


Figure 1.23: (a) Pictures of the *Sarracenia* insect-trapping plant. The trichomes, responsible for water collection from fog and dew, are small hairs on the operculum of the plant. (b) Mode I of fog water harvesting: small droplets form on the trichome, coalesce, and move towards the base, creating a thin liquid film along the natural fiber. (c) Mode II of collection: small droplets slide rapidly on the liquid film. (d) The structure of the trichome is a conical fiber with hierarchical grooves on its surface. (e) to (h) Scanning electron microscopy images of the trichome's surface to highlight the two-height ribs and the microchannels. From [4].

intake. Water droplets with large advancing and receding contact angles ($\theta_A \sim 98^\circ$ and $\theta_R \sim 56^\circ$, respectively) are observed to pin on the grass leaves, see Fig. 1.24 (b). Once the water droplet becomes large enough, it slides straight down towards the base of the plant, collecting all the smaller pinned droplets along the way. The directional motion, with minimal scattering of droplets, is attributed to the parallel ridges and grooves observed on the culms and leaves of the plant, as highlighted in Fig. 1.24 (c) and (d). The ridges have diameters of about $100 - 150 \mu\text{m}$ and the grooves have diameters of about $30 - 80 \mu\text{m}$.

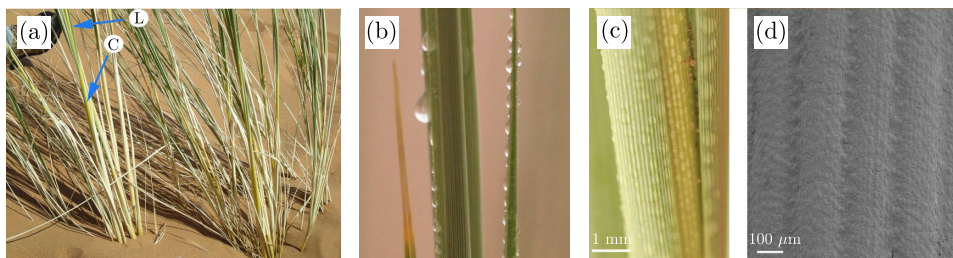


Figure 1.24: (a) Picture of the *Stipagrostis sabulicola* Namib grass. The arrow labeled "L" indicates the leaves, while the arrow labeled "C" points to the culms. (b) A Namib grass leaf with collected fog water droplets, showing the advancing and the receding contact angles. (c) Droplets on the leaves, highlighting the grooves and ridges on the leaf surface as well as droplets spanning multiple grooves. (d) Scanning electron microscopy image of the leaf surface. From [127].

A general observation from these three fog collecting plants is that they all have the same features, namely conical spines and a grooved surface.

1.6.3 Fog collectors

We review here below synthetic fiber-based (cylindrical and conical) fog collectors, directly inspired by spider webs and cactus spines. In this specific case, fog is formed due to atmospheric conditions and is transported by the wind towards the structure.

Fog collectors are usually made of a mesh composed of an intertwining of horizontal and vertical fibers, which effectively collect water droplets present in the fog. The experimental setup consists of placing a vertical mesh in an opened land so the wind, which carries fog droplets, blows perpendicular to the net, as illustrated in Fig. 1.25. In experimental lab setups, the mesh is placed in front of a wind fan that blows perpendicular to the mesh. Several parameters can be tuned to improve the collection: the fiber radius, the half-spacing between the fibers, and the fog droplet radius. The global collection efficiency is composed of three distinct contributions

$$E = E_{AC}E_dE_{dr},$$

where E_{AC} is the aerodynamic collection efficiency, E_d is the deposition efficiency, and E_{dr} is the drainage efficiency [130]. Each efficiency is explained below.



Figure 1.25: Picture of a fog collector made of meshes. The structure is vertical, allowing the wind to blow through it. The water droplets transported by the wind may collide with the mesh and drain towards a gutter below the net. From [131].

The aerodynamic collection efficiency E_{AC} : This represents the portion of the unperturbed flow that goes through the net, while the rest of the flow is deviated around the net. A representation of the aerodynamic effects is illustrated in Fig. 1.26 (a). Rivera showed that it depends on the shade coefficient s , which describes the proportion of holes and matter in the net. A plate with no holes corresponds to $s = 1$, will completely deviate the flow, resulting in no collisions between the flow and the plate. Conversely, a mesh with large holes and extremely thin fibers, so a small shade coefficient, will leave the flow unperturbed, and no water will be collected. The maximum aerodynamic collection efficiency is demonstrated to be around $s = 0.5$, meaning the net is composed of 50% of holes and 50% of matter [130].

The deposition efficiency E_d : This represents the fraction of fog droplets in a collision trajectory that are actually deposited on the meshes [130]. The condition of collision depends on the Stokes number,

$$\text{St} = \frac{\text{inertia}}{\text{viscous drag}} = \frac{2\rho r_{\text{fog}}^2 v}{9\eta r_f}, \quad (1.61)$$

where r_{fog} is the typical radius of a fog droplet, v is the flow speed, r_f is the radius of the fiber. If the Stokes number is larger than 1, inertia dominates, and the droplet collides with the fiber. A Stokes number smaller than one means viscous drag overcomes inertia, causing the droplet to deviate by following the wind streamlines around the fiber, resulting in no collision. A representation of the deposition and inertial effects is illustrated in Fig. 1.26 (b). Langmuir calculated the capture efficiency for a cylindrical fiber and showed that the thinner the fiber, the larger the capture efficiency [9, 132].

The drainage efficiency E_{dr} : This represents the proportion of water captured by the net that actually flows to the reservoir [130]. A representation of a draining net is illustrated in Fig. 1.26 (c). This efficiency can be reduced by several factors, including the re-entrainment of captured droplets, evaporative losses and potential leaks in the gutter and pipes leading to the collector's reservoir [9].

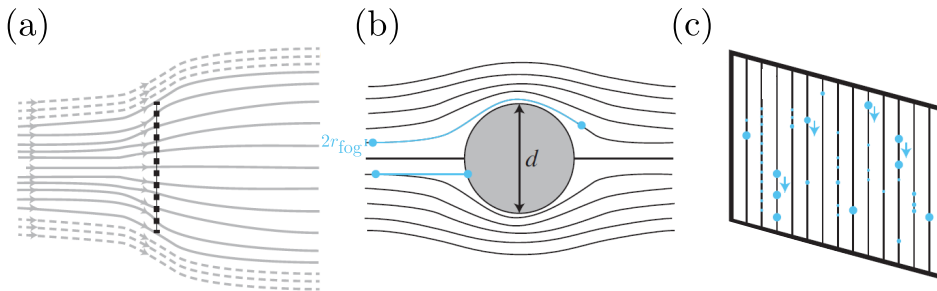


Figure 1.26: Representation of fog collection efficiency. (a) Aerodynamic effects seen from above the net. The fog flow is deviated due to the presence of the net. (b) One single portion of the net (a fiber) interacting with the inertial fog droplets. The droplets may either follow the streamlines around the fiber or impact it, depending on their inertia. (c) Droplets collected by the net (here made of vertical fibers) need to drain towards the gutter. From [133].

Fibers are interesting components to design the net as each efficiency can be optimized, in addition to being low-cost. The shade coefficient can be easily adjusted by adding or removing fibers, thus improving E_{AC} easily. The capture efficiency can be modified by changing the fiber diameter, and the drainage efficiency can be enhanced with hydrophilic wires that spread droplets into liquid films. Robust nets made of both horizontal and vertical fibers are capable of collecting fog but are limited by clogged droplets, which remain on the net without draining and

reduce the mesh openness, both factors impacting overall efficiency [9]. A solution is to use only vertical fibers, similar to harps, as shown in Fig. 1.27 [134, 135, 136]. This configuration increases efficiency by limiting clogging events. However, some droplets may still remain on the fibers without draining, impacting the collection rate [137]. To further improve this, placing two fibers side by side can help. A droplet on a bundle of two fibers tends to form a columnar shape as observed in section 1.4.6, enhancing both the drainage and the capture efficiency [137, 133]. Another interesting improvement is to use multi-layer fiber nets, adding another net behind the first one, which optimizes the aerodynamic collection efficiency [138].

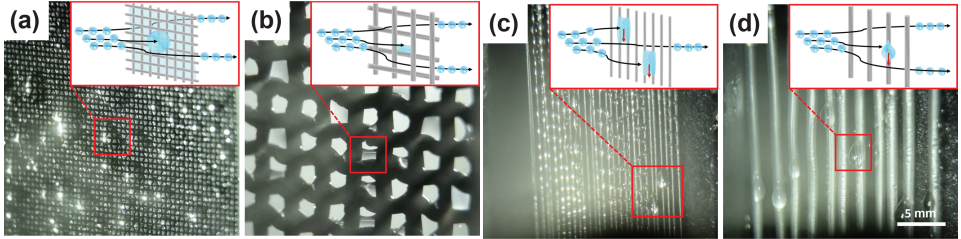


Figure 1.27: Experimental images of four stainless steel meshes ((a) and (b)) and harps ((c) and (d)). The nets (a) and (c) are made with thin fibers (diameters : (a) $d = 254 \mu\text{m}$, (c) $d = 229 \mu\text{m}$). The nets (b) and (d) are made with larger fibers (diameters : (b) $d = 1.30 \text{ mm}$ and (c) $d = 1.60 \text{ mm}$). (a) The mesh is fully clogged with droplets, interfering with the aerodynamics of the fog stream. (b) Only partially clogged droplets are observed, but the fibers are too large to efficiently capture fog droplets. (c) The most effective fog collector, as it efficiently captures droplets with small wires that also favor draining without clogging. (d) Large wire harp with efficient droplet drainage, but the capture rate is low due to the large fibers. From [134].

In fiber nets, the motion of droplets is mainly driven by gravitational force. This requires that droplets reach a critical size to initiate sliding motion. Gravity effects become significant when the droplet size exceeds the capillary length, which delays the onset of a new collection cycle at that position, increases the risk of evaporation, and decreases the deposition efficiency. Ensuring the motion of small droplets is crucial for continuous and efficient fog collection. Two approaches can be employed: creating wettability gradients along the fiber through chemical surface modification, and/or using surface gradients with conical structures [139]. In our context, we will discuss the latter solution.

Conical fibers in a fog flow are effective in catching fog droplets, similar to cylindrical fibers, as illustrated in Fig. 1.28 (a) [16]. These fibers initially capture small droplets that coalesce into larger ones, which then move towards the base of the cone. Conical fibers facilitate the spontaneous movement of droplets from the tip to the base without relying on gravity, thereby continuously refreshing the collecting surface and enhancing the global fog collection efficiency. Two notable designs incorporating conical fibers are the kirigami cactus and cone-pierced membranes. The kirigami cactus design corresponds to sheets cut into triangular shapes, inspired by a combination of harps and cactus spines. The 2D spines collect fog water droplets and self-propel them towards a central axis between the two rows of

spines, as shown in Fig. 1.28 (b). The central axis gathers the collected droplets, which grow rapidly due to the input from several spines, forming a large droplet that slides vertically along the axis towards a gutter [140]. The second design, cone-pierced membranes, features a network of conical fibers that pierce a porous membrane. The conical fibers capture and transport fog droplets to the porous membrane, that absorbs and releases the collected water on the other side. These conical fibers are inspired by the *Sarracenia* insect-trapping plant with hierarchical microgrooves on their surfaces. Additionally, the porous membrane is optimized with a Janus system consisting of a hydrophobic layer near the cone base and a hydrophilic layer underneath. The membrane is also designed with bumps to favor liquid dripping, enhancing the overall efficiency of the fog harvester, as illustrated in Fig. 1.28 (c) [141].

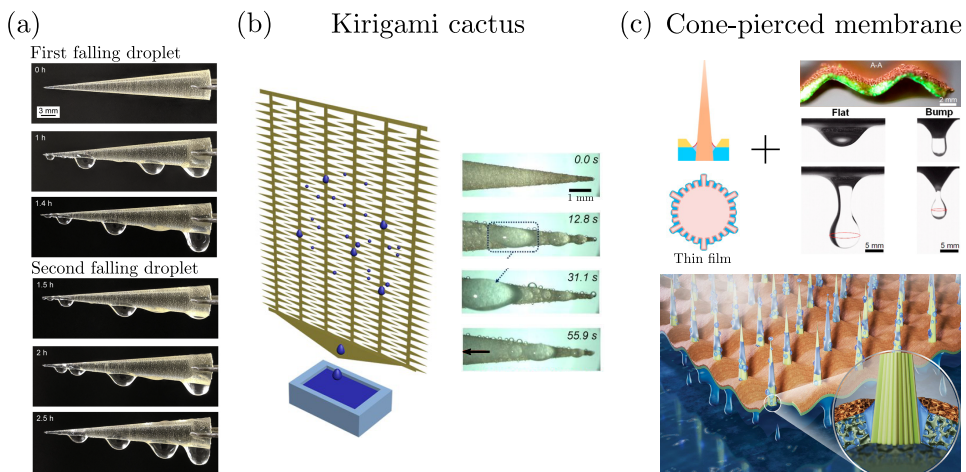


Figure 1.28: (a) Horizontal conical fiber with a 10° half-angle in a perpendicular to the cone large axis fog flow. The fiber captures fog droplets that coalesce on the cone surface to form larger droplets that move towards larger radii. The collected water droplet detaches from the end of the fiber. From [16]. (b) Kirigami cactus which is a cut sheet with triangular shapes, with a vertical central axis between the opposite triangles. Fog droplets are collected on the tips and edges of the triangles, where they merge and are transported towards the base. Once the larger droplets form on the central axis, they slide vertically towards a gutter. From [140]. (c) Cone-pierced membrane composed of hierarchical grooves conical fibers and a Janus membrane. The conical fibers pierce the porous membrane at regular intervals. The membrane consists of a hydrophobic layer near the cone base and a hydrophilic layer on the opposite side. As the conical fibers collect fog droplets, the liquid is transported into the porous media where it is absorbed and released on the other side. The membrane is embossed to favor droplet dripping compared to a flat membrane. From [141].

1.7 Foundations and Launch Pad

This thesis aims to expand our understanding of liquid spreading dynamics on macroscopic structures such as fibers and cones, and on macroscopic structures decorated with grooved substructures, including grooved substrates and grooved fibers. The important background necessary to appreciate the thesis subjects has been explained in this State of the Art section. In the following, we will dive into the thesis' core. Firstly, we will begin by describing the spreading dynamics of a droplet in a concave and a convex groove inscribed on a flat substrate. Next, we will examine different droplet descending motions on vertical fibers. A wetting droplet on a single cylindrical fiber leaves a liquid film that destabilizes to form new droplets. We will observe an interesting behavior of droplet merging. A droplet on a double-twisted cylindrical fiber exhibits helical motion that depends on the number of fiber twists. Finally, we will analyze droplet motion on conical fibers, focusing on shape deformation due to gravity and transition due to the increasing radius.

Throughout the thesis, we will progress from flat substrates to cylindrical fibers and then to conical fibers. The complexity of the substrates is further increased by incorporating grooved substructures. As will be explained, all these droplet-surface interactions are relevant to fog harvesting systems.

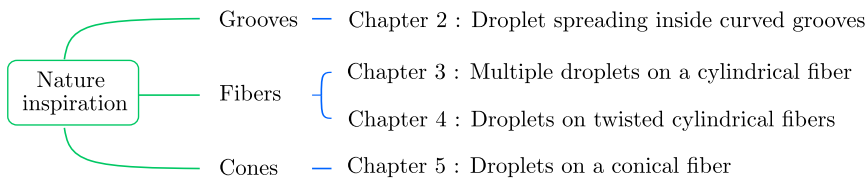
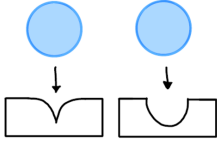


Figure 1.29: Outline of the following chapters. Inspired by natural observations, our research investigates the influence of various natural features. We analyze droplet spreading within curved grooves, droplet sliding along vertical fibers, and droplet movement on horizontal cones.



2

Droplet spreading inside curved grooves

In this chapter, we discuss the spreading of silicone oil droplets within curved grooves. Both curvatures are studied with convex and concave grooves, referred to as epicycle and hypocycle grooves. The radius of the grooves is varied. The spreading dynamic is different depending on the sign of the curvature. This chapter reveals that epicycle grooves are an important ingredient to efficiently spread totally wetting droplets. We present experimental data and a model to describe the observed spreading behaviors.

Partially published as

J. Van Hulle, and N. Vandewalle, *Effect of groove curvature on droplet spreading*, *Soft Matter* **19**, 4669 (2023).

M. Leonard, J. Van Hulle, F. Weyer, D. Terwagne and N. Vandewalle, *Droplets sliding on single and multiple vertical fibers*, *Phys. Rev. Fluids* **8**, 103601 (2023).

2.1 Motivations

A wetting liquid may spread spontaneously along a surface thanks to capillary driving forces [40]. This spontaneous motion is of primary importance in many fields. Biomedical applications with lab-on-chip device [101, 142], water delivery in microgravity [143] or also water collection in arid regions [135]. Even in our everyday life, capillarity governs the way a biscuit soaks up coffee or water absorbs into paper [144].

Several studies have examined capillary rise into different structures, or droplet spreading on specific substrates [38, 47, 145], as reviewed in Chapter 1. A general trend has been observed, the position of the advancing meniscus always follows a power law $x = ct^p$, where x is the position of the leading meniscus and t is time. The exponent value p depends on various experimental parameters: whether the volume of liquid is conserved or not, whether the transporting structure is open or closed, it also depends on the shape and size of this transporting structure, a literature review is proposed in Table 1.1. However, less attention has been dedicated to the effects of curvature.

When it comes to efficiency, nature is often a good source of inspiration since natural selection has shaped the best features over time. As reviewed in Chapter 1, many plant species that deal with water collection are decorated with curved grooves, such as the spines of the *Opuntia microdasys* cactus (see Fig. 1.22) [5], the trichomes of the insect trapping plant *Sarracenia* (see Fig. 1.23) [4] and the leaf of the Namib desert grass *Stipagrostis sabulicola* (see Fig. 1.24) [127]. In Fig. 2.1, we show a 3D representation of various textures observed on water-transporting organs of these plants. All organs have an overall conical shape and, along the fiber, one notices curved grooves. The conical geometry is known to passively transport the

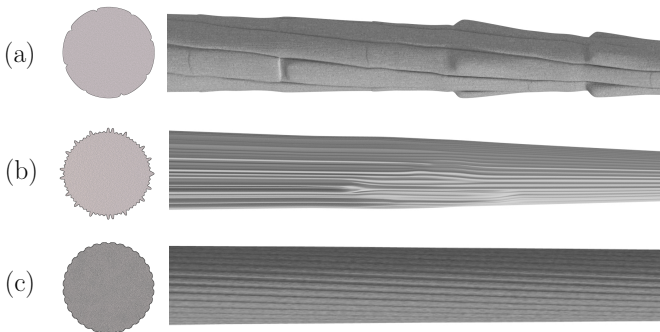


Figure 2.1: Representation of natural fibers found on several plants with the expected cross-sections of the fiber. Illustration of (a) a cactus spine observed on *Opuntia microdasys* [5], (b) a trichome of the insect trapping plant *Sarracenia* [4], (c) a leaf of the Namib desert grass *Stipagrostis sabulicola* [127]. All these structures are used by the plants to collect and drive water droplets. The ingredients are the same in each case, the fiber is conical and there are curved grooves along the fiber. The diameter of each natural fiber is approximately $35 \mu\text{m}$ for the *Opuntia microdasys* spine, $40 \mu\text{m}$ for the *Sarracenia* trichome and $250 \mu\text{m}$ for the *Stipagrostis sabulicola* leaf.

droplet along the fiber [99, 119] as soon as the droplets are captured which increases the water harvesting efficiency [16, 140, 146]. Then, the purpose of the grooves is also to enhance the water droplet motion by pre-wetting and keeping wet the fiber [4]. Two recent studies showed that curved grooves on synthetic conical fibers can also increase the liquid transport [122, 123], which will be described in Chapter 5. Notice, from the examples shown in Fig. 2.1, that curved grooves appear at different scales. In addition, two types of curved groove structures are observed. For Fig. 2.1 (a) and (c), the bumps appear wider than the hollows. For Fig. 2.1 (b) the bumps and the hollows have the same width. One can wonder what is the best groove’s geometry to spread droplets.

In the present chapter, we compare the influence of the curvature’s groove sign on the spreading dynamics of a droplet. In other words, we are searching for the curvature (convex or concave) that enhances the droplet spreading.

2.2 Experimental setup

A sketch of the experimental setup is provided in Fig. 2.2. The substrates are three-dimensionally (3D) printed with Object Prime 30 from Stratasys. The printer is jetting tiny polymers droplets which are cured with a UV lamp. The accuracy of a single layer is about $30\ \mu\text{m}$. The material used by the printer is Acrylonitrile Butadiene Styrene (ABS). The 3D-printing technique allows to tune the curvature’s sign as well as the radius R of the groove. We use grooves with R ranging from 0.5 mm to 2 mm. The radius R of the curved groove is sketched in Fig. 2.3 (a). This substrate is horizontal and a droplet of liquid is gently deposited in the middle of one groove. The droplet is produced by a micropipette (Eppendorf Xplorer). The liquid is silicone oil (Dow Corning) with a viscosity $\nu = 100\ \text{cSt}$. The surface tension is $\gamma = 20.6\ \text{mN/m}$ and the density is $\rho = 960\ \text{kg m}^{-3}$. The droplet volume is fixed at $\Omega = 5\ \mu\text{l}$. The static contact angle of silicone oil on ABS is very small, we are thus in the case of total wetting, $\theta_E \approx 0^\circ$. Prior to each experiment, the groove is cleaned with isopropanol and distilled water, then the surface is left to dry.

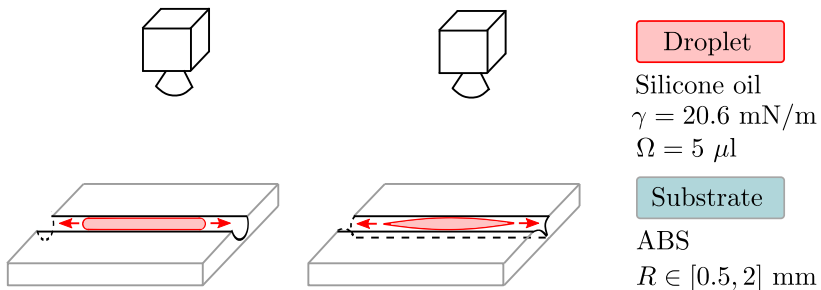


Figure 2.2: Sketch of the experimental setup. Grooves are printed along a flat substrate made of ABS. (left) The groove is concave, called hypocycle groove, (right) the groove is convex, called epicycle. A red-colored silicone oil droplet spreads inside the groove. The spreading is recorded with a camera above the horizontal groove. The radius of the grooves R ranges from 0.5 mm to 2 mm.

The droplet spreading is recorded from above thanks to a CCD camera (Charge-Coupled Device) at 20 fps. To improve the contrast as in Fig. 2.3, silicone oil is colored in red and we used two lights (Effilux) on each side of the groove. With an image treatment, the contour of the spreading droplet over time is detected (see Fig. 2.3 (c)). It allows to obtain the left and right positions of the advancing meniscus and so the spread x of the droplet along the groove. An experimental movie with the obtained contour is available with the QR code in Fig. 2.3 (d). The spreading is recorded after the droplet is completely inside the groove. For a given droplet volume Ω , the droplet completely fills the groove if the spread x is higher than the calculated filled spreading, $x > x_f = \Omega/S$ where S is the cross-section of the groove. Before the value x_f is reached the droplet sits around the groove with a spherical cap. These early stages of droplet spreading will not be described in the present study.

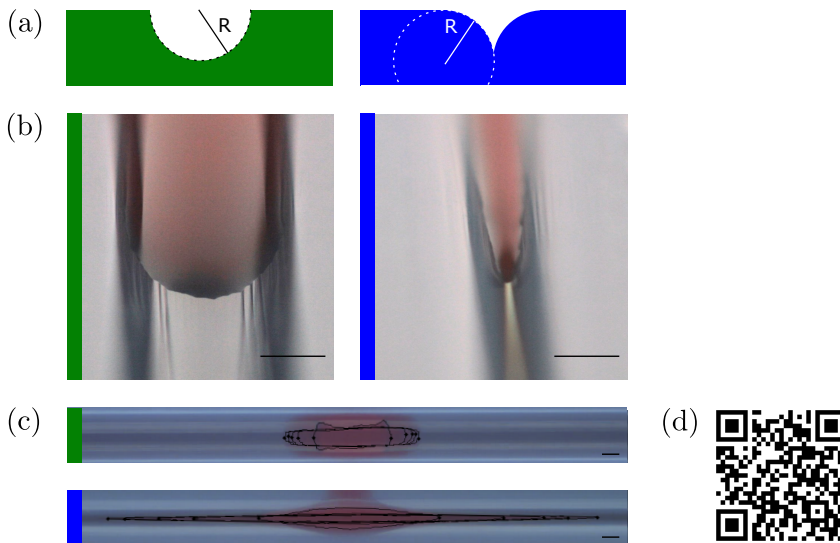


Figure 2.3: (a) Illustration of a hypocycle groove (left) and an epicycle groove (right). (b) Pictures of the liquid front in a hypocycle groove (left) and an epicycle groove (right). The radius of the groove is the same being $R = 1.37$ mm, as sketched above the pictures. The droplet is colored in red. One can observe that the shape of the advancing front of the droplet is impacted by the curvature of the groove. In a hypocycle groove, the droplet has a round advancing meniscus. In an epicycle groove, the droplet is pinched at the bottom of the groove. (c) Superposition of experimental pictures of a red-colored droplet spreading in a hypocycle groove (top) and in an epicycle groove (bottom) with the same radius $R = 1.37$ mm. The numerically found contour is in black. The time interval between successive contours is 5 s. The scale bars represent 1 mm. (d) QR code to access an experimental video comparing the spreading of a red-dyed silicone oil droplet in a hypocycle groove and in an epicycle groove. This video corresponds to (c).

2.3 Spreading characterization

When the droplet is in contact with the groove, the spreading becomes one directional. To investigate the crucial physical parameters, one can calculate several non-dimensional numbers. The capillary number compares surface tension effects to viscous ones, it is defined by $Ca = \dot{x}\nu\rho/\gamma$ where \dot{x} is the speed of spreading, ρ the density and γ the surface tension. In our case, we found $Ca \approx 2 \cdot 10^{-3}$ meaning that surface tension overcomes viscosity. The Weber number compares the inertial force to the surface tension force, we have $We = \rho\dot{x}^2L/\gamma$ with L the characteristic length of the system. In the present study, droplets are confined inside a millimeter groove, so we have $L \approx 10^{-3}$ m. For our experiments, the Weber number is typically $We \approx 2 \cdot 10^{-5}$, meaning that surface tension forces dominate inertial forces. The Reynolds number, $Re = \dot{x}L/\nu \approx 7 \cdot 10^{-3}$, compares inertial forces to viscous forces. This value reveals that viscous forces are larger than inertial ones. The Bond number compares gravitational forces to capillary forces, $Bo = \rho gL^2/\gamma \approx 0.5$, where g is the gravitational acceleration. It indicates that capillary forces are larger than gravitational ones. The capillary length is given by $l_c = \sqrt{\gamma/(\rho g)} = 1.5 \cdot 10^{-3}$ m. Therefore, in our system, the motion of the liquid inside the groove is driven by surface tension forces.

In Fig. 2.4, we plot a double logarithmic graph of the non-dimensional spread $(x - x_0)/l_c$ over time t for different curvatures. The value x_0 is the initial spread adopted by the droplet inside the groove. One can notice that all long time dynamics are given by power laws as expected. But the slopes are different depending on the sign of the curvature. The spread of a droplet inside an epicycle groove is going as time to the power one half. While inside a hypocycle groove, it spreads as time to the power one third. Then, we vary the radius R of the groove. We observe that the dynamic of a droplet inside an epicycle groove is independent of the radius as all curves collapse. However, for a droplet inside a hypocycle groove, the spreading clearly depends on the radius of curvature. We observe that the spreading increases as the radius decreases. From those first observations, one can say that the spreading can be enhanced in a hypocycle groove with a small radius. Nevertheless, a droplet spreading inside an epicycle groove wins any droplet race, with spreading factors one order of magnitude larger than in the case of hypocycles.

2.3.1 Hypocycle - concave

A droplet inside a hypocycle groove spreads along the direction given by the channel (see Fig. 2.3). This motion is led by surface tension acting along the contact line. The driving force can be expressed as

$$F_{\gamma,h} \sim \gamma x \theta_D^2 \quad (2.1)$$

where θ_D is the dynamical contact angle [19]. We can express this contact angle as $\theta_D \sim z/R$, where z is the height of the droplet that decreases as the droplet spreads, and is defined in Fig. 2.5 (a). In fact, as can be noticed in this figure, the front meniscus is curved. The characteristic length of this meniscus is assumed to

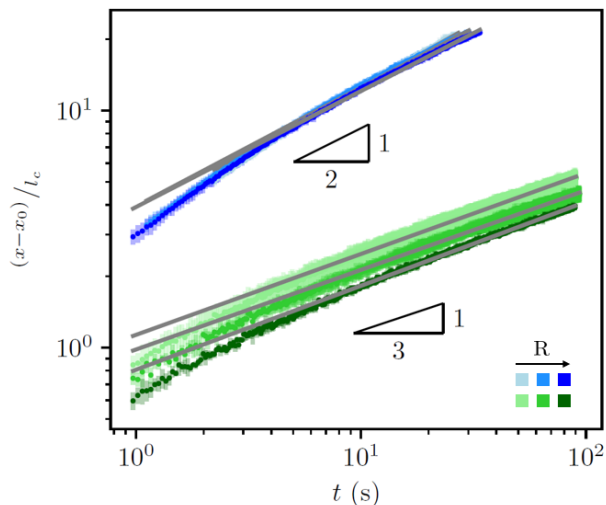


Figure 2.4: Double logarithmic graph of the non-dimensional spread $(x - x_0)/l_c$ as function of time t . In blue, the groove is an epicycle. In green, the groove is a hypocycle. The darker the color is, the larger the radius of the groove R (radius values are respectively 1.07 mm, 1.37 mm and 1.67 mm). The error bars coming from repeated experiments for each data set are in light color. One notices that the spread of a droplet inside an epicycle groove is independent of the radius R . However, for a hypocycle groove, the spread is faster for small radii. The grey lines are power law fits on experimental data, the fitting laws are described in section 2.3.

be the radius of the groove R . Hence, the driving force is given by

$$F_{\gamma,h} \sim \gamma x \frac{z^2}{R^2} \quad (2.2)$$

Since the dissipation occurs in the bulk of the droplet, the dissipation force is then given by

$$F_{\eta,h} \sim \nu \rho x \dot{x} \quad (2.3)$$

where \dot{x} is the spreading speed. By balancing both forces and looking at the stationary equation, one can obtain the expression of the spreading speed, $\dot{x} \sim \frac{\gamma}{\nu \rho} \frac{z^2}{R^2}$. By assuming the volume of the droplet is $\Omega \sim xzR$. Therefore, the speed is expressed as $\dot{x} \sim \frac{\gamma}{\nu \rho} \frac{\Omega^2}{x^2 R^4}$. This leads to the following expression of the spread over time

$$x \sim \left(\frac{\gamma}{\nu \rho} \frac{\Omega^2}{R^4} t \right)^{1/3}. \quad (2.4)$$

This model gives the scaling law to describe the spreading. It predicts a power law of time to the power one third as observed experimentally. In fact, this model is an adaptation of Tanner's model that describes the spreading of a droplet on a smooth surface. Here, we have a 1D version of that model where the driving force, as well as the volume of the droplet, are rewritten to take into account the confinement of the droplet inside the 1D groove.

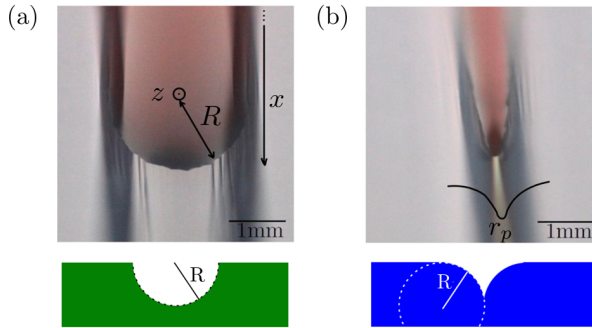


Figure 2.5: Pictures of the advancing contact line of a red-colored silicone oil droplet spreading in curved grooves. (a) In a hypocycle groove, the advancing meniscus of the droplet is curved, describing an advancing contact angle that decreases as the droplet spreads. The advancing contact angle is approximated by the ratio of the height of the droplet z and the curvature of this meniscus, which is approximated by the groove radius R . (b) In an epicycle groove, the advancing meniscus of the droplet is pinched at the cusp of the groove. This creates a confined advancing meniscus that leads the dynamics, its characteristic length is given by the resolution of the 3D printer, r_p , which governs the size of the cusp.

2.3.2 Epicycle - convex

A picture of a droplet spreading inside an epicycle groove is shown in Fig. 2.3 (c). One can notice that the advancing contact line of the droplet is pinched at the cusp of the epicycle (Fig. 2.3 (b)). There, the fastest spreading takes place, therefore this point dominates the dynamic. As the front meniscus is in contact with the cusp of the groove, the driving force is expressed as

$$F_{\gamma,e} \sim \gamma r_p \quad (2.5)$$

where r_p is the accuracy of the 3D printer. In fact, the advancing front is confined inside the bottom of the groove where the characteristic length scale is fixed by the layer deposition accuracy of the 3D printer, as illustrated in Fig. 2.5 (b). In our system, we have $r_p \approx 30 \mu\text{m}$. The dissipation occurs in the bulk of the droplet. The dissipation force is thus given by

$$F_{\eta,e} \sim \nu \rho x \dot{x}. \quad (2.6)$$

The spread is obtained by balancing the forces. The expression of the spread x of the droplet over time is therefore given by

$$x \sim \left(\frac{\gamma}{\nu \rho} r_p t \right)^{1/2}. \quad (2.7)$$

This scaling model is based on the BCLW model (see section 1.3.4). It corresponds to the case of a closed capillary tube with the size of the cusp r_p .

2.3.3 Analysis

In the previous sections, we proposed two models for the spreading of a droplet inside each type of groove. We can fit the experimental data with the equations of each curvature (Eq. (2.4) and Eq. (2.7)). The fitting law is a power law, $x/l_c = ct^p$ with two fitting parameters, being the coefficient c and the power p . In Fig. 2.4, the grey lines are the adjustment of the power law on the data. These fits capture the overall trend of the spreading process effectively. Please notice that the scaling law deviates from the experimental data during the initial seconds of the experiment. We attributed this deviation to a change in regime, the transition from the droplet filling the groove to a regime where the volume inside the groove is constant, as discussed in section 2.2. The observed deviation is an indication of the time range during which the regime transition affects the dynamic. Our models describe the spreading behavior for a constant volume, which is applicable to later time periods.

In Fig. 2.6 (a), we plot a graph of the fitting parameter p , the power of the fitting power law, as a function of the groove's radius R . For both the hypocycle and the epicycle groove, the parameter p is independent of the radius of the groove. We found a power one third for the hypocycle groove and a power one half for the epicycle. The models proposed in the previous subsections are in excellent agreement with the experimental data.

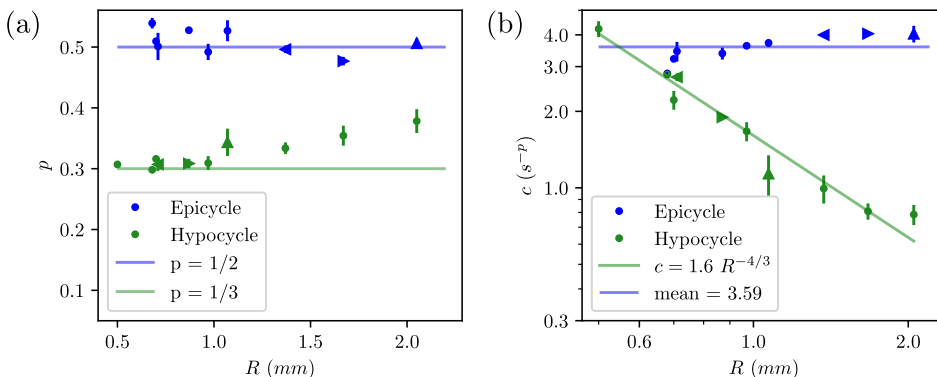


Figure 2.6: (a) The fitted exponent p as a function of the radius R of the groove. For both curvatures, the exponent p is independent of the radius. It has two distinct values, one half for the epicycle and one third for the hypocycle. (b) Double logarithmic graph of the fitted prefactor c as a function of the radius R of the groove. The error bars are smaller than the size of the symbols. For the epicycle, the parameter c is independent of the groove's radius. For the hypocycle, the parameter c follows a decreasing power law of the radius. The triangular markers correspond to the same cross-section of the groove (left triangle $S = 0.8 \text{ mm}^2$; right triangle $S = 1.2 \text{ mm}^2$; up triangle $S = 1.8 \text{ mm}^2$).

In Fig. 2.6 (b), we plot a double logarithmic graph of the fitting parameter c as a function of the groove's radius R for both curvatures. Firstly, for the hypocycle case, the coefficient c of the power law exhibits a decreasing trend with the radius

R of the groove. This trend can itself be fitted,

$$c_h = a_h R^{-4/3} \quad (2.8)$$

with $a_h = 1.6 \text{ mm}^{4/3} \text{ s}^{-1/3}$. The model proposed in section 2.3.1 gives the Eq. (2.4) where the spread is decreasing with the good dependency of the radius. We have

$$c_h = \frac{1}{l_c} \left(\frac{\gamma}{\nu\rho} \Omega^2 \right)^{1/3} R^{-4/3}. \quad (2.9)$$

Then, the prefactor a_h provided by the model is $a_{h,model} = \frac{1}{l_c} \left(\frac{\gamma}{\nu\rho} \Omega^2 \right)^{1/3} = 12 \text{ mm}^{4/3} \text{ s}^{-1/3}$, it overestimates the experimental value as no geometrical factors were taken into account in our model. Nevertheless, the model gives the good power as well as the right dependency for R .

Secondly, for the epicycle groove, the coefficient in front of the power law is independent of the radius of the groove. This can be understood as the droplet is pinched at the cusp of the groove where the characteristic length is governed by the accuracy of the 3D printer. The model obtained in section 2.3.2 gives the equation Eq. (2.7) which recovers this independence of the groove's radius. We have

$$c_e = \frac{1}{l_c} \left(r_p \frac{\gamma}{\nu\rho} \right)^{1/2}. \quad (2.10)$$

The value of this coefficient is $c_e = 1.7 \text{ s}^{-1/2}$ which is the same order of magnitude as the mean value obtained in Fig. 2.6 (b).

The influence of the cross-section of the groove is depicted by the triangular markers in Fig. 2.6 (a) and (b). One observes that these data can be analyzed by considering the radius of the groove.

The models explained in section 2.3.1 and 2.3.2 are in excellent agreement with the experimental data. In both cases, we use the expression of bulk dissipation. The difference between both models appears in the expression of the driving force. This driving force takes into account the specific shape of the droplet adopted inside the groove. Different shapes lead to two distinct dynamics.

2.4 Application

To compare the spreading efficiency of both groove types, we have created the logo of our University with either epicycle grooves or hypocycle grooves. To compare both structures, we kept as a constant the cross-section, $S = 0.8 \text{ mm}^2$. Meaning the radius of the epicycle groove is larger than the hypocycle one. The experimental pictures are shown in Fig. 2.7. A droplet is dropped off at the same spot on both logos, the droplet is colored in black. After 170 s, the logo made with epicycle grooves is completely filled, and the logo is highlighted by the droplet. While, during this same lapse of time, the logo made with hypocycle grooves is more or less still half filled. This simple experiment proves that spreading can be enhanced

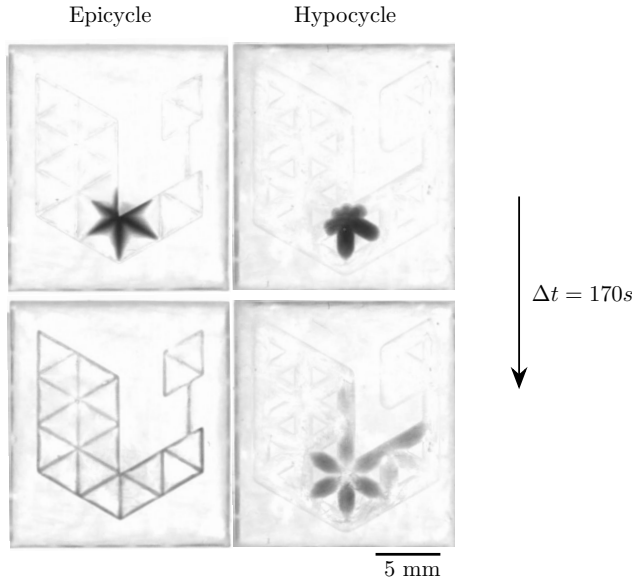


Figure 2.7: The logo of the University of Liège is a triangular lattice. By using epicycle grooves (left) or hypocycle grooves (right), a droplet colored in black spreads inside the network. Both grooves have the same cross-section, $S = 0.8 \text{ mm}^2$ (epicycle's radius: $R = 1.37 \text{ mm}$ and hypocycle's radius: $R = 0.71 \text{ mm}$). In the epicycle case, the logo is filled after 170 s. However, during this same lapse of time, the hypocycle logo is half filled.

using the right curvatures of the grooves. One could imagine microfluidics devices based on this groove avoiding the use of pumps.

This research is in line with water collection problems. In fact, the findings of this study have potential applications in improving water collection in arid regions. Large meshes of cylindrical fibers show good efficiency in fog catching. The structure is made with either an intermingling of fibers [130, 9] or with harps made of vertical fibers [134, 136]. One could imagine to add curved grooves on the fibers in order to increase the drainage. In fact, the groove spreads the liquid and retains it as a film which should decrease the friction. Better than that, it has recently been shown that the epicycloid structure of the fiber allows droplets to go down faster [147], this assertion is further discussed in the next section. Moreover, the first step of any fog catcher is the initialization time, this is when the net is capturing liquid without draining it [148]. Simply by adding curved grooves on the fiber, this onset time should decrease.

2.5 Grooved fibers

This section reviews the article [147], which studies one perspective of epicycle grooves by using these grooves on fibers to improve droplet drainage.

One key takeaway from the above analysis is that epicycle grooves are more effective at rapidly spreading a droplet. Actually, convex grooves, such as epicycle grooves, can be easily built using two cylindrical fibers placed side by side. This arrangement creates two convex grooves on each side, as illustrated in the cross-sectional view in Fig. 2.8 (a). Does a droplet descend faster on such a bundle of fibers than on a single fiber with the same equivalent diameter? The answer is yes. Fig. 2.8 (b) shows the speed of the descending silicone oil droplet \dot{z} on vertical fibers as a function of its volume Ω . As the droplet slides down, its volume decreases due to the formation of a thin liquid film left behind (see LLD theory in section 1.4.2). The graph compares the speed of droplets sliding on a single fiber (light color) with those on a bundle of two fibers with the same equivalent diameter (dark color). The diameter of each fiber in the bundle is half the diameter of the single fiber case. The graph indicates that, for a given droplet volume, the droplet descends faster on a bundle of two fibers than on a single fiber [147]. Furthermore, Fig. 2.8 (c) presents two superpositions of pictures with the same time interval between successive frames, demonstrating that a droplet on a bundle of two fibers (right) travels further in the same time interval compared to one on a single fiber (left).

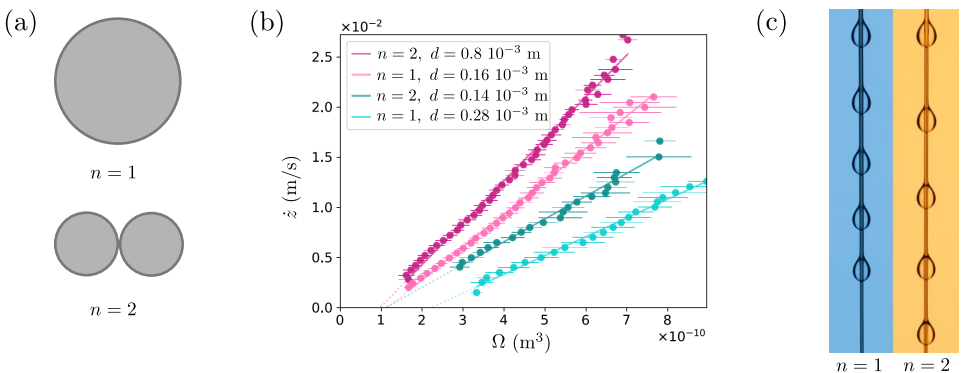
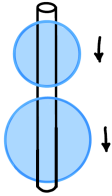


Figure 2.8: (a) Illustration of the cross-sectional view of a single fiber (case $n = 1$) and a bundle of two fibers (case $n = 2$). (b) Graph of the silicone oil droplet speed \dot{z} as a function of the droplet's volume Ω . The light color corresponds to the case of a single fiber ($n = 1$) and the dark color to the case of a bundle of two fibers ($n = 2$) with the same equivalent diameter. The graph is taken from [147]. (c) Superposition of pictures with the same time interval between successive images (credit: M. Leonard). On the left, the droplet slides on a single fiber ($n = 1, d = 0.28$ mm); on the right, it slides on a bundle of two fibers with the same equivalent diameter ($n = 2, d = 0.14$ mm). A droplet on a bundle of two fibers travels further in the same time interval compared to one on a single fiber.

2.6 Conclusion

A study of curved grooves effect on the droplet spreading dynamics has been performed. A 3D printer is used to manufacture the grooves, it allows to choose easily the radius of curvature. A droplet spreading in a curved groove adopts a different shape depending on the sign of the curvature. Specifically, we observed that the advancing contact line is curved for the hypocycle groove (concave), while the front of the liquid is pinched inside the cusp of the groove for the epicycle groove (convex). This leads to different spreading dynamics. In both cases, the droplet spreads with a power law. For the hypocycle groove, the power is one third and the pre-factor decreases with the power law of the groove's radius. For the epicycle groove, the power is one half, which is higher than the hypocycle case, and the pre-factor is independent of the groove's radius. We proposed two models inspired from Tanner's and BCLW's models that predict these powers and pre-factors. Notice that both powers encountered are greater than the one of a droplet spreading on a flat surface (power $1/10$). Therefore, grooved structures favor any droplet spreading. Consequently, it is not surprising to find such kind of structures on plants living in arid regions, as illustrated in Fig. 2.1, in section 2.1 [5, 4, 127]. Our study reveals that epicycle grooves are more efficient to spread droplets, with in the power law a higher exponent and a larger pre-factor. Epicycle grooves seem similar to the large bumps and small hollows observed on some natural fibers, see Fig. 2.1 (a) and (c). Further biological research could verify this hypothesis. In conclusion, our study provides a comparison between two ways of spreading droplets and offers many new perspectives.



3

Multiple droplets on a cylindrical fiber

In this chapter, we investigate the dynamics of a droplet on a smooth vertical cylindrical fiber. As the droplet descends, it coats the dry fiber with a thin liquid film. This coating destabilizes to form smaller droplets that also slide downwards on the wet fiber. We model both the initial droplet and the subsequent droplet dynamics. The merging of droplets is observed. We theoretically predict the number of droplets created at the deposition location.

These experiments have been performed in the Pan Lab at Waterloo University in collaboration with Zhao Pan.

3.1 Introduction

The study of droplet and fiber interaction is a vast research area spanning across both static and dynamic studies. Herein we focus on dynamic processes. The dynamics of a barrel-shaped droplet sliding along a vertical or inclined fiber is described in [98] and is reviewed in section 1.4.5. A coating liquid film on a fiber is known to destabilize through the Rayleigh-Plateau instability [23], leading to the formation of small droplets on the fiber. Furthermore, Quéré further provided a cutoff value of the film thickness below which a film on a vertical fiber remains stable [83]. Yet, some mysteries are still to be unraveled. In particular, Quéré *et al.* highlighted in [149] a predator/prey-like interactions between droplets on fibers resulting from the Rayleigh-Plateau instability: "When [...] the film is thick [...], drops appear quickly and fall along the fiber. If one drop is slightly larger than the other, it falls faster and in passing swallows the rest". This behavior is shown in Fig. 3.1. To our knowledge, this behavior has not been further studied.

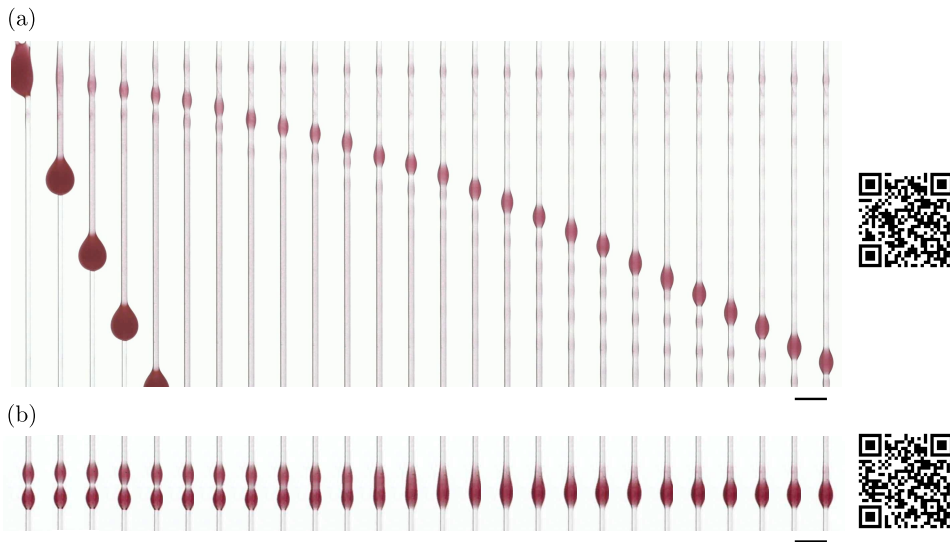


Figure 3.1: (a) Red dyed silicone oil droplet descending a vertical nylon fiber. The time interval between each image is 0.68 s. As the droplet slides down, a liquid film is left behind. The thickness of this liquid film is larger when the droplet speed is larger. Therefore at the release point of the initial droplet, the so-called mother droplet or generation 0, the film is the thickest. The Rayleigh-Plateau instability takes place which creates a tiny new droplet, termed as daughter droplet or generation 1. This daughter droplet slides on the film left by the mother droplet. Both motions are different. (b) At a given time and a given position, the two generations will meet. The mother droplet is under and the daughter droplet is above. The time interval between each image is 0.017 s. One observes that the daughter droplet finally catches the mother droplet, leading to a merging of both droplets. The experimental data for (a) and (b) are the same, $\Omega = 5 \mu\text{l}$, $\nu = 100 \text{ cst}$ and $d = 0.3 \text{ mm}$. The scale bars correspond to 2 mm. QR codes on the right side give access to the corresponding experimental videos.

We aim to study the residual liquid film a descending droplet produces along a vertical dry fiber. Focusing on predator/prey behavior in light of all the knowledge we have on the topic of droplets on fibers. We focus on the case of a single droplet descending along a dry fiber. As the droplet descends, it leaves a non-uniform liquid film behind. This residual film may undergo a Rayleigh-Plateau destabilization, forming subsequent droplets. These newborn droplets slide on the liquid film left by the previous droplet. One aims to describe the dynamic of these subsequent droplets and predict the number of droplet generations created at the release point of the first mother droplet.

3.2 Methods

The fibers used in the experiments are made of nylon (fishing thread) and are fixed vertically. These fibers have a circular cross-section with diameters ranging from $d = 0.2$ mm to $d = 0.45$ mm. The liquid used is silicone oil with kinematic viscosities of $\nu = 50$ cSt and $\nu = 100$ cSt. The droplets are deposited on the fiber using a syringe (Eppendorf Xplorer). The tested volumes are $\Omega = 3, 5$ and $7 \mu\text{l}$. To enhance contrast, the silicone oil is dyed red, and a white lighting source is positioned behind the fiber. Prior to each experiment, the fiber is cleaned with isopropanol and distilled water and let to dry. Each experiment is conducted five times.

The motion of the droplets is recorded with a CCD camera positioned in front of the fiber. The camera setup allows a field of view of 13 cm while still capturing the millimeter-scale droplets. The positions of the droplets z over time t are extracted using a Python script.

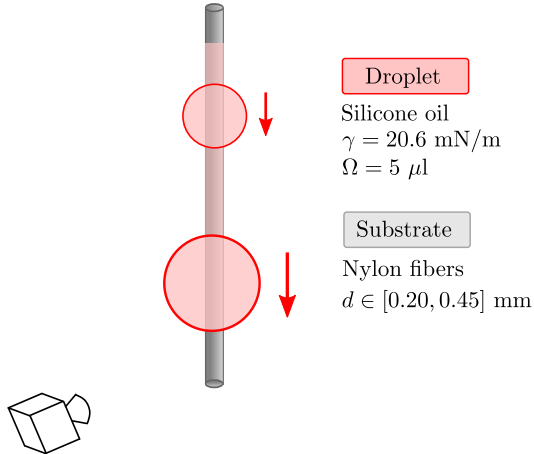


Figure 3.2: Sketch of the experimental setup. A cylindrical fiber stands vertically and a $5 \mu\text{l}$ red-colored droplet with a barrel shape descends along it. A liquid film is left at the rear of the droplet and may destabilize into a new droplet, which also descends along the now wet fiber. These descents are recorded with a camera placed in front of the fiber. The diameter of the fiber d ranges from 0.20 mm to 0.45 mm.

3.3 Results

A first droplet is deposited on a dry fiber and is referred to as generation 0 or the "mother" droplet. As this droplet descends along the vertical fiber, it coats the fiber with a liquid film, as observed in the experimental pictures in Fig. 3.1 (a). Due to the droplet losing volume as it travels, its speed decreases. The thickness of the resulting film is directly related to the droplet's speed, the higher the speed, the thicker the film. Consequently, the droplet leaves a non-uniform film along the fiber, with the thickest film located close to the initial deposition point. A liquid film on a fiber tends to minimize its energy through the Rayleigh-Plateau instability, creating droplets from the film. These subsequent droplets are created along the path where the mother droplet (generation 0) has traveled. Since the film is thickest at the initial release point, the first new droplet forms rapidly here. This new droplet, referred to as generation 1 or the first "daughter" droplet, slides along a non-uniform wet fiber (the liquid film left by the previous mother droplet) and engulfs other potential droplets of the same generation in its path due to their slower growth, which results from the thinner liquid film. In Fig. 3.1 (a) one observes the liquid destabilization that takes a longer time on the lower part of the fiber. As generation 1 moves, it also leaves a liquid film behind, potentially enabling the formation of a second generation.

A distinction is made between generation 0 and the following generations. Generation 0 slides on a dry fiber, while generations 1 and beyond slide on a wet fiber. This difference results in distinct dynamics for generations 0 and 1. Notably, it is observed that both generations merge after traveling a certain distance, as shown in Fig. 3.1 (b). The mother droplet and the daughter droplet are destined to meet again, and it is only a matter of time before it occurs. At the merging position, the droplets accelerate, creating a thicker liquid film at the point of merging, as observed and analyzed in [118]. The merging may therefore initiate a new cycle of generations.

The case study of this chapter focuses on a single droplet descending a fiber, which is to be distinguished from studies where a constant flow rate is applied at the top of the fiber, see section 1.4.4 of the State of the Art. In cases of imposed flow rate, the descending coating also destabilizes into droplets. The interplay between the flow rate, fiber radius and nozzle diameter determines the emergence of three regimes [91, 85, 87, 88]: the isolated droplet regime or dripping state, where primary droplets are spaced evenly, move at a constant speed and coalesce with smaller secondary beads (secondary breakup of the thin film) in a cyclic pattern [89], (b) the steady Rayleigh-Plateau regime, characterized by a regular sequence of closely spaced and periodic droplets descending the fiber at constant speed and spacing, without collisions, (c) the unsteady and convective regime characterized by random coalescence events where primary droplets merge to form larger droplets, which then coalesce with subsequent primary beads, resulting in an irregular overall bead pattern. This research inscribes in the isolated droplet regime due to the small liquid input rate, but it differs significantly in that the incoming rate is not constant, setting it apart from those case studies.

In our experiments, the motion of the droplet is affected by gravity as revealed when calculating the Bond number $\text{Bo} = \rho g L^2 / \gamma$, where ρ is the fluid density, g is the gravitational acceleration, L is the characteristic length of the droplet and γ is the surface tension. Taking $L \sim 10^{-3}$ m, yields $\text{Bo} = 0.46$, indicating that both gravity and surface tension influence the droplet motion. The Capillary number compares viscous effects to surface tension ones and is given by $\text{Ca} = \nu \rho \dot{z} / \gamma$, where ν is the kinematic viscosity and \dot{z} is the droplet's vertical speed. The maximum speed measured in our experiments is $\dot{z} = 0.025$ m/s for $\nu = 50$ cSt, leading to $\text{Ca} = 0.06$. This low Capillary number suggests that surface tension forces dominate over viscous forces. The Weber number, defined as $\text{We} = \rho \dot{z}^2 L / \gamma$, compares inertial effects to surface tension and is significantly smaller than one (10^{-2} or less) across all the experimental parameters tested in this study, indicating the dominance of surface tension over inertial forces. Finally, the Reynolds number is given by $\text{Re} = \dot{z} L / \nu = 0.5$, which indicates that inertial effects are comparable to viscous effects and may play a role in the droplet's dynamic.

3.4 Discussion

We focus on the dynamics of both generations 0 and 1. All generations beyond 1 are expected to follow a similar trend as generation 1. The positions of the recorded generations are shown in Fig. 3.3, where lighter colors indicate higher generation numbers. The dynamics of droplet generation 0 differ from those of subsequent generations. Generation 1 is formed at the initial position of the mother droplet. Generations 1 and 2 exhibit a similar trend characterized by an accelerating phase followed by a decelerating phase. We begin our analysis by describing the dynamics of generation 0.

3.4.1 Mother droplet

Generation 0, or the mother droplet, refers to the initial droplet descending on a dry vertical fiber. The dynamic of this droplet has been studied by Gilet *et al.* [98] and is re-explained in this section. The droplet descends the dry fiber driven by its weight $W = \rho g \Omega_0$. Opposing this driving force is a dissipative force, $F_\nu = \nu \rho d v \xi_{dry}$ with ξ_{dry} a parameter which describes the dissipation of the droplet on a dry fiber. This dissipation parameter is given by $\xi_{dry} = \pi C_v \frac{L}{l} \Gamma$, where C_v is a coefficient, L/l is the aspect ratio of the droplet (length to width), and Γ is a logarithm factor introduced by de Gennes [40]. Balancing these forces gives the speed of the mother droplet

$$\dot{z}_0 = \frac{g}{\xi_{dry} \nu d} \Omega_0, \quad (3.1)$$

where the subscript 0 refers to generation 0. As the droplet descends, it loses volume at a rate given by

$$\dot{\Omega}_0 = -\pi d e_0 \dot{z}_0, \quad (3.2)$$

where e_0 is the thickness of the liquid film left behind the droplet, which depends on the droplet's speed and the fiber diameter. This film thickness is given by the

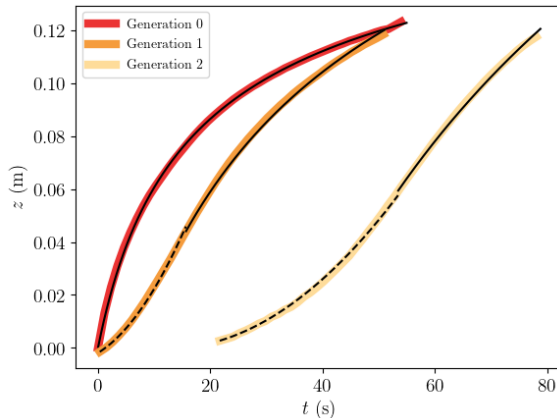


Figure 3.3: Vertical position z over time t of a droplet sliding along a straight fiber, with different colors representing different generations. The red color refers to generation 0 or the mother droplet, the orange color represents generation 1 or the first daughter droplet, and the yellow color corresponds to generation 2, or the granddaughter droplet. The solid lines are fits of Eq. (3.6) for generation 0 and Eq. (3.15) for generations 1 and 2. The dashed line is the fit of Eq. (3.11). These models describe effectively the different dynamics for all generations. The positions of each droplet tend to converge towards the same value, indicating the merging of the droplets. After this merging event, the refilled mother droplet continues its descent. The experimental conditions for this graph are a droplet volume $\Omega = 5 \mu\text{l}$, viscosity $\nu = 50 \text{ cSt}$, and fiber diameter $d = 0.35 \text{ mm}$.

Landau-Levich-Derjaguin theory [150] adapted for a cylindrical fiber as provided in [81],

$$e_0 = c_{dry} d \left(\frac{\nu \rho}{\gamma} \dot{z}_0 \right)^{2/3}, \quad (3.3)$$

where c_{dry} is a coefficient, with theoretical developments leading to $c_{dry} = 0.67$ [81]. The film thickness depends on the droplet speed, which decreases as the droplet descends along the vertical fiber, resulting in a non-uniform film. Using all these relationships, the following differential equation is obtained

$$\ddot{z}_0 = -w_0 \dot{z}_0^{5/3}, \quad (3.4)$$

with

$$w_0 = \pi \frac{c_{dry} g}{\xi_{dry} \nu} d \left(\frac{\nu \rho}{\gamma} \right)^{2/3}. \quad (3.5)$$

Solving this equation yields

$$z_0 = \frac{\dot{z}_{0,i}^{1/3} - \left(\dot{z}_{0,i}^{-2/3} + \frac{2}{3} w_0 t \right)^{-1/2}}{w_0/3}, \quad (3.6)$$

where $\dot{z}_{0,i}$ is the initial speed of the droplet generation 0. The model accurately depicts the observed dynamic for generation 0, as shown in Fig. 3.3 (solid line). The

	ξ_{dry}	ξ_{wet}	c_{dry}	c_{wet}
$\nu = 50$ cSt	173	95	1.42	0.39
$\nu = 100$ cSt	173	95	1.84	0.48

Table 3.1: Table comparing the values of ξ and c for different fiber states (dry and wet) and fluid viscosities. The parameter ξ is estimated using theoretical calculations (see, Eqs. (3.7) and (3.8)), while the coefficient c is obtained from the fitted prefactor ξ/c and the theoretical estimation of ξ for both dry and wet conditions. Both ξ and c are smaller in the wet state compared to the dry state.

experimental conditions are the same as in [98]. The initial speed is obtained by adjusting a slope at the beginning of the trajectory, with an arbitrary choice to fit the first 50 experimental data points. The factor c_{dry}/ξ_{dry} is unknown and used as a fitting parameter. This parameter is plotted in Fig. 3.4 as a function of the fiber diameter d and for several droplet volumes Ω and fluid viscosity ν . This prefactor is found to be independent of the diameter of the fiber, slightly dependent on the droplet volume, and increases with the viscosity. The mean value of c_{dry}/ξ_{dry} is 0.008 for $\nu = 50$ cSt and 0.011 for $\nu = 100$ cSt. According to [40] and [147], the friction coefficient ξ can be estimated by integrating the dissipation over both the front and the rear of the droplet, leading to

$$\xi = C_v \pi \frac{L}{l} \Gamma, \quad (3.7)$$

with

$$\Gamma = \ln \left(\frac{L^2}{4a_f a_r} \right), \quad (3.8)$$

where a_f and a_r are the shortest lengths at the front and rear of the droplet, respectively. At the front, where the droplet is in contact with a dry fiber, a_f is estimated to be around 10^{-9} m [40]. At the rear, a liquid film is left, with a thickness approximated as $a_r \approx 10^{-5}$ m. In the literature, values of $C_v = 1$ and $L/l = 3$ are found [98, 147]. Considering a droplet length of $L = 2 \cdot 10^{-3}$ m, we obtain $\Gamma = 18$ and thus $\xi_{dry} = 173$. The logarithm factor for a dry surface is typically accepted to be $\Gamma = 15$ [41, 99], and ξ_{dry} values reported in [147] are in the same range as the value obtained here. The value of c_{dry} can therefore be found, yielding $c_{dry} = 1.42$ for $\nu = 50$ cSt and $c_{dry} = 1.84$ for $\nu = 100$ cSt. In [98], similar values were found, with $c_{dry} = 1.5$. The obtained values of ξ_{dry} and c_{dry} are summarized in Table 3.1. The value of c_{dry} will be used in section 3.4.3 to predict the number of generations created.

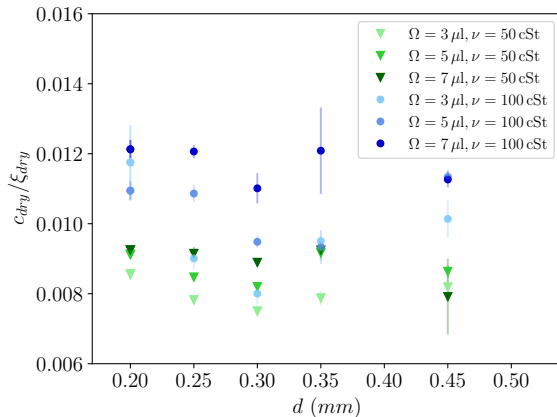


Figure 3.4: Fitted prefactor c_{dry}/ξ_{dry} from Eqs. (3.6) and (3.5) as a function of the fiber diameter d , for different volumes Ω and fluid viscosities ν . This prefactor is independent of the fiber diameter. However, the prefactor increases with both the droplet volume and the fluid viscosity.

3.4.2 Daughter droplet

Generation 1 is the first droplet formed due to the Rayleigh-Plateau instability. This droplet slides on a non-uniform liquid film left by the previous generation (0, mother). The dynamic of this new generation droplet differs from the previous one, as illustrated in Fig. 3.3. In the first instance, this droplet grows by accumulating liquid from the film on which it slides. This process is observed in Fig. 3.1 (a), where the generation 1 droplet grows in volume as it descends. This first regime is called the "growth phase" as the new droplet feeds from the liquid film left by the previous droplet. Although the droplet also leaves a liquid film behind, the film is relatively thin compared to the one in front of the droplet due to the droplet's lower speed at this stage. As the droplet travels a certain distance, it begins to lose more liquid at its rear than it gains at its front. This is because the coating film is not uniform; it is relatively thick near the initial release point and becomes thinner further along the fiber. The growth phase ends and the droplet enters a new phase, termed the "decline phase". In Fig. 3.3, the change in curvature of the droplet's position over time clearly indicates the transition from an accelerating phase to a decelerating one. The decline phase mirrors the dynamics observed in the mother droplet. Here under we propose two models to describe these distinct regimes.

Growth phase The forces acting on the generation 1 droplet are similar to those acting on the mother droplet, except that the dissipative coefficient is reduced because the droplet slides on a liquid film. The dissipative coefficient for this generation is written ξ_{wet} . The speed of the first daughter droplet is therefore given by

$$\dot{z}_1 = \frac{g}{\xi_{wet}\nu d}\Omega_1, \quad (3.9)$$

where the subscript 1 refers to the first generation. As the droplet slides, its volume, Ω_1 , increases. The droplet gains volume from the liquid coating in front of it while losing a negligible amount at its rear. The rate of volume gained is expressed as

$$\dot{\Omega}_{1,growth} = +\pi d \frac{\bar{e}_0 z_{tr}}{t_{tr}}, \quad (3.10)$$

where \bar{e}_0 is the average film thickness left by the previous droplet, z_{tr} and t_{tr} are the length and time over which the droplet grows. By combining Eq. (3.9) and Eq. (3.10) we obtain,

$$z_{1,growth} = \frac{1}{2} (At^2 + 2\dot{z}_{1,i}t + 2z_{1,i}), \quad (3.11)$$

with A a parameter given by

$$A = \pi \frac{g}{\xi_{wet} \nu} \frac{\bar{e}_0 y_{tr}}{t_{tr}}. \quad (3.12)$$

To fit the model to the growth phase of the data, \bar{e}_0 is used as a fitting parameter, while the initial speed $\dot{z}_{1,i}$ is determined by fitting a slope on the first 5% of the data corresponding to the growth phase. The position z_{tr} and time t_{tr} are related to the transition between regimes and are extracted from the experimental data, as explained at the end of this section. This model captures well the initial part of the droplet's trajectory, as shown by the dotted line in Fig. 3.3. Once the liquid film is no longer thick enough to sustain the increase in droplet volume, the droplet transitions into a different phase where its volume begins to decrease.

Decline phase In this second phase, the droplet loses more liquid at its rear than it gains at the front from the fiber coating. To describe this dynamic, we neglect the input from the front of the droplet since the output at the rear dominates. The model is therefore similar to the one of Gilet *et al.*, which was used to describe the mother droplet. The rate of volume loss is given by,

$$\dot{\Omega}_{1,decline} = -\pi d e_1 \dot{z}_1, \quad (3.13)$$

where e_1 is the film thickness left at the rear of the generation 1 droplet. This thickness is expressed as

$$e_1 = c_{wet} d \left(\frac{\nu \rho}{\gamma} \dot{z}_1 \right)^{2/3}, \quad (3.14)$$

with c_{wet} being a coefficient. Combining Eqs. (3.9), (3.13) and (3.14), yields

$$z_{1,decline} = \frac{\dot{z}_{1,max}^{1/3} - \left(\dot{z}_{1,max}^{-2/3} + \frac{2}{3} w_1 (t - t_{tr}) \right)^{-1/2}}{w_1/3} + z_{tr}, \quad (3.15)$$

where $\dot{z}_{1,max}$ is the maximal speed of the droplet, achieved at the transition from the growth phase to the decline phase, with z_{tr} and t_{tr} the coordinates of this maximal slope, and with w_1 a coefficient given by

$$w_1 = \pi \frac{c_{wet} g}{\xi_{wet} \nu} d \left(\frac{\nu \rho}{\gamma} \right)^{2/3}. \quad (3.16)$$

This model is fitted on the experimental data in the decline phase, as shown in Fig. 3.3 (solid line), with c_{wet}/ξ_{wet} a fitting parameter. The dynamic observed in this phase is similar to the one of the generation 0 droplet.

In order to adjust the models, the experimental data has to be divided into a growth and decline phase. It is achieved by identifying the point of maximum slope that separates the accelerating and decelerating portions of the trajectory. The position and time at which the transition occurs are denoted z_{tr} and t_{tr} , respectively and are plotted as a function of the diameter in Fig. 3.5 (a) and (b). The transition position is observed to increase as the fiber diameter decreases and is independent of the droplet volume and liquid viscosity. The time before the transition increases with higher viscosity, lower volume, and thinner fiber diameter. In some experimental conditions, the droplet may move too quickly or too slowly, resulting in insufficient data to allow for a meaningful fit. In such extreme cases, the data are excluded from fitting.

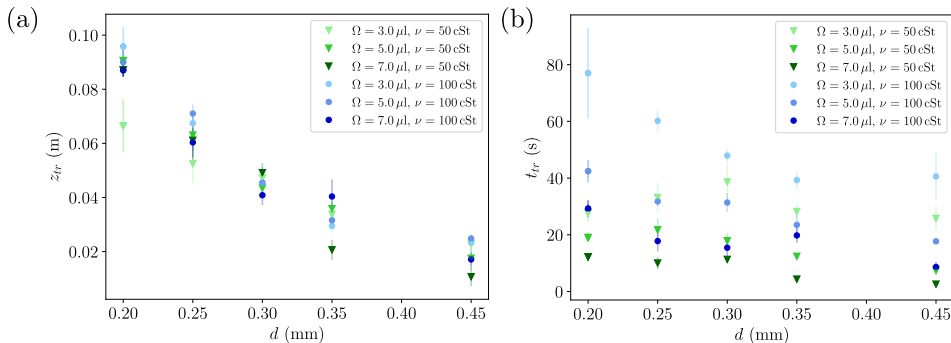


Figure 3.5: (a) Position of the transition z_{tr} as a function of the fiber diameter d and for several droplet volumes and liquid viscosities. The transition position corresponds to the location along the fiber where the droplet shifts from the growth phase to the decline phase. (b) Transition time t_{tr} as a function of the fiber diameter. The transition time is the duration from the droplet appearance to the phase change in its dynamic.

For $z < z_{tr}$, the droplet is in the growth phase. Eq. (3.11) is fitted on the trajectories with \bar{e}_0 as the fitting parameter, which represents the mean thickness of the liquid film left by generation 0. The order of magnitude of this mean thickness is confirmed a posteriori by calculating the ratio $\bar{e}_0/e_{0,i}$, where $e_{0,i}$ is the initial thickness of the liquid film, which can be determined using Eq. (3.3) and the experimentally estimated initial speed of the generation 0 droplet, \dot{z}_0 . This ratio is plotted in Fig. 3.6 as a function of the experimental parameters. Despite the large error bars, the mean thickness is systematically smaller than the initial maximum film thickness, which confirms the expected decrease in liquid film thickness along the fiber. The important error bars come from the fluctuations in the fitting parameter \bar{e}_0 as well as variations in the experimental initial conditions.

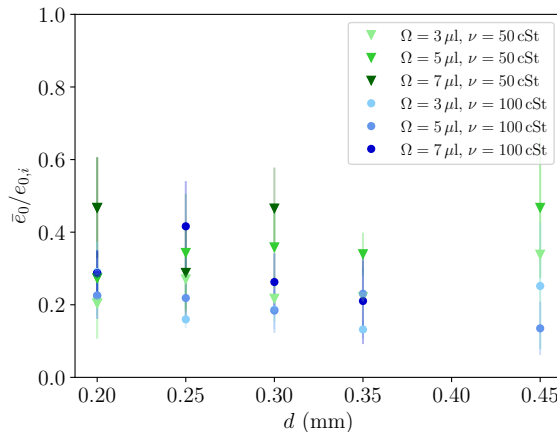


Figure 3.6: Ratio of film thickness $\bar{e}_0/e_{0,i}$ as a function of the fiber diameter d , and for different volumes Ω and fluid viscosities ν . The numerator, \bar{e}_0 , is a fitting parameter from Eqs. (3.11) and (3.12), it represents the mean thickness of the liquid film left by generation 0, which is used by generation 1 for growth. The denominator, $e_{0,i}$, is the initial thickness of the liquid film where generation 0 is deposited on the fiber. The fitted mean thickness is slightly less than half the initial maximum film thickness, a realistic estimate considering the non-uniformity of the liquid film, which decreases along the fiber.

For $z > z_{tr}$, the droplet is in the decline phase. This phase is described by Eq. (3.15), where the coefficient c_{wet}/ξ_{wet} is used as a fitting parameter. The resulting values are plotted in Fig. 3.7 as a function of the fiber diameter and for several volumes and viscosities. The fitting parameter is independent of both the volume and the diameter, and it slightly depends on the viscosity. The mean value is $c_{wet}/\xi_{wet} = 0.004$ for $\nu = 50$ cSt and $c_{wet}/\xi_{wet} = 0.005$ for $\nu = 100$ cSt. The dissipative parameter ξ can be approached using Eqs. (3.7) and (3.8). In the wet case, the values of a_f and a_r are different from those in the dry case. In front of the droplet, there is a liquid film with a characteristic length of $a_f \approx 10^{-5}$ m. At the rear, the droplet leaves a thinner film, one states $a_r \approx 10^{-6}$ m. Considering a droplet length $L \approx 10^{-3}$ m, we obtain $\Gamma = 10.1$ and $\xi_{wet} = 95$. As expected, the dissipative coefficient is smaller in the wet case than in the dry case. The literature estimates the logarithmic factor Γ to be around 5 for a wet surface [42], and we indeed find a close to five value, which validates the model. The value of c_{wet} can be found, we obtain $c_{wet} = 0.39$ for $\nu = 50$ cSt, and $c_{wet} = 0.48$ for $\nu = 100$ cSt. The obtained values of ξ_{wet} and c_{wet} are summarized in Table 3.1. Due to the different dynamic of generation 1 compared to generation 0, with smaller coefficients, all generations eventually converge, as shown in Fig. 3.1 (b) and Fig. 3.3.

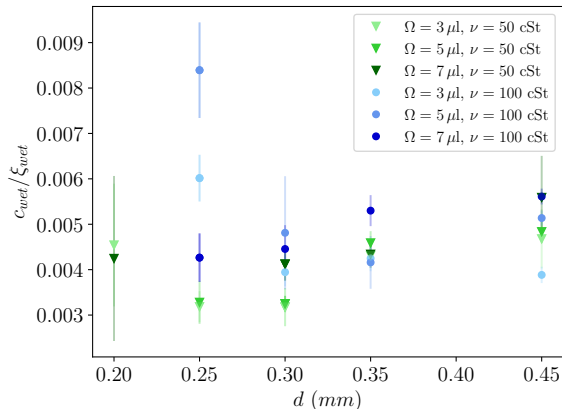


Figure 3.7: Fitted prefactor c_{wet}/ξ_{wet} from Eqs. (3.15) and (3.16) as a function of the fiber diameter d , for different volumes Ω and fluid viscosities ν . This prefactor is independent of both the droplet volume and the fiber diameter. However, the prefactor slightly increases with the viscosity.

3.4.3 Granddaughter droplets

We have described the dynamics of the mother and the daughter droplets (generations 0 and 1). The daughter droplet may also initiate the formation of a new generation at the initial deposition location. In Fig. 3.3, the position over time of generation 2 is presented. The dynamic of generation 2 is similar to generation 1 and the models can also be adapted on the data. We anticipate that all subsequent generations will follow the same trend, with the growth phase becoming broader for higher generations.

In this section, we propose a theoretical method to predict the number of droplet generations. By analyzing the initial conditions at the first droplet deposition, it is possible to predict the number of droplet generations that will be created at this specific position. The two key physical parameters required for this prediction are the diameter of the fiber and the volume of the generation 0 droplet. The initial liquid film thickness $e_{0,i}$ left by the mother droplet (generation 0) near the release point is given by Eq. (3.3) with $\dot{z}_{0,i}$ the initial speed of the generation 0 droplet. The subscript i indicates the initial condition. The liquid film then destabilizes into droplets following the Rayleigh-Plateau wavelength

$$\lambda = \pi\sqrt{2}d. \quad (3.17)$$

Considering the initial liquid film thickness $e_{0,i}$, the volume of the first daughter droplet (generation 1) can be approximated by

$$\Omega_{1,i} = \pi^2\sqrt{2}d \left(\left(\frac{d}{2} + e_{0,i} \right)^2 - \left(\frac{d}{2} \right)^2 \right). \quad (3.18)$$

This daughter descends with an initial speed $\dot{z}_{1,i}$ that depends on $\Omega_{1,i}$, and it leaves a liquid film behind with a thickness $e_{1,i}$ given by Eq. (3.3) with $\dot{z}_{1,i} =$

$g\Omega_{1,i}/\xi_{wet}\nu d$. This process can continue, generation 1 droplet may initiate the formation of a subsequent generation (generation 2), and so on. However, the Rayleigh-Plateau instability ceases when the film thickness e becomes less than or equal to a critical cutoff value e_c given by

$$e_c = c_c \frac{d^3}{l_c^2} \quad (3.19)$$

where $c_c = 0.175$ and where l_c is the capillary length, $l_c = \sqrt{\gamma/\rho g}$ [83]. This implies that the last generation will leave a liquid film thickness that is smaller than or equal to this cutoff value. Using this information, we can establish an iterative relationship to calculate the number of generations initiated by the mother droplet. With k as the iterative parameter, we continue the iterations until $e_{k,i} = e_c$. The iterated system of equations is

$$\begin{cases} e_{k,i} = cd \left(\frac{\nu\rho}{\gamma} \dot{z}_{k,i} \right)^{2/3} \\ \Omega_{k+1,i} = \pi^2 \sqrt{2} d \left(\left(\frac{d}{2} + e_{k,i} \right)^2 - \left(\frac{d}{2} \right)^2 \right) \\ \dot{z}_{k+1,i} = \frac{g}{\nu d \xi} \Omega_{k+1,i} \end{cases} \quad (3.20)$$

For $k = 0$, it refers to the mother droplet, which travels down along a dry fiber. For this case, we use the initial speed given by $\dot{z}_{0,i} = g\Omega_{0,i}/\xi_{dry}\nu d$. For $k > 0$, it refers to the k^{th} daughter droplet, which descends along a wet fiber. Here, the initial speed is given by $\dot{z}_{k,i} = g\Omega_{k,i}/\xi_{wet}\nu d$. In sections 3.4.1 and 3.4.2, we determined the values of ξ_{dry} , c_{dry} , ξ_{wet} and c_{wet} as summarized in Table 3.1. The iteration process with parameter k provides the number of generations that a mother droplet will create at the initial position.

Figure 3.8 shows the number of generations (indicated by a color scale) in a double logarithmic plot, with the fiber diameter d on the x-axis and the droplet volume Ω on the y-axis. The graph in Fig. 3.8 (a) corresponds to a viscosity of $\nu = 50$ cSt, and the graph in Fig. 3.8 (b) is for a viscosity $\nu = 100$ cSt. Black dots represent experimentally tested parameters. The number of generations increases with a larger initial droplet volume and a thinner fiber diameter. This dependence on the fiber diameter seems counter-intuitive since a thinner fiber implies a thinner film thickness, leading one to expect fewer generations. However, this is when not considering the cutoff thickness e_c , which decreases with the diameter raised to the power of three, thereby allowing for more droplet generations before achieving film stability. It is important to note that the system of equations (3.20) is independent of the viscosity because ν can be simplified when the speed is substituted into the equation of the film thickness. The differences between the graphs for $\nu = 50$ cSt and $\nu = 100$ cSt are due to the value of c_{dry} and c_{wet} that vary with the viscosity, indicating a missing scaling factor in the models. These varying values of c_{dry} and c_{wet} influence the region around the transition between k and $k + 1$ generation.

Experimentally, it is challenging to record the exact number of generation droplets at the deposition point. The droplet is released using a syringe, but since it is manually handled, slight variations can occur when transferring the droplet onto the

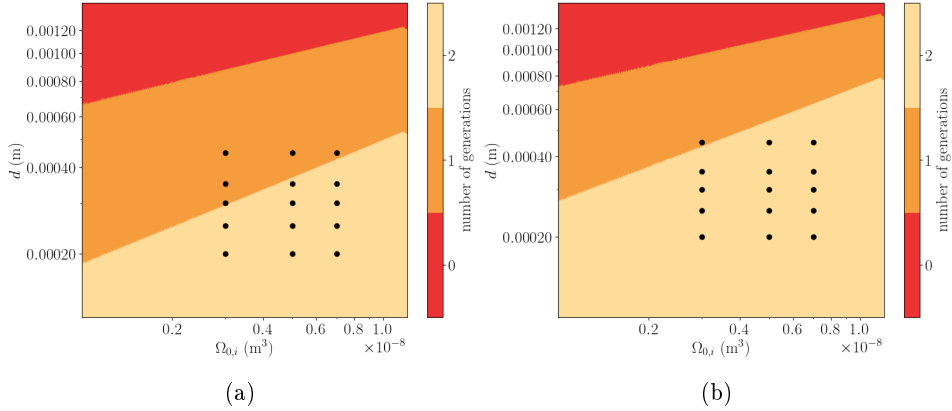


Figure 3.8: Number of generations in a double logarithmic graph of the diameter fiber d as a function of the initial mother droplet volume $\Omega_{0,i}$, for a fixed viscosity (a) $\nu = 50$ cSt and (b) $\nu = 100$ cSt. The different colors represent different generations. The black dots indicate the parameters tested experimentally. The number of generations is calculated by iterations of the system of equations (3.20) with a cutoff condition given by Eq. (3.19). The number of generations created at the initial deposition point increases with the droplet volume and thinner fiber diameters.

fiber. As a result, the liquid film at that position is influenced not only by the sliding of the initial droplet but also by the contact with the syringe or by the droplet pinching. Additionally, an unstable clamshell shape may initially appear, before transitioning into the stable barrel shape. Although experiments with observable clamshell shapes were excluded, this shape can still briefly appear within the first millimeter of descent. Another limitation is the small size of the subsequent generation droplets at the release point, making them difficult to record accurately. It is also problematic to account for droplets that form slightly further down the fiber, where the film is thicker due to the daughter droplet's growth phase. It is difficult to ensure that these droplets originate from the initial deposition point. Finally, thinner liquid films require a longer time for destabilization to occur, sometimes taking several hours. Due to these reasons, we are unable to provide experimental evidence of the precise number of generations formed. However, in all our experiments, we have recorded at least one generation. Furthermore, other droplets may appear at different positions, namely where the daughter droplet speed is maximal (between the growth and decline phases) and where mother and daughter droplets merge. These other generations are more complex and difficult to predict.

3.5 Conclusion

In this chapter, we study the motion of a droplet along a vertical fiber and the residual liquid film that coats the fiber as the droplet descends. The speed of the droplet influences the thickness of the liquid film it leaves behind; the faster the droplet, the thicker the resulting film, as theoretically analyzed for a plane substrate by Landau, Levich and Derjaguin [150] and for a cylindrical fiber by Qu  r   [81].

Because of this behavior, the initial droplet, which slows down as it descends, leaves a non-uniform liquid coating, with the thickest film near the initial release point. The coating film is observed to destabilize under the Rayleigh-Plateau instability, forming small droplets. The droplet that forms the fastest originates from the thickest part of the liquid film, typically at the release point of the initial droplet. This newly formed droplet grows by accumulating liquid from the film ahead of it as it slides down. The initial droplet, which creates the liquid film, is referred to as generation 0, while the droplet resulting from the liquid destabilization is termed generation 1. Initially, the generation 1 droplet accelerates in a phase termed growth phase. After reaching a given position, the liquid input from the front becomes negligible compared to the volume lost at the rear of the droplet, leading to a deceleration phase named the decline phase. This phase mirrors the dynamics of the initial generation 0 droplet. The model proposed by Gilet *et al.* [98] is used to describe the motion of the initial generation 0 droplet. Then, two models are provided to describe both the growth and decline phases observed in the generation 1 droplet trajectory. The dynamics of generation 0 and 1 are distinct, with generation 0 sliding on a dry fiber and generation 1 descending on a wet fiber. This difference leads to the merging of both generations after traveling a certain distance. Finally, generation 1 also leaves behind a liquid film, which may destabilize and form a new generation, called generation 2, and so on. We provide a theoretical estimation of the number of generations created at the release point of the initial droplet. However, with our current experimental setup, the analysis of the generation 2 droplet represents the limit of our observations.

This study contributes to the extensive literature on droplet behavior on fibers. It serves as an initial step towards understanding the predator-prey dynamics of self-sustaining droplets on fibers and opens up several avenues for further research. For instance, what occurs after the merging of the mother and daughter droplets? The "re-fed" mother droplet may initiate a new cycle, and analyzing the long-term behavior, including potential oscillations and increases in the period, could provide interesting insights. Such studies have potential applications in liquid coatings on fibers, where the formation of new generations needs to be controlled or avoided, as well as in fiber-based microfluidic devices, where this phenomenon must be considered.



4

Droplets on twisted cylindrical fibers

In this chapter, we investigate the impact of helical structures on the motion of asymmetrical droplets along vertical twisted fibers. The droplet adopts a helical motion around the bundle, driven by gravity. This complex motion can be manipulated by varying the twist turns of the fibers. When the droplet size is smaller than the characteristic length of the helix (pitch), the droplet adopts a predominant helical motion correlated with the groove of the twisted fibers. When the droplet size exceeds the pitch length, a mixed motion of vertical sliding and helical movement emerges. A model describes rotational and linear speeds as a function of the fiber twist turns number.

Partially under review as

J. Van Hulle, C. Delforge, M. Leonard, E. Follet, and N. Vandewalle, *Droplet helical motion on twisted fibers*, under review.

4.1 Introduction

Our focus lies on investigating the behavior of droplets traveling down two twisted fibers. The torsion of a bundle of two fibers creates a helical structure with a convex groove along the vertical bundle. We thereby create a system with a macrostructure, the vertical fibers, to guide vertically the droplet along with a microstructure, the helical convex groove. We aim to study the influence of this substructure on the motion of asymmetrical-shaped droplets, commonly referred to as clamshell shape, illustrated in Fig. 4.1.

Our investigation intersects with the recent research conducted by Kern and Carlson [100], which similarly examines the behavior of droplets along two twisted fibers. Their findings reveal distinct droplet trajectories, unveiling significant implications for droplet control and collection applications. It is important to note that our study operates within different experimental conditions. Furthermore, our contribution complements their work by delving deeper into the nuanced dynamics of these particular droplet trajectories. The differences and similarities are explained and highlighted throughout the chapter.

4.2 Experimental section

We use nylon fibers (fishing thread) with a fixed diameter, $d = 0.25$ mm. To achieve the desired stretching and twisting of the fibers, a single fiber is threaded through a buckle and fixed at the top on a manual rotation stage. By rotating the screw, both parts of the bundle can be twisted effectively. This helical structure is classified as a twisted double helix [151, 152]. The vertical length of the bundle is fixed at $L = 40$ cm. Each rotation of the screw corresponds to one twist turn of the fibers, denoted as n . A schematic representation of all defined lengths is presented in Fig. 4.2. The number of twists is given by

$$n = \frac{L}{2\pi b} \quad (4.1)$$

where $2\pi b$ is the pitch of the helical pattern, with b the reduced helix pitch. Note that twisting of the fibers creates a helical convex groove along the entire bundle. We conducted experiments with up to $n = 200$ twists. As the number of twists increases, so does the tension in the fibers, creating a highly compact structure. However, at higher twist counts, there is a risk of fiber deformation, which can result in non-uniform bundles, or in fiber breaking.

When a droplet adheres to a vertical fiber, it can adopt two distinct configurations: a barrel shape, where the droplet symmetrically engulfs the fiber, or a clamshell shape, where the droplet rests on one side of the fiber, creating an asymmetrical shape [73, 74]. Previous work by Gabbard *et al.* showed that a liquid film descending along a vertical fiber may undergo a destabilization process, resulting in a train of beads exhibiting either a symmetrical (barrel shape) or an asymmetrical morphology (clamshell shape) [92]. The occurrence of these configurations depends on factors such as fiber diameter and droplet surface tension. Specifically, the study

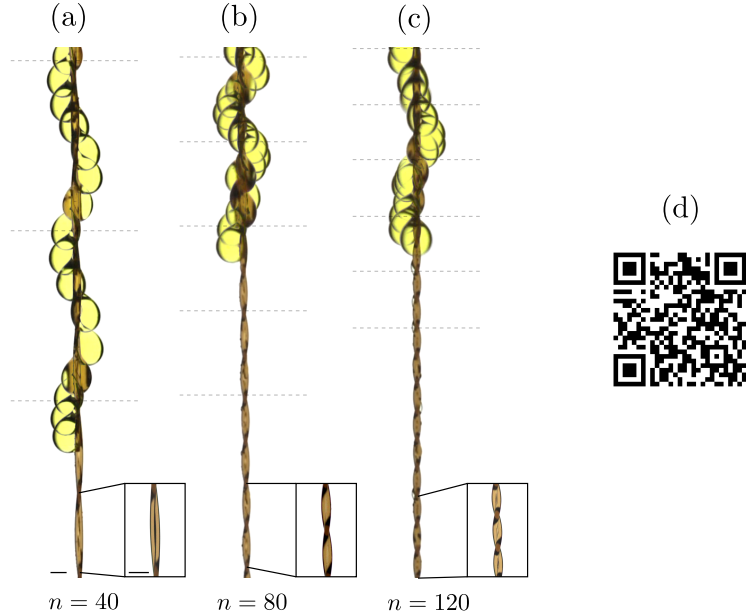


Figure 4.1: Superposition of successive pictures of an asymmetrically shaped droplet traveling down on twisted fibers with a helical motion. From left to right, the number of fiber twists increases, $n = 40, 80, 120$. The dashed horizontal lines represent the fiber pitch. For small n , the droplet follows exactly the substructure, displaying a helical motion, see (a). However, at a larger number of twist values, the droplet exhibits reduced adherence to the tight substructure, resulting in an additional vertical motion, see (b) and (c). The motion is a mix of translations and rotations but the helical motion is no longer correlated with the helical groove of the twisted fibers. The time interval between consecutive pictures is constant at $\Delta t = 0.2$ s. The volume of the droplet is $5 \mu\text{l}$ and the diameter of one fiber is 0.25 mm. The scale bars on picture (a) correspond to 1 mm. (d) QR code to access to the three experimental videos.

showed that the asymmetric configuration consistently arises for surface tensions exceeding 50 mN/m (see Fig. 1.14). The liquid we choose to use is glycerol with a surface tension of $\gamma \approx 55$ mN/m. The clamshell shape is therefore the more stable droplet configuration. The density of glycerol is $\rho = 1190$ kg/m³. We have noticed an important sensibility of the glycerol with temperature. As reported in the literature, the viscosity can decrease by half with an increase of 10°C [153]. Unfortunately, our lab equipment does not allow for precise control of the ambient lab temperature. Furthermore, glycerol manipulations are also suspected to warm the solution. Nonetheless, we measured a dynamic viscosity of $\eta \approx 1.2$ Pa.s at around 18°C , and $\eta \approx 0.8$ Pa.s at around 25°C . The difference factor is about 1.5 . The volume of the droplet is fixed at $\Omega = 5 \mu\text{l}$. The droplet is gently deposited on the bundle thanks to an electronic pipette (Eppendorf Xplorer plus). Before each experiment, the bundle is prewetted with several droplets to coat the grooves. For the initialization, at small twist number, 10 droplets are deposited to ensure complete prewetting of the fibers. This prewetting procedure ensures the studied

droplets keep a conserved volume. Subsequently, 5 droplets are measured. As the twist turn is increased, 2 prewetting droplets are deposited before the measurement of the subsequent 5 droplets. The contact length of the glycerol droplet on the fibers is constant and is measured, $l = 2.64$ mm. One can also approximate this length with the diameter of a spherical droplet, we have $l \sim 2(3\Omega/4\pi)^{1/3} = 2.1$ mm. The length between the center of the bundle of fibers and the center of the droplet is labeled a and is measured, $a = 0.76$ mm. This length is measured to be constant in all our experiments, the capillary force F_γ that acts at the surface of the droplet overcomes eventual deformations in the droplet shape due to centrifugal forces F_{cf} , the ratio of both forces is estimated $F_{cf}/F_\gamma \sim \rho\Omega\dot{\phi}^2 a/4\pi\gamma\Omega^{2/3} \approx 0.6$.

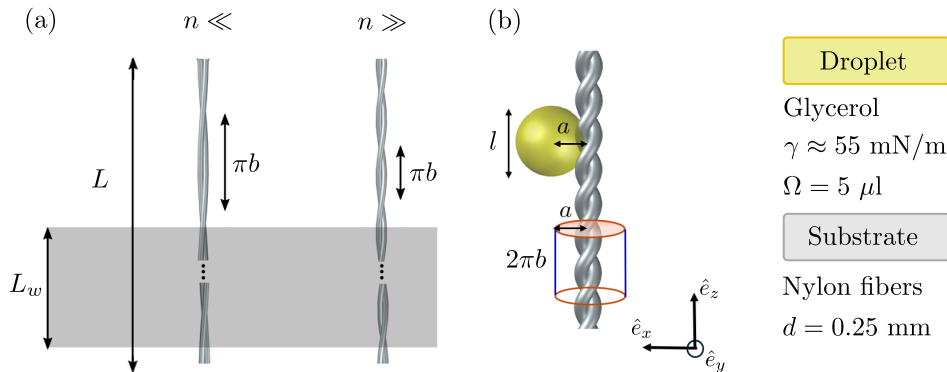


Figure 4.2: (a) Sketch of the twisted fibers. We define several lengths, L is the total bundle length, L_w is the portion of the twisted fibers captured by the camera. An increase in the number of turns n leads to a reduction in the half-pitch πb of the helical pattern. (b) Sketch of a spherical droplet on twisted fibers. The distance between the droplet center and the bundle center is labeled a . The length of the droplet is noted l . When the droplet performs a helical motion around the bundle axis with a $2\pi b$ pitch length, the droplet center describes a helix with a radius a which is comprised in a cylinder of radius a and height $2\pi b$. The motion is recorded with a camera placed in front of the bundle of fibers. The volume of the droplet is $\Omega = 5 \mu\text{l}$ and the diameter of one fiber is $d = 0.25$ mm.

In front of the fibers, a CCD camera (Coupled-Charge Device) is positioned to record the droplet motion. The camera captures a portion of the bundle $L_w = 8$ cm. This field of view is 15 cm under the release point of the droplet. A white lighting source is placed behind the fibers to ensure a good contrast of the droplet, and the glycerol is slightly dyed with yellow food coloring. An original Python code is employed to track the linearly increasing position of the droplet over time and to extract the slope to study the linear speed \dot{z} . Additionally, as the droplet is traveling around the bundle, one can also count the number of turns of the droplet. The number of turns made by the droplet is denoted τ_w . Consequently, one extracts the angular speed of the droplet $\dot{\phi}$.

To reveal key physical parameters, several nondimensional quantities are calculated. The Bond number defined as $\text{Bo} = \rho g \Omega / \gamma l$, compares gravitational and capillary effects. In our experiment, we have a Bo value of around 0.5, indicating

that the droplet dynamic is led by both gravitational and capillary effects, such conditions are similar to [147]. The Capillary number estimates viscous effects to surface tension ones, $Ca = \dot{z}\nu\rho/\gamma$. One obtains values in the range 0.1 to 0.5 with the typical speed values \dot{z} in our experiments. Surface tension overcomes viscous dissipation, allowing the descent of droplets along the fibers. The Weber number compares inertial and surface tension effects, $We = \rho\dot{z}^2l/\gamma$, yielding a We number smaller than 0.03, signifying a negligible role of inertia in the present study.

In this experimental setup lies two significant differences with the experiment conducted by Kern and Carlson [100]: the choice of liquid and the prewetting of the fibers. Their research centered on silicone oil droplets, a low surface tension liquid ($\gamma \approx 20$ mN/m), descending along dry twisted fibers. In our experiment, prewetting the fibers not only conserves droplet volume but also improves drainage efficiency. These divergent experimental approaches lead to complementary investigations, that expand the understanding of droplet dynamics on twisted fibers.

4.3 Results

The descending motion of the asymmetrical droplet is significantly influenced by the substructure created by the twist, as shown in Fig. 4.1. Indeed, the droplet exhibits a helicoidal motion along the twisted fibers. We observe that when the twist turns, denoted n , is small, the droplet follows exactly the twist of the fibers (Fig. 4.1 (a)). More precisely, one observes the droplet to follow the convex groove. This motion is labeled groove flow by [100]. However, as the number of twist turns increases, the droplet exhibits a combination of helical and vertical motions, as depicted in Fig. 4.1 (c), labeled as skipping flow [100]. Notably, the distance for one complete turn of the droplet is not correlated with the helical pitch of the twisted fibers. In our experiments, we discern instances where the droplet alternates between rotational and translation motion along several fiber pitches. In Fig. 4.1 (c), one shows that, at the end of the superposition, the droplet undergoes a vertical descent. The experimental videos are available thanks to the QR code present in Fig. 4.1 (d).

To describe this transition between both dynamical regimes, we measure the number of turns made by the droplet, τ_w . The count is done along the length L_w captured by the camera. We subsequently normalize it to the total length, resulting in

$$\tau = \left(\frac{L}{L_w} \right) \tau_w \quad (4.2)$$

In Fig. 4.3, we plot τ as a function of the number of twist turns n . For small values of n , the rotation of the droplet increases linearly with n , this is regime I (groove flow). As n surpasses approximately 80, marking the transition to a second regime, regime II (skipping flow), the number of turns made by the droplet falls to a smaller value that decreases with n .

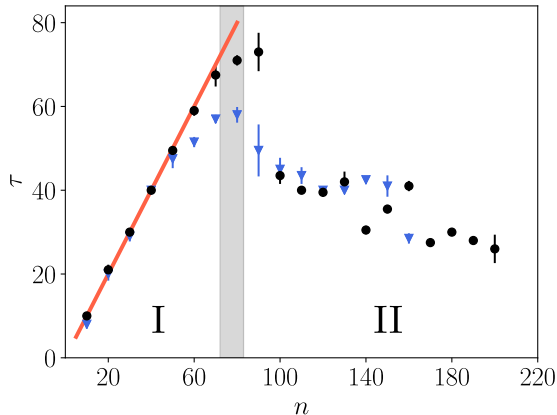


Figure 4.3: Number of droplet turns τ as function of fibers twist turns n . Data with black circles (\bullet) are for a low viscosity, around 0.8 Pa.s, and data with blue triangles (\blacktriangledown) are for a higher viscosity, around 1.2 Pa.s. One observes two distinct regimes. In regime I, for $n < 76$, the droplet follows the helical pattern. The number of turns made by the droplet is directly correlated with the fiber twists. The red line is a line of slope 1, i.e. $\tau = n$. In regime II, $n > 76$, the droplet is not following the substructure anymore. The number of turns made by the droplet decreases with n . The grey region depicts the transition between both regimes.

We assume that the transition to regime II is linked with the portion of the fiber that the droplet covers. Indeed, as can be seen in Fig. 4.4, for small values of n , the droplet length l is smaller than the half-pitch of the helical pattern πb (Fig. 4.4 (a)). On the other hand, for larger n values, the droplet spans several pitches, $l > \pi b$ (Fig. 4.4 (c)). When the length of the droplet equals the half-pitch, a transition occurs (Fig. 4.4 (b)). To quantitatively describe this transition, one introduces dimensionless parameter α , which is the ratio between the length of the droplet and the half-pitch [100],

$$\alpha = \frac{l}{\pi b} = \frac{2nl}{L}. \quad (4.3)$$

At the transition, we assume that $\alpha = 1$. We can thus theoretically approximate the number of twists needed to induce the transition $n_{tr} = 76$. This transition value is well estimated, as can be observed in Fig. 4.3. The theoretical transition is described in each plot with a vertical grey range. The width of this range is calculated by considering the error made on the droplet length l , we have $l = 2.64 \pm 0.16$ mm.

One can examine the droplet dynamics in both regimes. Note that both the angular speed and the vertical speed are constant for a given value of twists n thanks to the prewetting of the bundle. First, in Fig. 4.5 (a), we plot the angular speed $\dot{\phi}$ of the droplet as a function of α , for two different viscosities of the same mixture at different temperatures. In regime I, the angular speed increases with the twist turns, while in regime II, it decreases. This trend is also observed in [100] for the

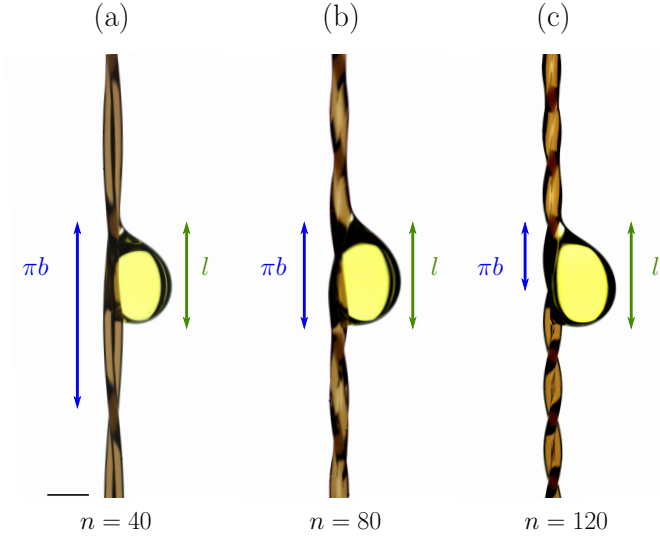


Figure 4.4: Pictures of a droplet on several twisted fibers. From left to right, the number of fiber twists increases, $n = 40, 80, 120$. This emphasizes the covered length of the droplet l on the twisted fibers (green), a key parameter to distinguish the motions adopted by the droplet. The half-pitch of the helical pattern created by the twisted fibers is depicted in blue. (a) The droplet's length is shorter than half the pitch. Under such conditions, the droplet exhibits a purely helical motion. (b) The droplet's length is the same as the half-pitch. (c) The droplet's length is longer than the half-pitch, which induces a combined behavior of helical motion and vertical sliding. The volume of the droplet is $5 \mu\text{l}$ and the diameter of the fiber is 0.25 mm . The scale bar corresponds to 1 mm .

groove and skipping flows. Next, in Fig. 4.5 (b), we plot the linear speed \dot{z} as a function of the dimensionless parameter α (see Eq. (4.3)). Interestingly, in regime I ($\alpha < 1$), we observe an important decrease in the linear speed with α , while in regime II ($\alpha > 1$), it decreases more slowly with α . Surprisingly, this influence of the twists on the linear speed is not observed when the fibers are not prewetted [100]. In both Fig. 4.5 (a) and (b), one notices that a change in viscosity does not affect the trend of the data, a decrease in the viscosity only results in an increase of the angular and vertical speeds. In the following section, we describe the observed trends thanks to one model for each regime.

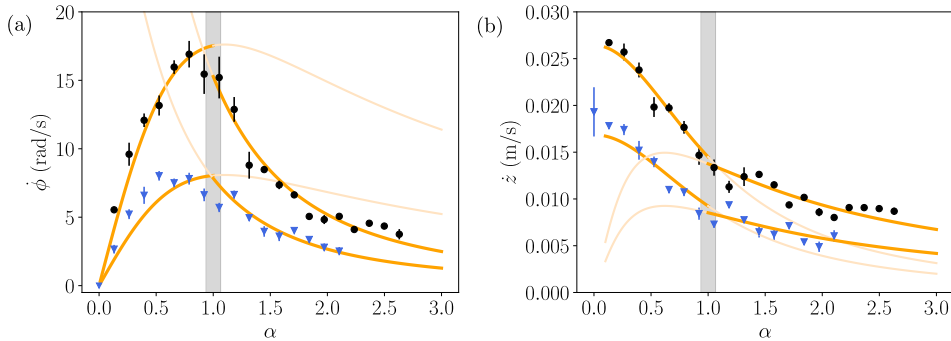


Figure 4.5: (a) Angular speed $\dot{\phi}$ as a function of α . In regime I, $\alpha < 1$, the angular speed increases with α . In regime II, $\alpha > 1$, it is slightly decreasing. The colored curves are fit of Eq. (4.8) and Eq. (4.10) on the respective regime. (b) Linear speed \dot{z} as a function of α . In regime I, $\alpha < 1$, the linear speed decreases with α . In regime II, $\alpha > 1$, it decreases more gently. The orange curves are fit of Eq. (4.9) and Eq. (4.11). Data with black circles (\bullet) are for a low viscosity and data with blue triangles (\blacktriangledown) are for a higher viscosity. The grey region both in (a) and (b) depicts the transition between the two regimes.

4.4 Discussion

In the first instance, to differentiate the motions in both regimes, the ratio $\dot{z}/(b\dot{\phi})$ is plotted in Fig. 4.6 (a). The relation $\dot{z}/(b\dot{\phi}) = 1$ is characteristic of a helical motion. In the first regime, for $\alpha < 1$, this ratio is approximately 1, with a mean value of 0.9. This regime is dependent on the characteristic length of the helix, $2\pi b$. Interestingly, in the second regime, the relationship between vertical and angular speed is not correlated with the helix length. When the droplet size is larger than the half-pitch, it changes the characteristic length. In the second regime, the capillary length of the droplet l_c and the relative size of the droplet compared to the helix, α , are important parameters. This is depicted in Fig. 4.6 (b) where the ratio $\dot{z}/(\alpha l_c \dot{\phi})$ is plotted. It shows a constant value in the second regime, with a mean value of 0.4. The transition between regimes signifies a change in the dominant parameter, the first regime is governed by the helix pitch $2\pi b$ (Fig. 4.6 (a)), while the second regime is dominated by the capillary length and the relative size of the droplet compared to the half-pitch (Fig. 4.6 (b)). This transition marks a shift from a regime where the helical structure dictates the motion to one where capillary length controls the descent, combining helical motion with vertical sliding.

To describe the particular motion of the droplet, one can notice that the center of mass of the droplet follows a helical path inscribed on the surface of a cylinder. The height of the cylinder is $2\pi b$ and its radius is a , as illustrated in Fig. 4.2 (b). Two capillary forces act at both ends of the droplet. These capillary forces act as adhesive forces, promoting rotation around the bundle by creating a resultant force directed toward the cylinder's interior. To describe the helical motion of the center of mass, one can unroll the cylinder into a rectangular representation with

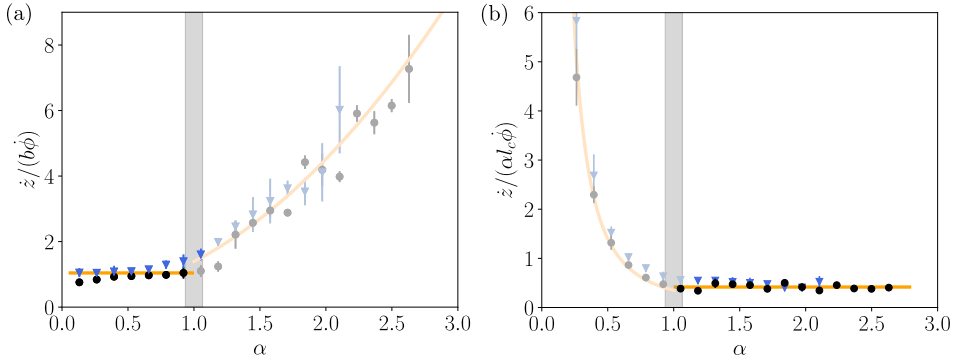


Figure 4.6: (a) Ratio $\dot{z}/(b\dot{\phi})$ as a function of α . For $\alpha < 1$, the ratio is constant, with a mean value close to one. The first regime is linked with the characteristic length of the helical groove of the bundle. For $\alpha > 1$, the vertical and the angular speeds relation is not defined by the helix pitch $2\pi b$, showing an increasing trend with α . (b) Ratio $\dot{z}/(\alpha c \dot{\phi})$ as a function of α . This ratio is constant in the second regime ($\alpha > 1$), with a mean value of 0.4. This is indicative that the capillary length times the droplet's relative size to the half-pitch is the relevant characteristic length in this regime. One observes no influence of the viscosity.

a length $2\pi a$, corresponding to the perimeter of the cylinder base, and a width $2\pi b$, corresponding to the pitch of the helix, as represented in Fig. 4.7. This representation also includes the grooves between the fibers, which are parallel to the diagonal of the rectangle. Two grooves are represented, the one in front of the bundle and the one at the rear. Depending on the relative size of the droplet compared to the half-pitch, the droplet may either sit on a single groove ($\alpha < 1$, see Fig. 4.7 (a)) or span on multiple grooves ($\alpha > 1$, see Fig. 4.7 (b)).

To model the behavior observed in the different regimes, we use a balanced force model. The droplet motion is driven by its weight, which is balanced by viscous dissipation. Inertia can be neglected due to the Weber number and the constant velocities observed during helical motion at fixed torsion. We therefore consider a balance between the dissipation force and the driving gravitational force along the fiber groove, as sketched in Fig. 4.7 (a) and (b). The dissipation force is given by

$$F_{\eta} = \xi \eta l v \quad (4.4)$$

with ξ a geometrical parameter and v the total speed of the droplet which is given by

$$v = \sqrt{\dot{z}^2 + (a\dot{\phi})^2}. \quad (4.5)$$

The gravitational component along the groove is given by

$$F_{g,h} = \rho g \Omega \sin(\theta), \quad (4.6)$$

where θ is the slope of the helix and is given by $\tan \theta = b/a$. This leads to

$$F_{g,h} = \rho g \Omega \frac{b}{\sqrt{b^2 + a^2}}. \quad (4.7)$$

Balancing both forces allows to describe the observed trend of \dot{z} and $\dot{\phi}$ as explained in the following sections.

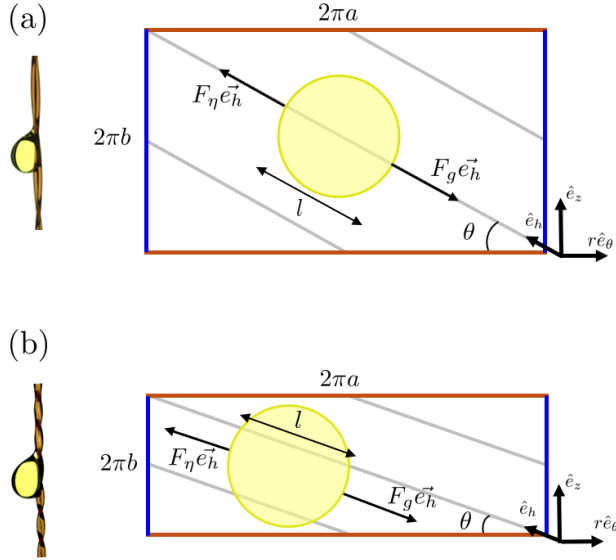


Figure 4.7: Representation of the unrolled cylinder on which the helical motion is inscribed. The length is given by the perimeter of the cylinder base, $2\pi a$, and the width by the pitch of the helix, $2\pi b$. The grooves of the fiber bundle are depicted as grey lines parallel to the diagonal of the rectangle. The slope of the helix is labeled θ . In regime I, where the droplet length l is smaller than the half-pitch πb , the droplet sits on one groove, as shown in (a). In regime II, the droplet spans several grooves, as shown in (b). In both cases, the motion is attributed to a balance between the driving gravitational force and the dissipating friction force.

4.4.1 Regime I

In this subsection, we model the droplet motion when it adheres to the spiral pattern of the twisted fibers. We assume the motion of the droplet to be a helix with (i) a reduced pitch b_{drop} equal to the reduced pitch of the twisted fibers, $b_{drop} = b$, and with (ii) a radius a given by the length between the center of the bundle of fibers and the center of the droplet. In the regime I, the relation between the vertical speed and the angular speed is given by $\dot{z} = b\dot{\phi}$ as shown in Fig. 4.6 (a). Injecting this relation into Eq. (4.5) and balancing the weight and the dissipation, leads to the expression of the angular speed,

$$\dot{\phi}_I = \frac{\rho g \Omega}{\xi_I \eta l} \frac{b}{b^2 + a^2}. \quad (4.8)$$

Then, one obtains the vertical speed,

$$\dot{z}_I = b\dot{\phi}_I = \frac{\rho g \Omega}{\xi_I \eta l} \frac{b^2}{b^2 + a^2}. \quad (4.9)$$

In these two relations, we have two unknown parameters ξ_I and ξ'_I for dissipation, that are used as fitting parameters. These two coefficients account for the different dissipation in angular motion and vertical motion.

4.4.2 Regime II

In this subsection, we describe the motion of a droplet in the second regime where an intermittent vertical sliding is observed. The droplet sometimes adheres to the helical fiber substructure and sometimes slides along the bundle. The ingredients are the same as before except for the relation between the vertical speed and the angular speed. As shown in Fig. 4.6 (b), one has the following relationship $\dot{z} = \alpha l_c \dot{\phi}$. We obtain the following expressions,

$$\dot{\phi}_{II} = \frac{\rho g \Omega}{\xi_{II} \eta l} \frac{b}{\sqrt{(\alpha l_c)^2 + a^2} \sqrt{b^2 + a^2}}, \quad (4.10)$$

and

$$\dot{z}_{II} = \alpha l_c \dot{\phi}_{II} = \frac{\rho g \Omega l_c}{\xi'_{II} \eta l} \frac{\alpha b}{\sqrt{(\alpha l_c)^2 + a^2} \sqrt{b^2 + a^2}}, \quad (4.11)$$

with ξ_{II} and ξ'_{II} two dissipation coefficients for the dissipation in the second regime.

4.4.3 Analysis

The previously described models can be adjusted on the experimental data for each regime. We divide the data into both regimes: regime I with $\alpha < 1$ and regime II with $\alpha > 1$, to fit the corresponding model on each regime. In Fig. 4.5 (a) and Fig. 4.5 (b), we plot the angular speed and the vertical speed as a function of α , with the orange lines representing the model fittings. The models depict well the observed behaviors. In the model, $\xi \eta$ and $\xi' \eta$ are the fitting parameters. As the temperature is not well controlled in our laboratory, we let the viscosity η remain as a free fitting parameter. We find that the fitting parameters are of the same order of magnitude across both regimes. The fitting parameters are given in Table 4.1. One notices that the fitting parameter is systematically larger for the higher viscosity. We also show the ratio of the fitting parameters, which highlights the influence of the viscosity variation. This ratio is approximately equal to the expected viscosity ratio, around 1.5, as described in section 4.2. Although the fitted values are similar, the difference can be attributed to a different dissipation between helical and vertical motions. Specifically, in regime II, the droplet slides along multiple pitches and grooves, which can result in a higher dissipative coefficient for the vertical motion. Indeed, it is known that horizontally oriented fibers intersecting the path of a vertically descending droplet have a significant influence on its behavior [80, 98]. The droplet may either continue its motion or stop, hung on the horizontal fiber. In our case, the droplet moves along a fiber with periodic bumps, due to the substructure, which may act as obstacles along the droplet's path, explaining the different dissipation in the angular and vertical motions in the second regime. Also, the lack of precise temperature control may affect the viscosity and, consequently, the fitting parameters.

	Low viscosity	High viscosity	Ratio
$\xi_I\eta$	0.83 Pa.s	1.8 Pa.s	2.2
$\xi_{II}\eta$	0.47 Pa.s	0.91 Pa.s	1.9
$\xi'_I\eta$	0.84 Pa.s	1.32 Pa.s	1.6
$\xi'_{II}\eta$	1.13 Pa.s	1.82 Pa.s	1.6

Table 4.1: Comparison of the obtained fitting parameters. The fitting values obtained for the angular speed in regimes I and II, $\xi_I\eta$ and $\xi_{II}\eta$ respectively, are compared with the ones for the vertical speed in regimes I and II, $\xi'_I\eta$ and $\xi'_{II}\eta$, respectively. It is observed that the values are systematically higher for the high viscosity fluid. The last column shows the ratio of the values for high viscosity to those of low viscosity. The ratio values are similar.

4.5 Application: Manipulation and fog collection

For further insights into the practical applications of twisted fibers, the recent paper by Kern and Carlson [100] provides interesting demonstrations of droplet manipulation and collection on twisted fibers. This section reviews their work.

Twisted fibers offer the opportunity to manipulate droplets with carefully designed fiber meshes. As discussed in section 1.4.6 of the State of the Art, droplets descending along fiber networks with horizontal fiber crossings, result in a reduction in the droplet speed and leave small liquid deposits at the intersections. This phenomenon occurs also with clamshell shape droplets and when using a bundle of two parallel fibers vertically instead of a single fiber, as illustrated in Fig. 4.8 (a) (left). To avoid the slowdown and liquid loss, twisted fibers can be employed as a solution. In this setup, two twisted fibers are placed vertically with a small number of twist turns, while the horizontal fiber alternates between being positioned in front of and behind the twisted fibers. Experimental images from [100], shown in Fig. 4.8 (a) (right), demonstrate that on such a network, a clamshell shape droplet can follow the helical twist (regime I) and avoid fiber crossings. Consequently, no liquid is left behind when the horizontal fiber is on the opposite side of the droplet path and the descent is faster.

Regarding fog collection, twisted fibers show interesting collection ability when placed in a fog chamber. Fig. 4.8 (a) (left) compares a single fiber with a twisted bundle with collected water droplets. On a single fiber, several droplets form and become pinned along the fiber. In contrast, on two twisted fibers, the absence of visible droplets suggests the existence of a liquid film within the helical groove. This enables an increased collection efficiency. The efficiency is quantified by the capture efficiency of each twisted bundle, $E_{\pi b}$ which is defined as the ratio between the amount of water collected and the amount of fog in the flow. The graph in

Fig. 4.8 (b) (right) shows the ratio of the measured deposition efficiency $E_{\pi b}$ to the theoretical one E_d (for a smooth fiber), $E_{\pi b}/E_d$, as a function of the twisting ratio, $d/\pi b$. For $d/\pi b = 0$, the fibers are parallel (πb tends to infinity), the efficiency ratio is larger than one, indicating enhanced efficiency compared to the theoretical prediction for a single fiber without grooves. As the number of fiber twists increases (i.e., decreasing half-pitch πb), the capture efficiency increases. Within a fog flow, the twisted fibers become wetted, which facilitates fog capture and liquid drainage through the wetted grooves.

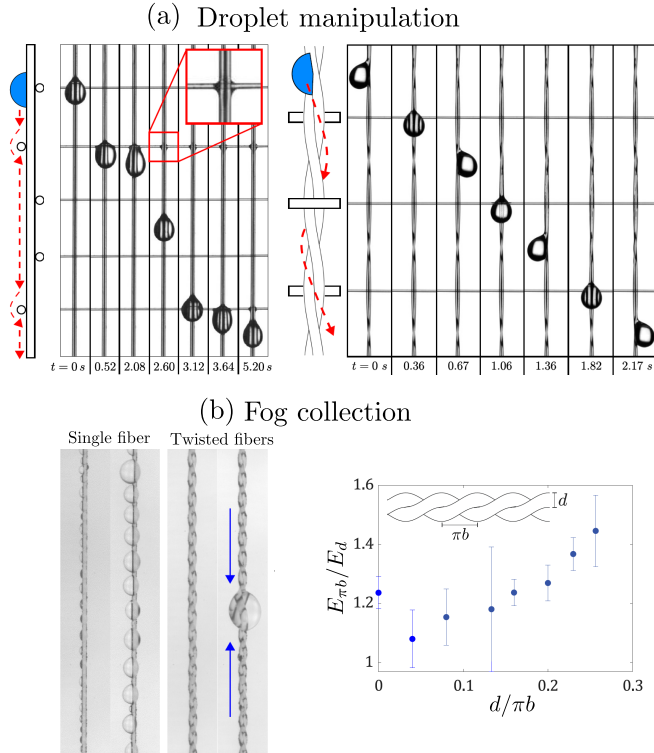
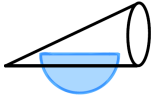


Figure 4.8: (a) Clamshell shape droplet descending along a fiber network composed of a bundle of two vertical fibers, with horizontal fibers alternately placed in front of or behind the bundle. The vertical fibers in the bundle are either parallel (left) or twisted (right). When the vertical fibers are parallel, the droplet slows down at fiber crossings and leaves a liquid residue at the crossing. When the vertical fibers are slightly twisted (regime I), the droplet follows the helical groove which prevents slowdown and liquid loss. (b) Twisted fibers demonstrate effective water collection from fog. While droplets tend to cling to a single fiber, no visible droplets appear on twisted fibers, suggesting the formation of a liquid film within the grooves. The graph on the right shows the ratio of the measured deposition efficiency $E_{\pi b}$ to the theoretical deposition efficiency for a single smooth fiber E_d as a function of the twisting ratio $d/\pi b$. When $d/\pi b = 0$, the fibers in the bundle are parallel. Increasing the twist of the fibers enhances the efficiency of fog collection. From [100].

4.6 Conclusion

In this chapter, we study the helicoidal and translational dynamics exhibited by a droplet traveling along vertical twisted fibers for two different viscosities. The droplet exhibits an asymmetric clamshell shape due to the high surface tension of glycerol. Twisting two cylindrical fibers creates a specific bundle with a helical convex shape groove. This substructure considerably influences the droplet's motion. Indeed, depending on the twist turns, the droplet is seen to adopt a predominantly helical trajectory or a predominantly vertical one. These reveal two regimes that depend on the relative dimensions of the droplet and of the helical pitch, as also observed in [100]. When the droplet size is smaller than the pitch, the droplet has a high tendency to adhere to the helical substructure. Conversely, when the droplet size surpasses the pitch length, then the droplet that spans on several grooves exhibits a mixture of motion composed of vertical sliding and helical motion. Furthermore, we show that increasing the viscosity decreases both speeds but does not affect their trends with the twist turns. We develop a model that describes the experimental data of the rotational speed and the linear speeds. In addition, we observe a larger dissipative coefficient for the vertical motion in the second regime explained by the fact that the droplet encounters several bumps due to the helical structure of the fibers.

This study shed light on the importance of substructures that can change the behavior of the droplet's motion. We achieve the rotation of the droplet along a vertical fiber, thereby opening avenues for three-dimensional manipulation of droplets. It enables the droplet to go from either the right-left or front-back side of the fiber. Additionally, this rotational motion affords the droplet an expanded interaction area with the surrounding gas phase, which holds promise for application in droplet-gas interaction [154, 155]. This experiment is also a creative adaptation of a bead moving along a helical wire, a usual problem taught in classical mechanics. Indeed, the soft matter bead leads to transitional behavior and unusual motions. Finally, this study has potential implications for enhancing droplet drainage of droplets along fibers. Specifically, we highlight that small torsions in a bundle of fibers induce larger vertical speeds than high twisted bundles. Draining efficiency is a key problem in water-harvesting structures, particularly in fiber-based configurations such as harps or nets [135, 125]. Twisted fibers hold promise for optimizing the performance of such structures in water collection applications. This study also opens potential avenues for future research on liquid retention on twisted fibers. Performing an experiment of a twisted bundle outward from a liquid bath could be interesting to investigate the thickness and the stability of the prewetting liquid inside the helical convex groove.



Droplets on a conical fiber

In this chapter, we focus on describing droplets moving on conical fibers. The experiment consists of a horizontal cone and a silicone oil droplet placed at its tip. We describe the motion of the droplet along the cone and consider the transition in the shape of the droplet. When the droplet is near the tip, its shape is a barrel while when the droplet encounters larger radii it has a clamshell shape. Depending on the droplet's shape, the dynamic differs. We also investigate the influence of the cone half-angle and the droplet volume on the dynamic.

Partially published as

J. Van Hulle, F. Weyer, S. Dorbolo, and N. Vandewalle, *Capillary transport from barrel to clamshell droplets on conical fibers*, Phys. Rev. Fluids **6**, 024501 (2021).

5.1 Motivations

Several works [99, 114, 112] have proposed that spine shapes could trigger the motion of droplets. Indeed, a droplet on a conical fiber is known to move toward large radii, as it can be seen in Fig. 5.1, due to the imbalance between surface tension forces acting on the droplet surface. This effect was first characterized by Lorenceau *et al.* [99], as described in the State of the Art, section 1.5.1. They studied this phenomenon for specific materials and scales, namely, microliter silicone oil droplets on pretwisted conical copper wires with a half-angle $\alpha \approx 0.38^\circ$ and a length $L = 3$ cm. Those cones were created by pulling a cylindrical copper wire out of an acid bath. Other studies used different ways to manufacture conical fibers like pulling glass [115, 118, 120, 156], using an electrochemical corrosion gradient [113] or even polishing brass [121].

According to the relative size of the fiber and of the droplet, the droplet on cylindrical and conical fibers can present two distinct geometries: barrel or clamshell [73]. A droplet with a barrel shape fully wraps the section of the fiber while a droplet in a clamshell shape covers only one side of the fiber, as explained in section 1.4.1. In all experimental studies listed above, the droplets adopt a barrel shape, except for two studies which focus on droplets showing a clamshell shape [121, 156]. The influence of gravity on the droplet shape is neglected in their models because its size is below the capillary length. Note also that all those previous studies used pretwisted conical fibers. A table comparing the experimental parameters used in this study to the recent publications is presented in Table 5.1 in order to position our work.

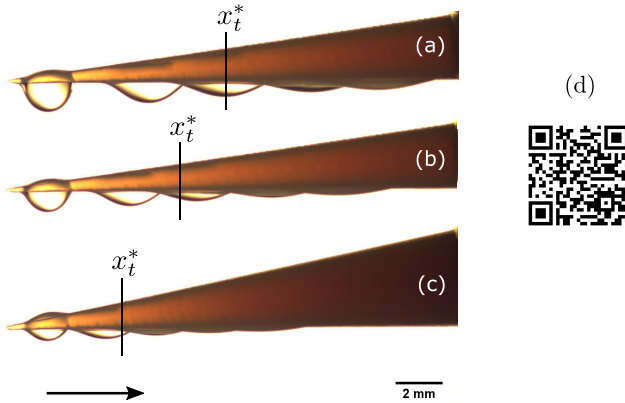


Figure 5.1: Superposition of successive pictures emphasizing the motion of a droplet on a 3D-printed conical structure. The motion is shown at time $t = 0$ s, 2 s, 7 s, 20 s and 45 s. (a) $\alpha = 4^\circ$, $\Omega = 4 \mu\text{l}$, (b) $\alpha = 4^\circ$, $\Omega = 2 \mu\text{l}$ and (c) $\alpha = 6^\circ$, $\Omega = 2 \mu\text{l}$. The vertical black line indicates the estimated position of transition x_t^* which is the distance after which the droplet should switch from the barrel shape to the clamshell shape. This value is calculated from Eq. (5.2). (d) QR code to access the three experimental videos.

		Half-angle α ($^\circ$)	Cone length L (cm)
Barrel	Lorceau [99]	0.38	3.0
	Li [115]	0.89	0.4
	Michielsen [120]	10.5, 14.2, 16	1.0
	Fournier [118]	≈ 0.05	≈ 0.5
Clam	Lv [156]	3.2	1.0
	McCarthy [121]	5, 10, 20, 45	1.5
Barrel & Clam	This chapter	3, 4, 5, 6, 7, 8, 9, 10	2.0

Table 5.1: Table comparing previous studies of droplets moving along conical fibers. This table shows the experimental parameters used, namely, half-angles α of the apex and the length L of the conical fiber. The studies are categorized by the shape adopted by the droplet on those fibers, either barrel or clamshell shape. This chapter is placed in another category as both barrel and clamshell shapes are experimentally observed on a single conical fiber.

The major motivation of this work is to achieve an extensive study on capillary transport of droplets lying on larger dry conical structures. Moreover, as can be seen in Table 5.1, we use conical fibers with a wide variety of large half-angles and with a relatively long length compared to other studies. We observe that such fibers allow droplet transportation. Fig. 5.1 shows a superposition of pictures emphasizing the motion of large droplets in three different cases that will be discussed in section 5.3. In all the situations shown in Fig. 5.1, the droplet spontaneously moves from the tip to the base of the cone. In addition to this directional motion, a shape transition of the droplet is observed during this motion. The droplet switches from the barrel shape to the clamshell shape. Previous experimental studies focused on either the barrel shape or the clamshell shape but none has experimentally observed this change of geometry (without any wetting gradient). We were able to witness this transition of shapes thanks to the properties of the cones we use (dry cones, long length, large half-angles). In this chapter, we perform an experimental study of this motion driven by capillarity, as well as by the geometry switch. Our results allow us to estimate the position of the geometrical transition and to propose two models for macroscopic capillary transport of both the barrel and the clamshell shape droplets on conical fibers.

5.2 Methods

In order to make an extensive experimental study, we 3D-printed several conical structures using Object Prime 30 from Stratasys, the same 3D printer as used in Chapter 2. This 3D-printing technology offers an easy and controllable way of manufacturing cones. On top of it, the flexibility of the 3D-printing technique offers the opportunity to explore various cone angles. We considered half-angles α from 3° to 10° . Those cones were slightly inclined for the experiment: the cone axis is tilted with the angle α in order to ensure that the lowest part of the cone was horizontal. Therefore, the droplet motion cannot be only attributed to gravity effects. A sketch of the experimental setup is shown in Fig. 5.2.

Prior to each experiment, we cleaned the cones with isopropanol and water and let them dry. The droplet was dropped off on the cone's tip thanks to a micropipette (Eppendorf Xplorer). We used silicone oil (Dow Corning), with a viscosity $\nu = 50$ cSt. The static contact angle between silicone oil and ABS is $\theta \approx 0^\circ$. Therefore, we were in the case of total wetting. We chose to focus on a range of droplet volumes Ω from $2 \mu\text{l}$ to $4 \mu\text{l}$. Higher volumes could not be tested because such larger droplets drop off the fiber (in particular near the tip).

Perpendicular to the cone's axis of symmetry, a CCD camera recorded the motion of the droplet (at 20 fps). A white background was lighted to achieve a good contrast. By image treatment, the left and right positions x_- and x_+ of the droplet from the apex were determined. The position of the droplet center is defined by $x = (x_+ + x_-)/2$, as shown in the inset of Fig. 5.3.

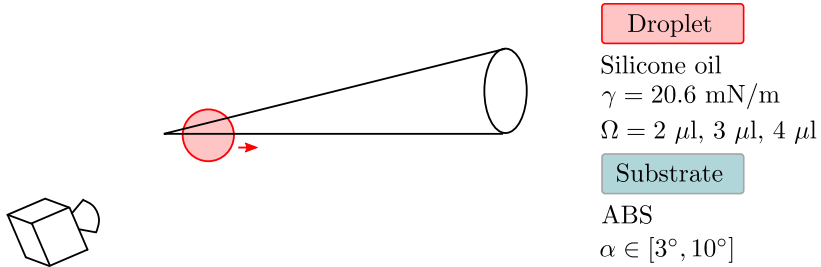


Figure 5.2: Sketch of the experimental setup. Cones are 3D printed and positioned with the lowest part horizontal. The half-angle of the cone α ranges from 3° to 10° . A droplet is deposited at the tip of the cone using a syringe and its motion towards the larger fiber radius is recorded with a camera in front of the cone axis. The tested droplet volumes are $\Omega = 2 \mu\text{l}$, $3 \mu\text{l}$ and $4 \mu\text{l}$.

5.3 Results

The typical evolution of the droplet position over time is shown in Fig. 5.3. This shows that the position x increases, at first rapidly and then more slowly. Moreover, we plot the position over time for different half-angles α and different volumes Ω in order to highlight the influence of both parameters on the droplet motion. For the same interval of time, the droplet with the largest volume, moving on the cone with the smallest half-angle, goes further than the other ones.

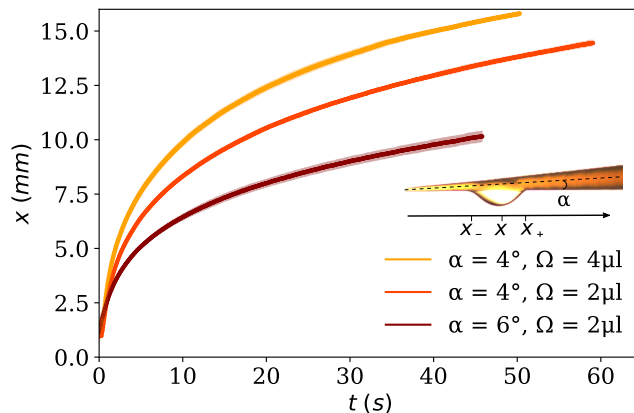


Figure 5.3: Position from the apex of the droplet center x along a cone as a function of time t . Different half-angles and volumes are shown : $\alpha = 4^\circ$, $\Omega = 4 \mu\text{l}$; $\alpha = 4^\circ$, $\Omega = 2 \mu\text{l}$ and $\alpha = 6^\circ$, $\Omega = 2 \mu\text{l}$. The error bars coming from repeated experiments for each data set are in light color. The inset defines the half-angle α of the cone as well as the position from the apex of the droplet center defined by $x = (x_+ + x_-)/2$.

In our experiments, the motion of the droplet is characterized by the capillary number $\text{Ca} = \dot{x}\nu\rho/\gamma \approx 2 \times 10^{-3}$, where \dot{x} is the droplet speed, γ is the surface tension and ρ is the density. This value indicates that the surface tension force

overcomes viscous one. The Weber number can also be calculated $We = \rho \dot{x}^2 L / \gamma \approx 7 \times 10^{-5}$, where L is the characteristic length of the system. Here, L is the typical diameter of a droplet : $L \approx 1.5 \times 10^{-3}$ m. It tells us that surface tension effects also dominate inertial forces. The Reynolds number, defined as $Re = \dot{x}L/\nu$, compares inertial forces to viscous forces. For our experiments, its value is $Re \approx 0.03$, therefore viscous forces are larger than inertial ones. The Bond number Bo is the ratio of gravitational forces to capillary forces, $Bo = \rho g L^2 / \gamma \approx 1.04$, where g is the gravitational acceleration. It reveals that gravity affects the barrel shape droplets.

To evidence the droplet motion, we compute the speed of the droplet \dot{x} as a function of the inverse of position $1/x$. This speed is obtained using a five-point derivative of the data $x(t)$ from Fig. 5.3. This is illustrated with a double logarithmic graph in Fig. 5.4 for the same cases as presented in Fig. 5.3. The speed decreases as the position on the fiber increases, i.e. as the inverse position decreases. The three curves clearly indicate that the motion is affected by the half-angle α and the volume Ω . Furthermore, it can be seen that as the half-angle increases, the speed decreases. Changing the volume reveals that the higher the volume is, the higher the speed is.

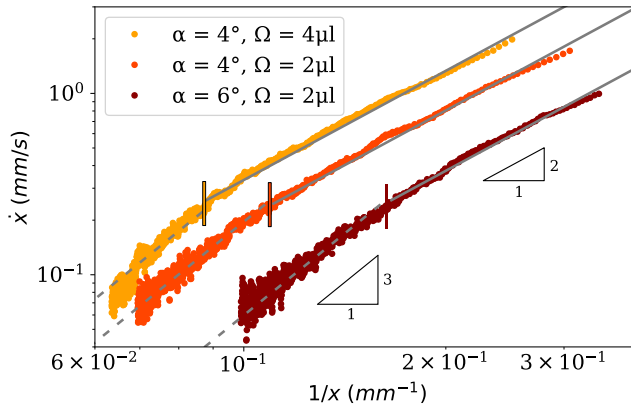


Figure 5.4: Double logarithmic graph of the speed \dot{x} of the droplet as a function of the inverse position $1/x$, for different half-angles and volumes : $\alpha = 4^\circ$, $\Omega = 4 \mu l$; $\alpha = 4^\circ$, $\Omega = 2 \mu l$ and $\alpha = 6^\circ$, $\Omega = 2 \mu l$. The short vertical colored lines are the inverse of the transition position $1/x_t^*$ (see Eq. (5.2)). The grey lines are fitting curves corresponding to the barrel shape model (see Eq. (5.11)), straight line, and to the clamshell model (see Eq. (5.12)), dashed line.

5.4 Discussion

In order to describe the dynamics of the droplet, we have to inspect the geometry of the system. Although both position and speed are smooth curves, the droplet is submitted to a major change of geometry, as it can be seen from Fig. 5.5. This image is obtained using ImageJ [157] and is the result of the difference between Fig. 5.1 (b) and the picture of the cone without any droplet. Consequently, the

geometry of the droplet is highlighted. We tuned the contrast of the picture to emphasize the top liquid film. Close to the tip of the cone, the droplet has a barrel shape, i.e. wraps the cone, with a deformation due to gravity (the droplet has a thin film above the cone and a hanging part under the cone). As the droplet moves, the droplet switches to a clamshell shape: the droplet does not wrap the cone any longer but sits on the bottom of it. Whatever the shape of the droplet, it moves towards the base of the cone. The change of geometry is the opposite of a roll-up transition [78, 74, 73]. It occurs on a fiber when the volume of the droplet is reduced or the radius of the fiber is getting larger. Here, we observe this transition with a constant droplet volume and on a fiber that has a conical shape. Thus, as the droplet moves, the local radius of the fiber increases. In the case of cylindrical fibers, an adimensional number, called the reduced volume V^* , has been introduced to predict the transition from one shape to the other [73]. It is the ratio between the volume of the droplet and the cube of the fiber radius and is defined as

$$V^* = \frac{\Omega}{r_f^3}. \quad (5.1)$$

If this number is large, the droplet is expected to adopt a barrel shape and if this number is small, the droplet should have a clamshell shape. In our case, we can use this adimensional number to estimate the position where the transition between barrel and clamshell shapes occurs. Let us note V_t^* the reduced volume at the transition. We can then obtain the transition position given by,

$$x_t^* = \frac{1}{\sin \alpha} \sqrt[3]{\frac{\Omega}{V_t^*}}. \quad (5.2)$$

Below this transition position, the shape adopted by the droplet should be a barrel and beyond, the droplet should switch to a clamshell shape. Experimentally, it is difficult to track the contact line because the droplet is transparent and the shape transition is a smooth process. Therefore, we can experimentally approximate the range of positions where the switch in shape occurs. We found an empirical value for the reduced volume at the transition, $V_t^* = 8$. This value is kept constant for all the post-treatment of our data. In section 5.4.3 there is a discussion about how this empirical value is obtained. The transition positions are denoted in Fig. 5.1, 5.4, 5.5 with vertical lines.

This shape transition is in good agreement with the simulations made by Liang *et al.* [112] using Surface Evolver [79]. They also observed, in their simulations, a transition from a barrel shape to a clamshell shape (without gravity) and, whatever the shape, the droplet goes towards large radii of curvature.

To explain these observations, a model taking into account the balance of the forces exerted on the droplet is developed. The droplet experiences two types of force: the capillary force and the viscous force. In our problem, we have two geometrical configurations, therefore we have to describe both cases independently.

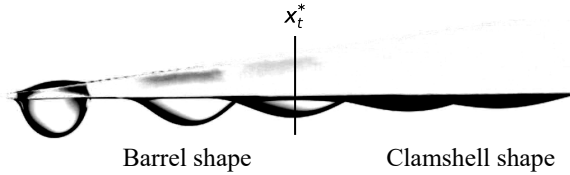


Figure 5.5: Image treatment of the superposition shown in Fig. 5.1 (a). This image treatment, which removes the image of the cone without any droplet, allows to highlight the geometry of the droplet and the contact area of the droplet with the cone as well as the contact line. We tuned the contrast to emphasize the top liquid film. The droplet position along the cone is shown at time $t = 0$ s, 2 s, 7 s, 20 s and 45 s and the experimental parameters are : $\alpha = 4^\circ$ and $\Omega = 4 \mu\text{l}$. One can see that the droplet has a barrel shape close to the tip of the cone and then, as the droplet gets closer to the base, we see a change in geometry from a barrel to a clamshell shape. The vertical black line is the position of transition x_t^* calculated from Eq. (5.2).

5.4.1 Barrel shape

Most of the previous studies consider the motion of axisymmetrical barrel shape droplets moving on conical substrates. The models are based on a driving force coming from a gradient of the Laplace pressure along the surface of the droplet [99, 115]. In our case, the barrel shape is not axisymmetrical due to gravitational effects. Finding the gradient of Laplace pressure in such a non-symmetrical geometry is a significant problem. This is why we use, for the driving force, the external force applying along the contact line of the droplet. This driving force has been used in the model of Fournier *et al.* [118] to describe the motion of sub-millimetric symmetrical barrel shape droplets on prewetted conical glass fibers. In opposition to Fournier *et al.* [118], we do not consider the two contact lines of the barrel as our conical fiber is not prewetted. In fact, in our case, the advancing contact line of the droplet is wetting a dry surface while, along the receding contact line, the surface is not dewet, the droplet is leaving a thin film. Therefore, the wetting by the advancing contact line is the slower process leading the motion. This is why we only consider the wetting force along the advancing contact line as the main contribution to the driving force. Along the advancing contact line, one can see an apparent contact angle (see Fig. 5.1), we note it θ_{app} . This angle is maximum just after the release of the droplet. The angle decreases as the droplet spreads. The dynamics of the wedge angle of a droplet θ on a flat surface is given by the law of Tanner $\theta \sim (\nu\rho\Gamma\dot{x}/\gamma)^{1/3}$, where Γ is a constant that takes the value 15 if liquid slides on a dry surface as showed by Hoffman [41]. Figure 5.6 shows a double logarithmic graph of the apparent contact angle as a function of the speed. We find a slope of 1/2 instead of 1/3 as Tanner's law provides. Therefore, to characterize the dynamics of the apparent contact angle on a cone, we use this law: $\theta_{app} \sim (\nu\rho\Gamma\dot{x}/\gamma)^{1/2}$. The capillary length, l_c , describes the competition between capillary effects and gravitational effects. We have $l_c = \sqrt{\gamma/(\rho g)} = 1.5 \cdot 10^{-3}$ m. With a bottom view of the fiber, one observes that the width of the hanging part of the barrel shape droplet is roughly constant as shown in Figure 5.7 (a). Actually, it has the same order of magnitude as the capillary length. This width, noted ξ ,

can be scaled thanks to the volume of the droplet with the relation $\xi \sim \Omega^{1/3}$, as illustrated in Figure 5.7 (b). So, we assume that the capillary force is acting on a length scale comparable to this characteristic length. This leads to a constant driving force given by

$$F_{\gamma,barrel} \sim \gamma\Omega^{1/3}. \quad (5.3)$$

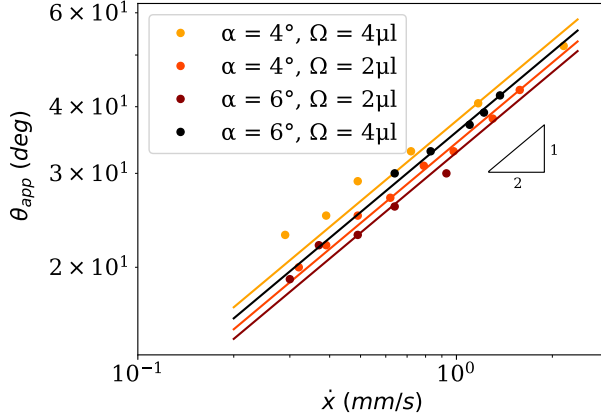


Figure 5.6: Double logarithmic graph of the apparent contact angle of barrel shape droplets θ_{app} as a function of the droplet speed \dot{x} , for different half-angles and volumes: $\alpha = 4^\circ$, $\Omega = 4 \mu\text{l}$; $\alpha = 4^\circ$, $\Omega = 2 \mu\text{l}$; $\alpha = 6^\circ$, $\Omega = 4 \mu\text{l}$; $\alpha = 6^\circ$, $\Omega = 2 \mu\text{l}$. The experimental data points are fitted with a power law with exponent $1/2$.

Now, let us look at the expression of the viscous force. We manage to perform experiments with droplets full of fluorescent particles (Fluostar EBM, $15 \mu\text{m}$) in order to see the motion of the liquid inside the droplet. A movie is available in the video accessible via the QR code in Fig. 5.8. We observe a circulation of the fluorescent particles towards the advancing liquid wedge. Therefore we assume that the dissipation in the front liquid wedge is dominating. Lorenceau *et al.* [99] explained that the viscous stress is given by $\rho\nu\dot{x}r_f\Gamma/\theta$. For our system, one obtains the following dissipating force in the liquid wedge,

$$F_{wedge} \sim \gamma x \sin \alpha \left(\frac{\nu\rho\Gamma\dot{x}}{\gamma} \right)^{1/2}. \quad (5.4)$$

The balance of these forces acting on the droplet can be written as

$$\gamma\Omega^{1/3} - \gamma x \sin \alpha \left(\frac{\nu\rho\Gamma\dot{x}}{\gamma} \right)^{1/2} = \rho\Omega\ddot{x}, \quad (5.5)$$

where \ddot{x} is the acceleration of the droplet. We study the stationary equation that gives the speed limit of the droplet for each position along the cone. One obtains

$$\dot{x} \sim \frac{\gamma}{\nu\rho\Gamma} \frac{\Omega^{2/3}}{(x \sin \alpha)^2}. \quad (5.6)$$

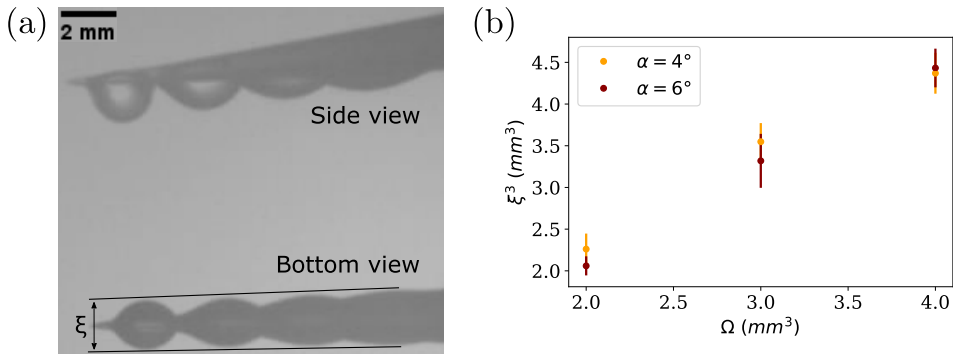


Figure 5.7: (a) Superpositions of pictures of a droplet moving along the cone with two different views, side view and bottom view, taken simultaneously. With the bottom view one can see that the width ξ of the barrel shape droplet is roughly constant. The experimental parameters are : $\alpha = 4^\circ$ and $\Omega = 3 \mu l$. (b) Graph of the width of the barrel shape droplet to the power three as a function of the volume of the droplet and for different half-angles. The width of the droplet can be scaled by the cube root of the volume.



Figure 5.8: QR code to access an experimental video of a silicone oil droplet full of fluorescent particles moving along a conical cone ($\alpha = 6^\circ$, $\Omega = 4 \mu l$). The fluorescent particles inside the droplet facilitate the visualization of the internal liquid motion. The vertical red line marks the expected position where the droplet's shape transitions. On the left of this line, the droplet exhibits a barrel shape, while on the right, it has a clamshell shape.

The model for the barrel shape predicts a linear dependency between the speed and the square of the inverse position. In Fig. 5.4, one can observe a slope of two for large values of $1/x$, namely when the droplet adopts a barrel shape. We will check the scaling in section 5.4.3.

5.4.2 Clamshell shape

A droplet with a clamshell shape set only on one side of the fiber. That kind of droplet hanging under a cone has a non-symmetrical front-rear contact line. If the droplet goes from the tip to the base of the cone, the radius of curvature at the front of the droplet is larger than the one at the rear. The droplet with a clamshell shape is thin, it is a flat droplet. For the driving force, we assume that it is the same expression as the one developed for thin symmetrical barrel shape droplets.

We have

$$F_{\gamma,clam} \sim \gamma\Omega/(x^2 \sin \alpha). \quad (5.7)$$

This expression comes from the Laplace law applied in the case of thin barrel shape droplets (see Eqs. (1.58) and (1.59)) [99].

For the viscous force, we assume that the dissipation inside the liquid close to the fiber dominates. Indeed, as we can see in the video accessible with the QR code in Fig. 5.8, when the droplet has a clamshell shape, the fluorescent particles are stretched in the fluid layers during the motion. This film dissipation is given by,

$$F_{film} \sim \nu\rho\Gamma \frac{e}{\omega} x\dot{x} \sin \alpha, \quad (5.8)$$

where e is the spread of the droplet ($e = x_+ - x_-$) and ω is the thickness of the thin liquid film where the dissipation occurs [99]. For the description of the position over time for a droplet experiencing a film dissipation, we have

$$\frac{\gamma}{\sin \alpha} \frac{\Omega}{x^2} - \nu\rho\Gamma \sin \alpha \frac{e}{\omega} x\dot{x} = \rho\Omega\ddot{x}. \quad (5.9)$$

The stationary expression is therefore given by

$$\dot{x} \sim \frac{\gamma}{\nu\rho\Gamma} \frac{\omega}{e} \frac{1}{\sin^2 \alpha} \frac{\Omega}{x^3}. \quad (5.10)$$

This is the same model as the one developed by Lorenceau *et al.* to explain the motion of symmetrical barrel shape droplets. With the present description, we extend this model to the case of clamshell shape droplets. The model for the clamshell shape predicts a speed proportional to the cube of the inverse position, as can be seen in Fig. 5.4 (range of small values of $1/x$). Also, the speed is linked to the droplet volume and the half-angle of the cone. We will check this scaling in the following section.

5.4.3 Analysis of the models

We have proposed in the previous sections two specific models for both regimes corresponding to different shapes. We now have to fix the range of x corresponding to each geometry. Therefore, we need to estimate the transition position x_t^* . To find the empirical value of the reduced volume at the transition, we tune the boundary between the two regimes until the models fit best the data for both regimes. Then, we confirm the given position transition (Eq. (5.2)) by looking at the experimental movies and see that the found range is well approximated. Indeed, thanks to image treatments like the one illustrated in Fig. 5.5, we can see where the droplet has a barrel shape or a clamshell shape. Also, the reduced volume at the transition can be confirmed by the fact that the droplet should change its shape when the width of the droplet corresponds to the diameter of the fiber. Therefore, we have $r_t^* \approx \sqrt[3]{\Omega}/2$, and with Eq. (5.1), we have $V_t^* = \Omega/r_t^{*3} \approx 8$. With that we obtain the range of positions corresponding to the barrel shape and to the clamshell shape. We can fit the data of the speed as a function of the inverse position for both regions with the corresponding model.

For the barrel shape, the model predicts that the speed goes as the square of the inverse position (Eq. (5.6)). The proportionality coefficient is the fitting parameter noted a_b . We have,

$$\dot{x} = \frac{a_b}{x^2}. \quad (5.11)$$

This fitting law is plotted with a straight grey line in Fig. 5.4, and we see that it is in good agreement with our experimental data. The fits are in excellent agreement for all our data except for the half-angle $\alpha = 3^\circ$ (determination coefficient of those fits are $r^2 \approx 0.94$). In Fig. 5.9, we have plotted $a_b \Omega^{-2/3} \sin^2 \alpha$ as a function of α . We have $a_b \Omega^{-2/3} \sin^2 \alpha \approx 0.08$ mm/s. According to Eq. (5.6), this expression can also be estimated with $\gamma/(\nu\rho\Gamma) \approx 0.03$ mm/s, which is the same order of magnitude. In Fig. 5.9, one observes that the ratio $a_b \Omega^{-2/3} \sin^2 \alpha$ is independent of the volume. The influence of the volume is well described by the model. One can also observe that this ratio increases with the half-angle. This highlights a limitation of the model, it overestimates the influence of the half-angle. Different reasons could explain this observation. The capillary force acts mainly where the apparent contact angle is the largest and we have scaled this length with the width of the droplet. The barrel shape has a symmetrical shape neither rear-front nor top-bottom. Moreover, the advancing contact line is inclined as the droplet is moving. A more precise description of the shape and the length of the contact line should provide a better scaling for the half-angle of the cone.

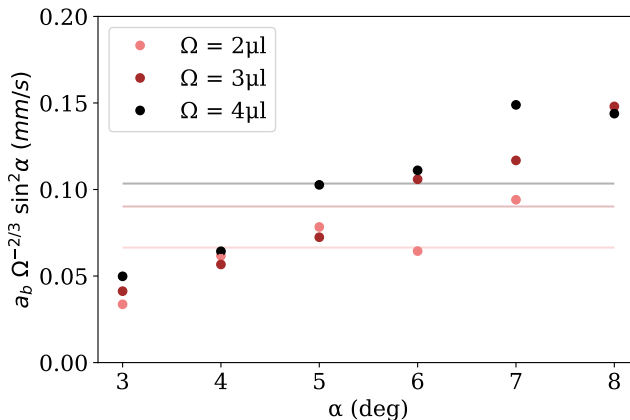


Figure 5.9: Graph of $a_b \Omega^{-2/3} \sin^2 \alpha$, where a_b is the fitting parameter for the barrel shape description, as a function of the half-angle and for different volumes. This parameter a_b represents the proportionality factor between the speed and the inverse of position to the power two (Eq. (5.11)). Therefore, the higher it is, the higher the speed is. It increases with the droplet volume and decreases with the half-angle of the cone. The model overestimates the influence of the half-angle. The error bars are smaller than the size of the symbols. The horizontal lines correspond to an average.

For the clamshell shape, the model predicts that the speed goes as the cube of the inverse of the position (Eq. (5.10)). We note the proportionality coefficient a_c and

it is the fitting parameter. We obtain

$$\dot{x} = \frac{a_c}{x^3}. \quad (5.12)$$

This fitting law is plotted with a dashed grey line in Fig. 5.4. Our model for the clamshell shape seems to depict the good trend of our experimental data. On the graph presented in Fig. 5.10, showing $a_c \sin^2 \alpha$ as a function of the half-angle, one can see that the speed of a droplet with a clamshell shape decreases with the half-angle and increases with the volume, as predicted by our model. By looking at the expression of the speed (Eq. (5.10)), one can see that the speed tends to zero for very large positions. It is known that there is no equilibrium position for the clamshell shape if no external forces apply (gravity or contact angle hysteresis) [158, 121]. We reinforce this result with our observations. With the fitting parameter a_c , the ratio ω/e can be calculated. We have $\omega/e \approx a_c \nu \rho \Gamma \sin^2 \alpha / (\gamma \Omega) \approx 10^{-2}$. It is a realistic order of magnitude because the spread is $e \approx 10^{-3}$ m and ω is the thickness of the layers of fluid where film dissipation occurs, having $\omega \approx 10^{-5}$ m is acceptable.

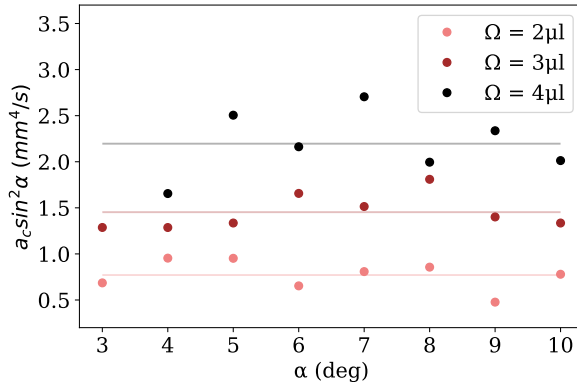


Figure 5.10: Graph of $a_c \sin^2 \alpha$, where a_c is the fitting parameter for the clamshell shape description, as a function of the half-angle and for different volumes. This parameter a_c represents the slope of the speed as a function of the cube of the inverse position (Eq. (5.12)). Therefore, the higher this coefficient is, the higher the speed is. The speed of a clamshell shape droplet increases with the droplet volume and decreases with the half-angle of the cone. The error bars are smaller than the size of the symbols. The horizontal lines correspond to an average and give the trend expected by the model.

5.5 Discussion: Grooved conical fibers

We have described the motion of both barrel and clamshell shaped droplets along a conical fiber. In Chapter 2, we discussed the influence of curved grooves with epicycle (convex) and hypocycle (concave) grooves, on droplet spreading. One potential enhancement involves adding such grooves to conical fibers, as explored by Hu *et al* [122] and Li *et al.* [123], who studied concave and convex grooves on cones, respectively. Let us now compare our study with these two recent works from the literature.

Firstly, we examine the case of droplets moving on concave grooved conical fibers. Hu *et al.* manufacture these concave grooved fibers using a casting technique, with a conical angle of 11.4° and a length of 2 mm. They name their fibers PCCF, which stands for Pyramid-structured with Concave Curved surface Fibers. Four fibers are studied, a plain conical fiber and conical fibers with three, four and five concave grooves, termed tri-PCCF, tetra-PCCF and penta-PCCF, respectively. Images of the fibers are shown in Fig. 5.11 (a). One notices that the cross-sections have large concave grooves with smaller microridges along the longitudinal direction. The plain conical fiber's cross-section exhibits a convex curvature with microridges.

They release water droplets at the tip of the fibers and observed a directional motion towards the base of the cone, see Fig. 5.11 (b). More specifically, the tri-PCCF demonstrates the highest droplet velocity compared to the other PCCFs or even natural fibers, as shown in Fig. 5.11 (c). The recorded speed is 28.79 mm/s on dry tri-PCCF and 47.34 mm/s on wet tri-PCCF. Comparing the tri-PCCF to the plain conical fiber, they observe a longer precursor film on the PCCF than on the conical fiber, with liquid spreading inside the concave groove upstream of the droplet. Also, the advancing meniscus has a convex shape on PCCF and a concave one on the plain conical fiber, as sketched in Fig. 5.11 (b). The highest velocity observed on tri-PCCF, compared to the other PCCFs (tetra and penta), is attributed to the decreasing cross-sectional surface as the number of grooves increases. They state this cross-sectional surface influences the droplet length on the PCCF, which is assumed to increase as the number of grooves decreases, leading to the longest droplet on the tri-PCCF. A longer droplet results in a larger capillary force. Unfortunately, this is the only empirical explanation provided in the article, no further study of the curvature radius is explored. Nevertheless, this article highlights an important observation, concave grooves indeed increase droplet speed on conical fibers, and this speed is influenced by the cross-sectional surface of the conical fiber.

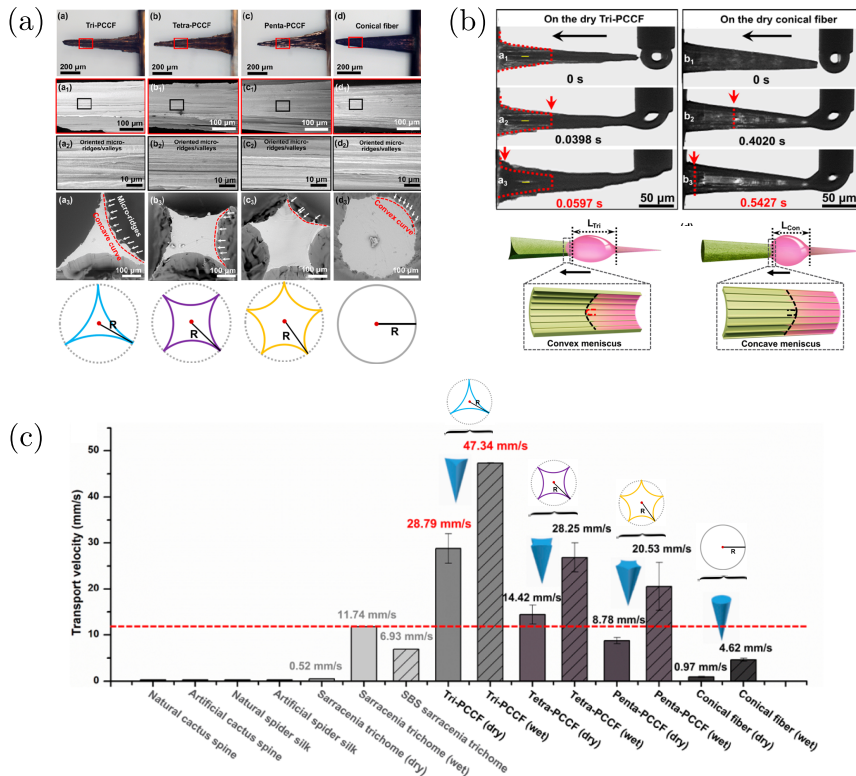


Figure 5.11: (a) Images of the conical fibers with concave grooves, from left to right with three, four and five grooves, termed as tri-, tetra-, penta-PCCFs. On the far right, it is a plain conical fiber. The images below are SEM images showing the microridges present on the surface. The bottom pictures show the cross-section of each conical fiber, highlighting the major concave grooves and smaller microridges. (b) A water droplet is released at the tip of a dry tri-PCCF (left) and a dry plain conical fiber (right). The droplet moves faster on the tri-PCCF, attributed to three factors: the upstream precursor film that invades the grooves, the convex shape of the meniscus, and the smaller cross-section of the fiber that induces a longer droplet. (c) Comparison of water droplet velocities on various conical fibers. Light grey bars are natural and artificial conical fibers, taken from previous literature (see [122]). Dark grey bars show the velocity values observed in the study of Hu *et al.*, with both dry and wet tri-PCCF allowing the fastest droplet motion. From [122].

Secondly, we examine the case of droplets moving on convex grooved conical fibers. Li *et al.* use 3D printing technology to create conical fibers with two to five grooves, having a conical angle of 9° and a length of 20 mm. These conical fibers possess the same circumscribed radius, as shown in Fig. 5.12 (a). In their experiment, the cones are oriented downward and are immersed in water, with an oil droplet ($1.2\text{-}\mu\text{l}$ dichloroethane) placed at the tip. This setup enables an anti-gravity study, and one observes the $6\text{-}\mu\text{l}$ droplet to move towards the base of the cone. Experimental images are shown in Fig. 5.12 (b). The highest droplet velocity is observed on

conical fibers with two grooves, with an average velocity of 8.28 mm/s. The velocity decreases as the number of grooves increases, as seen in Fig. 5.12 (d). Also, on a conical fiber without any grooves, the droplet initially moves upward before becoming pinned, resulting in a null average speed. Similar to the observations with concave grooves, the precursor film invades the grooves upstream of the droplet and the fiber cross-section decreases as the number of grooves decreases, which increases the droplet length.

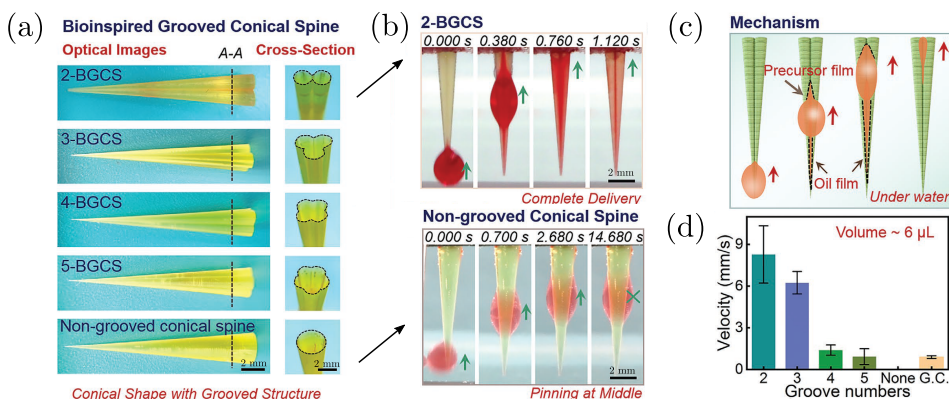


Figure 5.12: (a) 3D-printed conical fibers with convex grooves, arranged from top to bottom: 2 grooves, 3 grooves, 4 grooves, 5 grooves and a non-grooved conical fiber. The term BGCS stands for Bioinspired Grooves Conical Spine. The images on the right side show the cross-section of each cone. (b) In the experiment, the cones are placed downward under water, and an oil droplet ($\Omega = 6 \mu\text{l}$) is deposited at the tip of the 2-grooved conical fiber (top) and on a non-grooved conical fiber (bottom). The droplet moves upward along the all cone on the 2-grooved cone. On the non-grooved conical fiber, the droplet initially moves upward and then stops at a certain position. (c) Schematic illustration of the droplet motion on a cone with two convex grooves, highlighting the precursor film that rises ahead of the droplet. (d) Measured average droplet velocity for each type of conical fiber. The velocity decreases as the number of grooves increases. The velocity is null for the non-grooved conical fiber (none case) and is small for grooved cylindrical fiber (G. C. case). From [123].

Direct comparison with our work is complex due to the use of different liquids (water for Hu *et al.*, 1,2-dichloroethane oil for Li *et al.*, and silicone oil for us). In our study, the maximal speed of silicone oil droplets on a 12° dry conical fiber is 1 mm/s (see Fig. 5.4). In Hu's study, the observed speed on dry plain conical fiber is also around 1 mm/s, while on a dry tri-PCCF, it is about 30 times higher. Consequently, one might expect silicone oil droplets to move significantly faster on 3D-printed conical fibers with concave grooves. In Li's study, the experimental setup involves immersed conical fibers, which differs from our approach. The oil droplet on their conical fiber is pinned, resulting in a null velocity, likely due to a remaining effect of gravity. This difference prevents any direct comparison.

5.6 Application for fog collection

Conical fibers can be used for fog harvesting as discussed in section 1.6.3. The spontaneous motion of droplets could enhance collection efficiency by rapidly delivering water droplets. Effective drainage is a crucial aspect of fog collection systems, that could be improved by using conical fibers. In a fog chamber, conical fibers are observed to harvest droplets, with initial droplet formation at the cone tip. The droplet grows and moves towards the base, allowing new droplets to form at the cone tip. As the droplet moves, it coalesces with other droplets deposited on the cone surface. This behavior is significantly different from that of a horizontal cylindrical fiber, where droplets form periodically along the fiber without collisions or motion. This experimental observation is shown in a video accessible via the QR code in Fig. 5.13.



Figure 5.13: QR code to access to an experimental video comparing fog collection on cylindrical and conical fibers. The fog enters from the bottom of the video, and the fibers are observed from beneath. Both fibers are 3 cm long. The cylindrical fiber has a radius of 1.58 mm, while the conical fiber has a half-angle of 6° . The video is accelerated 5 times. This experiment has been performed in the Frugal lab at Université libre de Bruxelles in collaboration with Denis Terwagne.

Regarding cone fog collection, Gurera and Bhushan [16] showed that two 3D-printed cones with the same length but different conical angles (10° and 45°) have the same collection rate, see Fig. 5.14. As discussed in this chapter, the smaller the cone angle, the faster and further the droplet travels. Smaller cone angles are expected to harvest more by allowing faster droplet motion. However, under fog conditions, the experiment differs as droplets are deposited on the entire surface, favoring coalescence. Larger cone angles provide a larger surface area to catch fog droplets. This explains the same water collection rate, although the Laplace force is larger for small cone angles, more droplets are formed on the surface of larger angle cones. Moreover, the droplets fall with the same frequency, regardless of the cone angle and the projected surface area in the fog flow. The falling droplets also have the same weight, which is understandable with the capillarity versus gravity perspective.

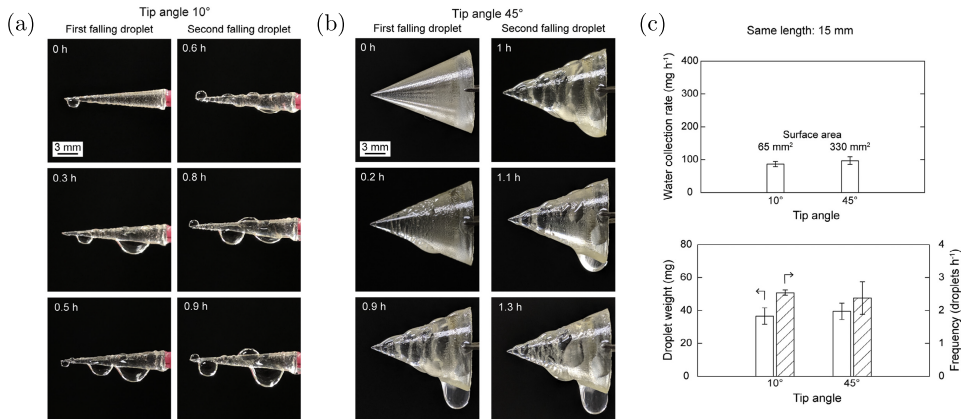


Figure 5.14: (a) and (b) Experimental images of 3D printed cones in a fog chamber. In (a), the cone has a 10° tip angle, while in (b), it has a 45° tip angle. Both cones are of the same length (15 mm). It is observed that the fibers collect water, with droplet formation at their tip, which then moves towards the base and falls. (c) (top) Graph showing the water collection rate for the two different tip angles, note that the surface areas of the fiber differ due to the same cone length. The water collection rate is dependent on the cone length, regardless of the tip angle or surface area. (c) (bottom) Graph of the weight of the fallen droplets and the falling frequency for the two fibers. Despite the different cone angles, the weight of the fallen droplets and their falling frequency remains the same. From [16].

5.7 Conclusion

Conical fibers are manufactured in a highly controllable way using 3D-printing techniques. When a droplet is placed on those synthetic cones, a motion of the droplet is observed from the tip toward the base of the cone. Beyond the capillary length, the shape of the barrel shape droplet is influenced by gravity. We have observed a switch in the geometry of the droplet. This transition is witnessed thanks to the use of dry cones (so that a clamshell shape can be defined) and thanks to a sufficiently long cone or a large half-angle so the position transition can be reached. For small radii, the droplet tends to adopt a barrel shape (deformed by gravity, meaning we have a thin film above the cone and a hanging part under the cone), but if the radius of the fiber is larger, the droplet adopts a clamshell shape. The two different shapes induce two different dynamics. These dynamics are explained with two separate models based on the balance of forces exerted on the droplet. For the barrel shape, the dissipation in the wedge dominates. A study of the evolution of the apparent contact angle with the speed of the droplet allows to adapt Tanner's law for conical fibers. For the driving force, as the barrel shape is not symmetrical, an external capillary force is developed. For the clamshell shape, the dissipation in the thin film layers close to the fiber dominates. The driving force used is the Laplace law applied on thin barrel drops, this expression has been developed by Lorenceau *et al.* [99]. We actually obtain the same model as Lorenceau *et al.* They developed it to explain the motion of symmetrical barrel

shape droplets but we extend it to the case of clamshell shape droplets. If the volume of the droplet is higher, the speed of the droplet is higher too, for both the barrel shape and the clamshell shape droplets. The smaller the half-angle of the cone, the higher the speed for both barrel and clamshell shapes. Note that some experimental dependencies in the barrel shape model are yet to be described. In conclusion, capillary transport is enhanced if the volume of the droplet is large and if the half-angle of the cone is small.

The perspectives of this work are numerous. We could change the surface roughness of the cones by adding grooves, scales or spikes which could be done thanks to 3D-printing. As analyzed in recent literature, both concave and convex grooves improve droplet motion [122, 123]. Another application of conical fibers is in fog harvesting. Utilizing conical fibers could enhance fog collection efficiency by increasing drainage efficiency. Additionally, another way to set a droplet into motion is to put it into a wedge made of two smooth surfaces [159, 160]. It would be interesting to consider curved surfaces and to see if the behavior of the droplet is changed. Duprat *et al.* [107] described the shape of droplets trapped between two parallel cylindrical fibers. Replacing these fibers with conical ones could provoke the motion of the droplets. In conclusion, our study provides a new way for manipulating droplets and offers many new perspectives.

General conclusion and perspectives

6.1 Conclusion

In this thesis, we explored the dynamics of liquid droplets interacting with various structures, focusing on their behavior on grooved substrates, cylindrical fibers and conical fibers. By systematically analyzing how droplets spread or move along these surfaces, we have gained insights into the key physical parameters that enhance droplet motion.

In Chapter 1, we provided an overview of the extensive field of droplet research, covering droplets in fluid environments, on flat and grooved substrates, on cylindrical and conical fibers. We highlighted how the solid substrate geometry deeply affects the droplet shape, spreading and motion. Additionally, we described natural examples of plants that achieve efficient droplet transport, which served as inspiration for our work. We have observed natural fibers and grooves on the plant attributes responsible for fog collection. This background laid the foundation for further studies, we have focused on new ways to initiate and enhance droplet spreading thanks to curved grooves and substrates.

In Chapter 2, we examined the spreading behavior of wetting droplets within curved grooves inscribed on flat substrates. This study revealed that the curvature sign (whether concave or convex) significantly influences the spreading dynamics. We showed that the convex grooves (epicycles) facilitate faster spreading. This enhanced dynamic is attributed to the convex groove cusp that pinches the droplet front, compared to the concave groove where the liquid front spreads more broadly. These findings underscore the importance of grooves on droplet motion. A feature also observed in plants performing water collection.

In Chapter 3, we studied the complete behavior of a single droplet descending on a vertical fiber, from its motion to the destabilization of its coating into new

droplets. We observed that the thickness of the liquid film left behind the droplet is correlated with the droplet speed, the film being thickest at the initial deposition point. At this position, the film destabilizes rapidly due to the Rayleigh-Plateau instability, leading to the formation of a new droplet. We developed models to describe the dynamics of this droplet formed from the destabilized coating.

In Chapter 4, we extended our fiber-based studies to the motion of droplets along twisted fibers. The helical grooves formed by twisting two cylindrical fibers create a substructure that influences droplet descent. Depending on the droplet size relative to the helical pitch, droplets either follow a helical path or move predominantly vertically. Our experiments revealed that both the angular and the vertical speeds are affected by the number of twists, and we proposed models to describe these observations.

In Chapter 5, we investigated the motion of droplets on conical fibers. We showed that the shape and motion of droplets are influenced by the geometry of the fiber. As the droplet moves from the tip to the base of the conical fiber, it transitions from a barrel shape to a clamshell shape, with each shape exhibiting different dynamic behaviors. We developed models to describe these dynamics.

These findings expand our understanding of liquid spreading on both macroscopic structures like fibers and cones, as well as macroscopic substrates decorated with grooves. The study of droplets on fibers provides practical insights for improving draining in water collection systems. Fog collection relies on three distinct efficiencies, this thesis focuses on enhancing drainage efficiency. Two components can be optimized: the droplet and the substrate. For the droplet, larger volume and lower liquid viscosity increase the descent speed. Clamshell shape droplets slide faster due to their smaller contact area with the substrate compared to barrel shape droplets. Regarding the substrate, vertical fibers are an effective way to drain droplets as gravity is used to drive droplet motion. In this configuration, smaller fiber diameter and prewetted fibers increase the droplet speed. Moreover, adding convex grooves by placing two fibers side by side enhances droplet descent. Namely twisted fibers could be advantageous as they promote the rotation of the droplet around the bundle. For horizontal droplet displacement, conical fibers are interesting as droplets on conical fibers move towards the base of the cone, with smaller half-angle resulting in faster droplet speed. Once more, inscribing curved grooves along the cone surface favors the droplet motion.

6.2 Perspectives

Droplets on fiber is a vast area of study, with many intriguing phenomena yet to be unraveled. At the end of each chapter, we discussed perspectives for each case study. Here, we propose two main ideas for future works. Fig. 6.1 shows an overview of the topics addressed in the thesis, as well as potential avenues for future research.

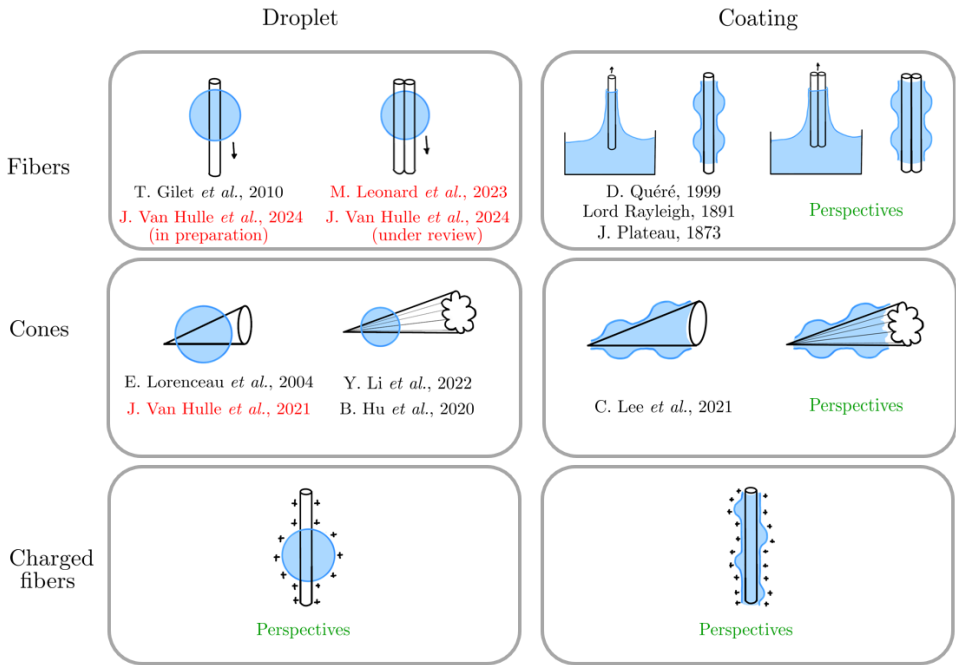


Figure 6.1: Schematic overview of the topics addressed in the thesis and the perspectives it opens. From top to bottom, the substrate changes, ranging from cylindrical fibers to conical fibers and finally to cylindrical charged fibers. From left to right, the liquid geometry changes, depicting both droplets and liquid coatings. The thesis focuses on droplet behavior on fibers. It opens avenues for future research about droplets on charged fibers and liquid coatings on grooved or charged fibers.

First, it would be interesting to investigate the Landau-Levich fluid coating of substrates with substructures, such as grooves. One could withdraw a bundle of fibers from a liquid bath at a controlled speed and examine how grooves affect the liquid film thickness. The bundle of fibers could consist of either two parallel fibers or two twisted fibers. Experimentally, this would be explored by measuring the weight of the fiber bundle to estimate the liquid entrainment. Additionally, the presence of grooves might alter the Rayleigh-Plateau instability, potentially delaying or even preventing the breakup of the liquid film.

Second, we observed interesting phenomena when a silicone oil droplet descends along a vertical charged fiber. A nylon fiber can accumulate static charges when rubbed with a piece of polystyrene. As the silicone oil droplet moves down the charged fiber, it amasses charges that induce a deformation in the droplet shape and sometimes explodes by jumping off the fiber, or expelling tiny jets of liquid, as shown in Fig. 6.2 (a), (b) and (c). Additionally, the liquid coating left behind the droplet can destabilize into a saw-tooth configuration, with deformed barrel or clamshell shapes, see Fig. 6.2 (d). The saw-tooth configuration remains stable due to the electrostatic repulsion between the droplets. Another curious observation is symmetrical barrel shape droplets, which under no charge circumstance would catch up and merge, instead maintaining a constant spacing forming a train of different sized beads that descends along the fiber as observed in Fig. 6.2 (b). Exploring these behaviors could be interesting and could lead to innovative applications, such as devices that control droplet movement between fibers based on applied electric potentials. One could imagine devices where droplets could jump from one fiber to another substrate. Note also the potential application for fog nets that might accumulate charges from wind interactions.

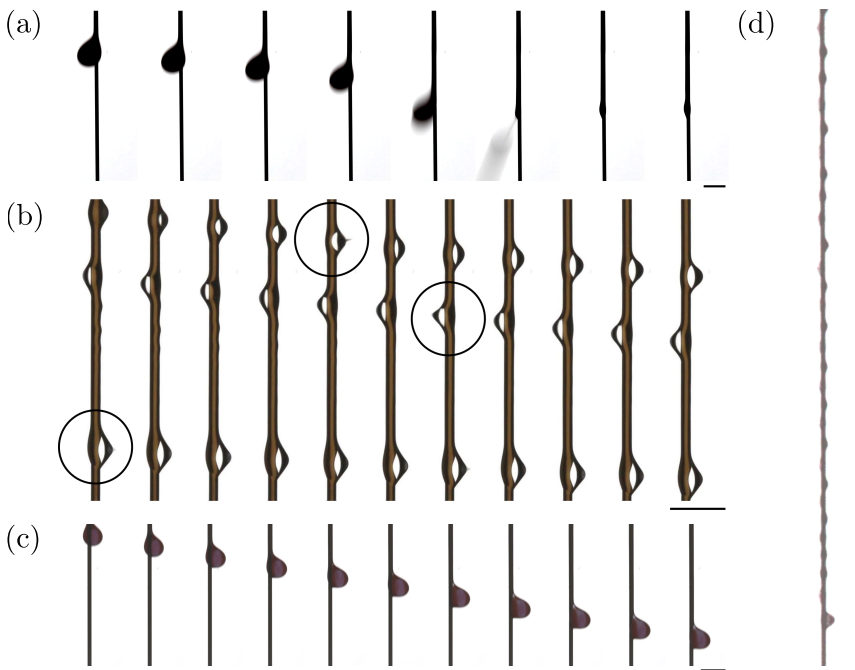


Figure 6.2: Phenomena observed when a silicone oil droplet descends along a charged vertical fiber. (a) The droplet accumulates charges leading to deformation of its shape until it jumps off the fiber. (b) Deformed barrel shape droplet due to the accumulation of electric charges on its surface. The droplets eject tiny jets of liquid (indicated by circles). All droplets slide down the fiber without merging. (c) The droplet transitions from a barrel shape to an asymmetric barrel or a clamshell shape and remains stable in this configuration. (d) Liquid coating on a charged fiber that destabilizes into a saw-tooth pattern. The scale bars correspond to 2 mm. Time intervals for (a), (b) and (c) are 0.04 s, 0.2s and 0.08s, respectively. (Credit: A. Grolet, F. Massoz and C. Traversin)

More than 150 years ago, Joseph Plateau, a notable figure from our University of Liège, first observed the destabilization of liquid coatings. Since then, the interaction between liquids and fibers has continued to fascinate scientists, revealing new and intriguing behaviors. While this thesis has contributed to our understanding, the journey to fully grasp droplet motions and interactions on structured surfaces is far from over, and many exciting discoveries await.

Appendix A

In this appendix, we derive the velocity profile of fluid layers inside a corner, as given in Eq. (1.23) and detailed in [40]. The problem is encountered in Chapter 1, section 1.3.3 and is the following. A droplet is spreading on a substrate, the contact line advances with a speed U and the dynamical contact angle θ_D decreases as the droplet spreads. One can zoom on one edge of the droplet and one obtains a liquid corner, as depicted in Fig. A.1.

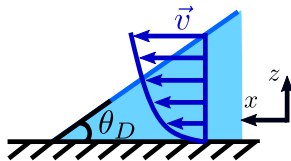


Figure A.1: Advancing wedge of fluid with a dynamical contact angle θ_D . The velocity profile v of the fluid layers (in dark blue) is parabolic as demonstrated in this Appendix.

The speed is along the x -axis, and the fluid is assumed stationary and incompressible. This later implies $\vec{\nabla} \cdot \vec{v} = 0$, leading to $\vec{v} = v(z)\vec{e}_x$. To express the velocity profile, we use the Navier-Stokes equation, which describes the conservation of momentum at any point in the fluid,

$$\rho \frac{\partial \vec{v}}{\partial t} + \rho (\vec{v} \cdot \vec{\nabla}) \vec{v} = \rho \vec{g} - \vec{\nabla} p + \eta \Delta \vec{v}, \quad (\text{A.1})$$

where \vec{v} is the local flow velocity and p is the local pressure. On the x -axis, one obtains,

$$v_x(z) = \frac{1}{\eta} \frac{\partial p}{\partial x} \frac{z^2}{2} + Cz + C' \quad (\text{A.2})$$

where C and C' are two integration constants. Considering two boundary conditions, namely the assumption of a non-slipping fluid, $v_x(z=0) = 0$, and no tangential constraints at the free surface, $\left(\frac{dv_x}{dz}\right)_{z=\zeta} = 0$, where ζ is a given thickness in the corner (expressed as $\zeta = \theta_D x$), yields,

$$v_x(z) = \frac{1}{\eta} \frac{\partial p}{\partial x} \left(\frac{z^2}{2} - \zeta z \right) \quad (\text{A.3})$$

To find the expression for the derivative of the pressure, we express the mean velocity along the profile, U , [40] one has

$$U = \frac{1}{\zeta} \int_0^\zeta v(z) dz = -\frac{1}{\eta} \frac{\partial p}{\partial x} \frac{\zeta^2}{3}. \quad (\text{A.4})$$

This leads to

$$\frac{\partial p}{\partial x} = -U\eta \frac{3}{\zeta^2}. \quad (\text{A.5})$$

Finally, one can rewrite the expression for $v_x(z)$ (see Eq. (A.3)) as

$$v_x(z) = \frac{3}{2} \frac{U}{\zeta^2} (-z^2 + 2\zeta z). \quad (\text{A.6})$$

This is the velocity profile along the x -axis that establishes inside a corner of fluid that spreads on a flat horizontal surface, as given in Chapter 1, section 1.3.3, Eq. (1.23). The velocity profile of the fluid layers is parabolic, as sketched in Fig. A.1.

Appendix B

In this Appendix, we calculate the Rayleigh-Plateau wavelength λ_{RP} using a linear stability analysis. This wavelength appears when a liquid film coating a fiber destabilizes. The fiber has a radius r_f , the initial liquid film thickness is noted e_0 . One considers the liquid film to be thin, $e_0 \ll r_f$. The orientation of the fiber defines the x -axis, the other coordinate is the polar r -axis which is perpendicular to the previous one, as shown in Fig. B.1 (a).

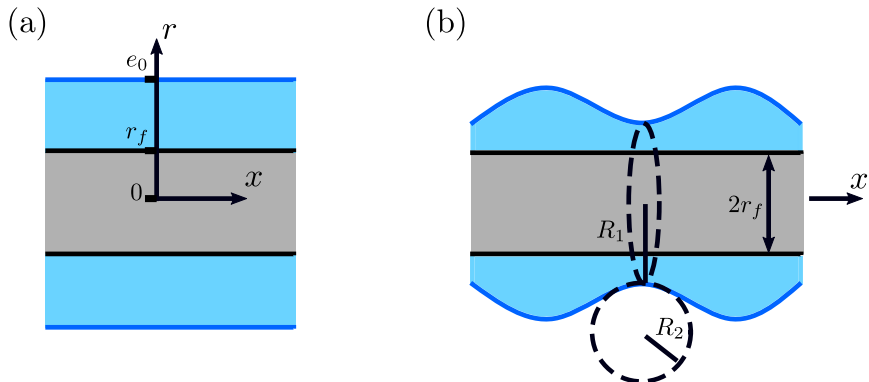


Figure B.1: (a) Illustration of the liquid coating on a fiber. The initial thickness of the liquid film is noted e_0 and the radius of the fiber is r_f . This liquid film destabilizes as illustrated in (b). The deformation of the interface is characterized by two curvatures, R_1 and R_2 .

Several assumptions are needed to simplify the Navier-Stokes equation (Eq. (A.1)) that governs the liquid flow inside the liquid film. The calculation is made for a stationary and incompressible flow. The flow is considered unidirectional along the x -axis, with the velocity profile that only depends on the r -axis. Furthermore, the pressure gradient inside the fluid only depends on the coordinate r . It yields, the Poiseuille equation

$$-\frac{\partial p}{\partial x} + \eta \frac{\partial^2 v_x}{\partial r^2} = 0. \quad (\text{B.1})$$

Integrating this equation along the r -coordinate gives

$$v_x(r) = \frac{1}{\eta} \frac{\partial p}{\partial x} \frac{r^2}{2} + Cr + C', \quad (\text{B.2})$$

where C and C' are two integration constants. To calculate these constants, we take the following boundary conditions:

- No slipping on the fiber : $v_x(r = r_f) = 0$.
- No tangential constrains along the free surface : $\frac{\partial v_x}{\partial r} \Big|_{r=r_f+e} = 0$.

One obtains the following expression for the velocity profile

$$v_x(r) = \frac{1}{2\eta} \frac{\partial p}{\partial x} (r^2 + r_f^2 - 2r(r_f + e) + 2er_f). \quad (\text{B.3})$$

Consequently, the linear flow rate, noted q is

$$Q = \int_{r_f}^{r_f+e} v_x(r) dr = -\frac{1}{3\eta} \frac{\partial p}{\partial x} e^3. \quad (\text{B.4})$$

One needs to express the pressure p and its dependence with the x -coordinate. The pressure inside the liquid film comes from the deformation of the interface and more specifically its curvature, as illustrated in Fig. B.1 (b). The Laplace pressure is given by

$$p = \gamma \left(\frac{1}{R_1} + \frac{1}{R_2} \right) = \gamma \left(\frac{1}{r_f + e} - \frac{\partial^2 e}{\partial x^2} \right). \quad (\text{B.5})$$

This leads to the following expression of the linear flow rate

$$Q = \frac{\gamma}{3\eta} e^3 \left(\frac{1}{r_f^2} \frac{\partial e}{\partial x} + \frac{\partial^3 e}{\partial x^3} \right). \quad (\text{B.6})$$

This linear flow rate is used in the following development.

The mass conservation in a portion of fluid dx and per unit length is

$$\frac{\partial e}{\partial t} = -\frac{\partial Q}{\partial x}. \quad (\text{B.7})$$

With Eq. (B.6) and with $e = e^* + \delta e \cos(qx)$ where e^* is the average thickness and q the wave vector related to the wavelength ($\lambda = 2\pi/q$), one obtains

$$\frac{\partial \delta e}{\partial t} = \frac{\gamma}{3\eta r_f^2} e^{*3} q^2 (1 - q^2 r_f^2) \delta e. \quad (\text{B.8})$$

This expression is given for the first order of δe . Finally, one assumes $\delta e \propto \exp(\sigma t)$ with σ being the rate of growth. One has

$$\sigma(q) = \frac{\gamma}{3\eta r_f^2} e^{*3} q^2 (1 - q^2 r_f^2). \quad (\text{B.9})$$

The wavelength taken by the system is the one that maximizes this rate of growth. The solution is $q_{RP} = 1/\sqrt{2}r_f$. The Rayleigh-Plateau wavelength is thus

$$\lambda_{RP} = \frac{2\pi}{q_{RP}} = 2\pi\sqrt{2}r_f. \quad (\text{B.10})$$

Bibliography

- [1] WWAP, *The United Nations World Water Development Report 2023: partnerships and cooperation for water*. Paris: UNESCO, (2023).
- [2] D. Gurera and B. Bhushan, *Passive water harvesting by desert plants and animals: lessons from nature*, *Phil. Trans. R. Soc. A*, **378**, 20190444, (2020).
- [3] Y. Zheng, H. Bai, Z. Huang, X. Tian, F. Q. Nie, Y. Zhao, J. Zhai, and L. Jiang, *Directional water collection on wetted spider silk*, *Nature*, **463**, 640–643, (2010).
- [4] H. Chen, T. Ran, Y. Gan, J. Zhou, Y. Zhang, L. Zhang, D. Zhang, and L. Jiang, *Ultrafast water harvesting and transport in hierarchical microchannels*, *Nature Mater.*, **17**, 935–942, (2018).
- [5] J. Ju, H. Bai, Y. Zheng, T. Zhao, R. Fang, and L. Jiang, *A multi-structural and multi-functional integrated fog collection system in cactus*, *Nature Commun.*, **3**, 1247, (2012).
- [6] Z. Pan, W. G. Pitt, Y. Zhang, N. Wu, Y. Tao, and T. T. Truscott, *The upside-down water collection system of *Syntrichia caninervis**, *Nature Plants*, **2**, 1–5, (2016).
- [7] P. Comanns, G. Buchberger, A. Buchsbaum, R. Baumgartner, A. Kogler, S. Bauer, and W. Baumgartner, *Directional, passive liquid transport: the texas horned lizard as a model for a biomimetic ‘liquid diode’*, *J. R. Soc. Interface*, **12**, 20150415, (2015).
- [8] T. Nørgaard and M. Dacke, *Fog-basking behaviour and water collection efficiency in Namib Desert Darkling beetles*, *Front. Zool.*, **7**, 1–8, (2010).
- [9] K.-C. Park, S. S. Chhatre, S. Srinivasan, R. E. Cohen, and G. H. McKinley, *Optimal design of permeable fiber network structures for fog harvesting*, *Langmuir*, **29**, 13269–13277, (2013).
- [10] M. Azeem, M. T. Noman, J. Wiener, M. Petru, and P. Louda, *Structural design of efficient fog collectors: A review*, *Environ. Technol. & Innovation*, **20**, 101169, (2020).
- [11] B. Khalil, J. Adamowski, A. Shabbir, C. Jang, M. Rojas, K. Reilly, and B. Ozga-Zielinski, *A review: dew water collection from radiative passive col-*

- lectors to recent developments of active collectors, *Sustainable Water Resources Management*, **2**, 71–86, (2016).
- [12] D. Beysens, *Dew water*. River Publishers, (2022).
- [13] W. Liu, P. Fan, M. Cai, X. Luo, C. Chen, R. Pan, H. Zhang, and M. Zhong, *An integrative bioinspired venation network with ultra-contrasting wettability for large-scale strongly self-driven and efficient water collection*, *Nanoscale*, **11**, 8940–8949, (2019).
- [14] L. Ding, S. Dong, Y. Yu, X. Li, and L. An, *Bionic surfaces for fog collection: A comprehensive review of natural organisms and bioinspired strategies*, *ACS Appl. Bio Mater.*, **6**, 5193–5209, (2023).
- [15] B. S. Kennedy and J. B. Boreyko, *Bio-inspired fog harvesting meshes: A review*, *Adv. Funct. Mater.*, 2306162, (2023).
- [16] D. Gurera and B. Bhushan, *Optimization of bioinspired conical surfaces for water collection from fog*, *J. Colloid Interface Sci.*, **551**, 26–38, (2019).
- [17] E. Reyssat, F. Chevy, A.-L. Biance, L. Petitjean, and D. Quéré, *Shape and instability of free-falling liquid globules*, *Europhys. Lett.*, **80**, 34005, (2007).
- [18] A. Marchand, J. H. Weijs, J. H. Snoeijer, and B. Andreotti, *Why is surface tension a force parallel to the interface?*, *Am. J. Phys.*, **79**, 999–1008, (2011).
- [19] P. de Gennes, F. Brochard-Wyart, and D. Quéré, *Gouttes, bulles, perles et ondes*. Collection Échelles, Belin, Paris, (2005).
- [20] E. Guyon, J.-P. Hulin, and L. Petit, *Hydrodynamique physique*. EDP Sciences and CNRS Editions, Paris, (2001).
- [21] L. Rayleigh, *XVI. On the instability of a cylinder of viscous liquid under capillary force*, *The London, Edinburgh, and Dublin Philosophical Magazine and Journal of Science*, **34**, 145–154, (1892).
- [22] J. A. F. Plateau, *Statique expérimentale et théorique des liquides soumis aux seules forces moléculaires: Tome premier*, vol. 2. Gauthier-Villars, (1873).
- [23] L. Rayleigh, *Some applications of photography*, *Nature*, **44**, 249–254, (1891).
- [24] F. Brochard, *Spreading of liquid drops on thin cylinders: The “marchon/droplet” transition*, *J. Chem. Phys.*, **84**, 4664–4672, (1986).
- [25] J. F. Joanny and P.-G. de Gennes, *A model for contact angle hysteresis*, *J. Chem. Phys.*, **81**, 552–562, (1984).
- [26] D. Quéré, *Rough ideas on wetting*, *Physica A*, **313**, 32–46, (2002).
- [27] D. Bonn, J. Eggers, J. Indekeu, J. Meunier, and E. Rolley, *Wetting and spreading*, *Rev. Mod. Phys.*, **81**, 739–805, (2009).
- [28] C. Furmidge, *Studies at phase interfaces. I. The sliding of liquid drops on solid surfaces and a theory for spray retention*, *J. Colloid Sci.*, **17**, 309–324, (1962).

- [29] Y. I. Frenkel, *On the behavior of liquid drops on a solid surface. 1. The sliding of drops on an inclined surface*, J. Exp. Theor. Phys., **18**, 659, (1948). Translated by V. Berejnov.
- [30] B. S. Massey and J. Ward-Smith, *Mechanics of fluids*, vol. 1. Crc Press, (1998).
- [31] E. Villermaux and B. Bossa, *Single-drop fragmentation determines size distribution of raindrops*, Nature Phys., **5**, 697–702, (2009).
- [32] A. M. Cazabat and M. A. Cohen Stuart, *Dynamics of wetting on smooth and rough surfaces*, Prog. Colloid Polym. Sci., **74**, 69–75, (1987).
- [33] H. P. Kavehpour, B. Ovrin, and G. H. McKinley, *Microscopic and macroscopic structures of the precursor layer in spreading viscous drops*, Phys. Rev. Lett., **91**, 196104, (2003).
- [34] W. B. Hardy, III. *The spreading of fluids on glass*, Philos. Mag., **38**, 49, (1919).
- [35] A. M. Cazabat, *How does a droplet spread?*, Contemp. Phys., **4**, 347–364, (1987).
- [36] M. N. Popescu, G. Oshanin, S. Dietrich, and A.-M. Cazabat, *Precursor films in wetting phenomena*, J. Phys.: Condens. Matter, **24**, 243102, (2012).
- [37] J. F. Joanny and P.-G. de Gennes, *Upward creep of a wetting fluid : a scaling analysis*, J. Phys., **47**, 121–127, (1986).
- [38] J. De Coninck, M. J. de Ruijter, and M. Voué, *Dynamics of wetting*, Curr. Opin. Colloid Interface Sci., **6**, 49–53, (2001).
- [39] S. L. Cormier, J. D. McGraw, T. Salez, E. Raphaël, and K. Dalnoki-Veress, *Beyond Tanner’s law: Crossover between spreading regimes of a viscous droplet on an identical film*, Phys. Rev. Lett, **109**, 154501, (2012).
- [40] P.-G. de Gennes, *Wetting: statics and dynamics*, Rev. Mod Phys., **57**, 827, (1985).
- [41] R. L. Hoffman, *A study of the advancing interface. I. Interface shape in liquid—gas systems*, J. Colloid Interface Sci., **50**, 228–241, (1975).
- [42] J. Bico and D. Quéré, *Falling slugs*, J. Colloid Interface Sci., **243**, 262–264, (2001).
- [43] A. M. Cazabat and M. A. Cohen Stuart, *Dynamics of wetting: Effects of surface roughness*, J. Phys. Chem., **90**, 5845–5849, (1986).
- [44] L. H. Tanner, *The spreading of silicone oil drops on horizontal surfaces*, J. Phys. D: Appl. Phys., **12**, 1473–1484, (1979).
- [45] A. E. Seaver and J. C. Berg, *Spreading of a droplet on a solid surface*, J. Appl. Polym. Sci., **52**, 431–435, (1994).
- [46] J. Lopez, C. A. Miller, and E. Ruckenstein, *Spreading kinetics of liquid drops on solids*, J. Colloid Interface Sci., **56**, 460–468, (1976).

- [47] J. Cai, Y. Chen, Y. Liu, S. Li, and C. Sun, *Capillary imbibition and flow of wetting liquid in irregular capillaries: A 100-year review*, Adv. Colloid Interface Sci., **304**, 102654, (2022).
- [48] V. R. Lucas, *Ueber das zeitgesetz des kapillaren aufstiegs von flüssigkeiten*, Kolloid Z., **23**, 15–22, (1918).
- [49] E. W. Washburn, *The dynamics of capillary flow*, Phys. Rev., **17**, 273–283, (1921).
- [50] J. M. Bell and F. Cameron, *The flow of liquids through capillary spaces*, J. Phys. Chem., **10**, 658–674, (2002).
- [51] P. Kolliopoulos, K. S. Jochem, D. Johnson, W. J. Suszynski, L. F. Francis, and S. Kumar, *Capillary-flow dynamics in open rectangular microchannels*, J. Fluid Mech., **911**, A32, (2021).
- [52] D. Yang, M. Krasowska, C. Priest, M. N. Popescu, and J. Ralston, *Dynamics of capillary-driven flow in open microchannels*, J. Phys. Chem. C, **115**, 18761–18769, (2011).
- [53] Y. Chen, L. S. Melvin, S. Rodriguez, D. Bell, and M. M. Weislogel, *Capillary driven flow in micro scale surface structures*, Microelectron. Eng., **86**, 1317–1320, (2009).
- [54] J. Bico, C. Tordeux, and D. Quéré, *Rough wetting*, Europhys. Lett., **55**, 214, (2001).
- [55] C. Ishino, M. Reyssat, E. Reyssat, K. Okumura, and D. Quéré, *Wicking within forests of micropillars*, Europhys. Lett., **79**, 56005, (2007).
- [56] B. Darbois Texier, P. Laurent, S. Stoukatch, and S. Dorbolo, *Wicking through a confined micropillar array*, Microfluid. Nanofluid., **20**, 1–9, (2016).
- [57] F. Ferrero, *Wettability measurements on plasma treated synthetic fabrics by capillary rise method*, Polym. Test., **22**, 571–578, (2003).
- [58] J. C. Ramírez-Flores, J. Bachmann, and A. Marmur, *Direct determination of contact angles of model soils in comparison with wettability characterization by capillary rise*, J. Hydrol., **382**, 10–19, (2010).
- [59] H. Caps, S. Cox, H. Decauwer, D. Weaire, and N. Vandewalle, *Capillary rise in foams under microgravity*, Colloids Surf. A, **261**, 131–134, (2005).
- [60] M. Reyssat, L. Courbin, E. Reyssat, and H. A. Stone, *Imbibition in geometries with axial variations*, J. Fluid. Mech., **615**, 335–344, (2008).
- [61] J.-B. Gorce, I. J. Hewitt, and D. Vella, *Capillary imbibition into converging tubes: Beating Washburn’s law and the optimal imbibition of liquids*, Langmuir, **32**, 1560–1567, (2016).
- [62] A. Ponomarenko, D. Quéré, and C. Clanet, *A universal law for capillary rise in corners*, J. Fluid Mech., **666**, 146—154, (2011).

- [63] J. Zhou and M. Doi, *Universality of capillary rising in corners*, J. Fluid Mech., **900**, A29, (2020).
- [64] D. Deng, Y. Tang, J. Zeng, S. Yang, and H. Shao, *Characterization of capillary rise dynamics in parallel micro v-grooves*, Int. J. Heat Mass Transfer, **77**, 311–320, (2014).
- [65] J. Cai and B. Yu, *A discussion of the effect of tortuosity on the capillary imbibition in porous media*, Transp. Porous Media, **89**, 251–263, (2011).
- [66] N. Obara and K. Okumura, *Imbibition of a textured surface decorated by short pillars with rounded edges*, Phys. Rev. E, **86**, 020601, (2012).
- [67] S. Dorbolo, *The wetting properties of frosted glass*, Pap. Phys., **13**, 130006, (2021).
- [68] R. R. Rye, J. A. Mann, and F. G. Yost, *The flow of liquids in surface grooves*, Langmuir, **12**, 555–565, (1996).
- [69] T. Chen, *Capillary force-driven fluid flow in open grooves with different sizes*, J. Thermophys. Heat Transfer, **29**, 594–601, (2015).
- [70] P. B. Warren, *Late stage kinetics for various wicking and spreading problems*, Phys. Rev. E, **69**, 041601, (2004).
- [71] L. Courbin, E. Denieul, E. Dresseira, M. Roper, A. Ajdari, and H. A. Stone, *Imbibition by polygonal spreading on microdecorated surfaces*, Nature Mater., **6**, 661–664, (2007).
- [72] B. Carroll, *The accurate measurement of contact angle, phase contact areas, drop volume, and Laplace excess pressure in drop-on-fiber systems*, J. Colloid Interface Sci., **57**, 488–495, (1976).
- [73] G. McHale, M. I. Newton, and B. Carroll, *The shape and stability of small liquid drops on fibers*, Oil & Gas science and technology, **56**, 47–54, (2001).
- [74] G. McHale and M. Newton, *Global geometry and the equilibrium shapes of liquid drops on fibers*, Colloids Surf. A, **206**, 79–86, (2002).
- [75] T.-H. Chou, S.-J. Hong, Y.-E. Liang, H.-K. Tsao, and Y.-J. Sheng, *Equilibrium phase diagram of drop-on-fiber: coexistent states and gravity effect*, Langmuir, **27**, 3685–3692, (2011).
- [76] M. Amrei, M. Davoudi, G. Chase, and H. Vahedi Tafreshi, *Effects of roughness on droplet apparent contact angles on a fiber*, Sep. Purif. Technol., **180**, 107–113, (2017).
- [77] G. McHale, N. A. Käb, M. I. Newton, and S. M. Rowan, *Wetting of a high-energy fiber surface*, J. Colloid Interface Sci., **186**, 453–461, (1997).
- [78] B. J. Carroll, *Equilibrium conformations of liquid drops on thin cylinders under forces of capillarity. A theory for the roll-up process*, Langmuir, **2**, 248–250, (1986).

- [79] K. A. Brakke, *The surface evolver*, Experimental mathematics, **1**, 141–165, (1992).
- [80] E. Lorenceau, C. Clanet, and D. Quéré, *Capturing drops with a thin fiber*, J. Colloid Interface Sci., **279**, 192–197, (2004).
- [81] D. Quéré, *Fluid coating on a fiber*, Annu. Rev. Fluid Mech., **31**, 347–384, (1999).
- [82] S. Haefner, M. Benzaquen, O. Bäümchen, T. Salez, R. Peters, J. D. McGraw, K. Jacobs, E. Raphaël, and K. Dalnoki-Veress, *Influence of slip on the Plateau–Rayleigh instability on a fibre*, Nature Commun., **6**, 7409, (2015).
- [83] D. Quéré, *Thin films flowing on vertical fibers*, Europhys. Lett., **13**, 721, (1990).
- [84] S. Kalliadasis and H.-C. Chang, *Drop formation during coating of vertical fibres*, J. Fluid Mech., **261**, 135–168, (1994).
- [85] I. L. Kliakhandler, S. H. Davis, and S. G. Bankoff, *Viscous beads on vertical fibre*, J. Fluid Mech., **429**, 381–390, (2001).
- [86] R. V. Craster and O. K. Matar, *On viscous beads flowing down a vertical fiber*, J. Fluid Mech., **553**, 85–105, (2006).
- [87] A. Sadeghpour, Z. Zeng, and Y. S. Ju, *Effects of nozzle geometry on the fluid dynamics of thin liquid films flowing down vertical strings in the Rayleigh–Plateau regime*, Langmuir, **33**, 6292–6299, (2017).
- [88] C. T. Gabbard and J. B. Bostwick, *Scaling analysis of the Plateau-Rayleigh instability in thin film flow down a fiber*, Exp. Fluids, **62**, 141, (2021).
- [89] B. Guo and R. Liu, *The relative periodic orbit of liquid films flowing down a vertical fiber*, Microgravity Sci. Technol., **34**, 1–9, (2022).
- [90] C. Duprat, C. Ruyer-Quil, S. Kalliadasis, and F. Giorgiutti-Dauphiné, *Absolute and convective instabilities of a viscous film flowing down a vertical fiber*, Phys. Rev. Lett., **98**, 244502, (2007).
- [91] L. B. Smolka, J. North, and B. K. Guerra, *Dynamics of free surface perturbations along an annular viscous film*, Phys. Rev. E, **77**, 036301, (2008).
- [92] C. T. Gabbard and J. B. Bostwick, *Asymmetric instability in thin-film flow down a fiber*, Phys. Rev. Fluids, **6**, 034005, (2021).
- [93] C. T. Gabbard and J. B. Bostwick, *Thin film flow between fibers: Inertial sheets and liquid bridge patterns*, Phys. Rev. Fluids, **8**, 110505, (2023).
- [94] Q. Xie, R. Liu, X. Wang, and X. Chen, *Investigation of flow dynamics of thin viscous films down differently shaped fibers*, Appl. Phys. Lett., **119**, 201601, (2021).
- [95] A. Cazaubiel and A. Carlson, *Influence of wind on a viscous liquid film flowing down a thread*, Phys. Rev. Fluids, **8**, 054002, (2023).

- [96] C. Duprat, C. Ruyer-Quil, and F. Giorgiutti-Dauphiné, *Spatial evolution of a film flowing down a fiber*, Phys. Fluids, **21**, (2009).
- [97] Z. Huang, X. Liao, Y. Kang, G. Yin, and Y. Yao, *Equilibrium of drops on inclined fibers*, J. Colloid Interface Sci., **330**, 399–403, (2009).
- [98] T. Gilet, D. Terwagne, and N. Vandewalle, *Droplets sliding on fibres*, Eur. Phys. J. E, **31**, 253–262, (2010).
- [99] E. Lorenceau and D. Quéré, *Drops on a conical wire*, J. Fluid Mech., **510**, 29–45, (2004).
- [100] V. R. Kern and A. Carlson, *Twisted fibers enable drop flow control and enhance fog capture*, Proceedings of the National Academy of Sciences, **121**, e2402252121, (2024).
- [101] T. Gilet, D. Terwagne, and N. Vandewalle, *Digital microfluidics on a wire*, Appl. Phys. Lett., **95**, (2009).
- [102] F. Weyer, M. Lismont, L. Dreesen, and N. Vandewalle, *Compound droplet manipulations on fiber arrays*, Soft Matter, **11**, 7086–7091, (2015).
- [103] F. Weyer, A. Duchesne, and N. Vandewalle, *Switching behavior of droplets crossing nodes on a fiber network*, Sci. Rep., **7**, 13309, (2017).
- [104] A. Sauret, F. Boulogne, B. Soh, E. Dressaire, and H. A. Stone, *Wetting morphologies on randomly oriented fibers*, Eur. Phys. J. E, **38**, 1–9, (2015).
- [105] Z. Pan, F. Weyer, W. G. Pitt, N. Vandewalle, and T. T. Truscott, *Drop on a bent fibre*, Soft Matter, **14**, 3724–3729, (2018).
- [106] S. Protiere, C. Duprat, and H. A. Stone, *Wetting on two parallel fibers: drop to column transitions*, Soft Matter, **9**, 271–276, (2013).
- [107] C. Duprat, S. Protière, A. Y. Beebe, and H. A. Stone, *Wetting of flexible fibre arrays*, Nature, **482**, 510–513, (2012).
- [108] J. Bico, B. Roman, L. Moulin, and A. Boudaoud, *Elastocapillary coalescence in wet hair*, Nature, **432**, 690–690, (2004).
- [109] C. Py, R. Bastien, J. Bico, B. Roman, and A. Boudaoud, *3D aggregation of wet fibers*, Europhys. Lett., **77**, 44005, (2007).
- [110] H. K. Khattak, A. Shanzeela, E. Raphaël, and K. Dalnoki-Veress, *Directed droplet motion along thin fibers*, PNAS Nexus, **3**, 1–6, (2024).
- [111] C. Luo, X. Heng, and M. Xiang, *Behavior of a liquid drop between two non-parallel plates*, Langmuir, **30**, 8373–8380, (2014).
- [112] Y.-E. Liang, H.-K. Tsao, and Y.-J. Sheng, *Drops on hydrophilic conical fibers: Gravity effect and coexistent states*, Langmuir, **31**, 1704–1710, (2015).
- [113] X. Tan, T. Shi, Z. Tang, B. Sun, L. Du, Z. Peng, and G. Liao, *Investigation of fog collection on cactus-inspired structures*, J. Bionic Eng., **13**, 364–372, (2016).

- [114] C. Luo, *Theoretical exploration of barrel-shaped drops on cactus spines*, *Langmuir*, **31**, 11809–11813, (2015).
- [115] E. Q. Li and S. T. Thoroddsen, *The fastest drop climbing on a wet conical fibre*, *Phys. Fluids*, **25**, 052105, (2013).
- [116] T. S. Chan, C. Pedersen, J. Koplik, and A. Carlson, *Film deposition and dynamics of a self-propelled wetting droplet on a conical fibre*, *J. Fluid Mech.*, **907**, A29, (2021).
- [117] T. S. Chan, C. L. Lee, C. Pedersen, K. Dalnoki-Veress, and A. Carlson, *Film coating by directional droplet spreading on fibers*, *Phys. Rev. Fluids*, **6**, 014004, (2021).
- [118] C. Fournier, C. L. Lee, R. D. Schulman, É. Raphaël, and K. Dalnoki-Veress, *Droplet migration on conical fibers*, *Eur. Phys. J. E*, **44**, 1–6, (2021).
- [119] C. L. Lee, T. S. Chan, A. Carlson, and K. Dalnoki-Veress, *Multiple droplets on a conical fiber: formation, motion, and droplet mergers*, *Soft Matter*, **18**, 1364–1370, (2022).
- [120] S. Michielsen, J. Zhang, J. Du, and H. J. Lee, *Gibbs free energy of liquid drops on conical fibers*, *Langmuir*, **27**, 11867–11872, (2011).
- [121] J. McCarthy, D. Vella, and A. A. Castrejón-Pita, *Dynamics of droplets on cones : Self-propulsion due to curvature gradients*, *Soft Matter*, **15**, 9997–10004, (2019).
- [122] B. Hu, Z. Duan, B. Xu, K. Zhang, Z. Tang, C. Lu, M. He, L. Jiang, and H. Liu, *Ultrafast self-propelled directional liquid transport on the pyramid-structured fibers with concave curved surfaces*, *J. Am. Chem. Soc.*, **142**, 6111–6116, (2020).
- [123] Y. Li, Z. Cui, G. Li, H. Bai, R. Dai, Y. Zhou, Y. Jiao, Y. Song, Y. Yang, S. Liu, and M. Cao, *Directional and adaptive oil self-transport on a multi-bioinspired grooved conical spine*, *Adv. Funct. Mater.*, **32**, 2201035, (2022).
- [124] K. Lakra and K. Avishek, *A review on factors influencing fog formation, classification, forecasting, detection and impacts*, *Rendiconti Lincei. Scienze Fisiche e Naturali*, **33**, 319–353, (2022).
- [125] Y. Jiang, C. Machado, and K.-C. K. Park, *From capture to transport: a review of engineered surfaces for fog collection*, *Droplet*, **2**, e55, (2023).
- [126] F. T. Malik, R. M. Clement, D. T. Gethin, W. Krawczik, and A. R. Parker, *Nature’s moisture harvesters: a comparative review*, *Bioinspiration Biomimetics*, **9**, 031002, (2014).
- [127] A. Roth-Nebelsick, M. Ebner, T. Miranda, V. Gottschalk, D. Voigt, S. Gorb, T. Stegmaier, J. Sarsour, M. Linke, and W. Konrad, *Leaf surface structures enable the endemic Namib desert grass *Stipagrostis sabulicola* to irrigate itself with fog water*, *J. R. Soc. Interface*, **9**, 1965–1974, (2012).

- [128] T. E. Dawson, *Fog in the California redwood forest: ecosystem inputs and use by plants*, *Oecologia*, **117**, 476–485, (1998).
- [129] H. Chen, P. Zhang, L. Zhang, H. Liu, Y. Jiang, D. Zhang, Z. Han, and L. Jiang, *Continuous directional water transport on the peristome surface of *Nepenthes alata**, *Nature*, **532**, 85–89, (2016).
- [130] J. de Dios Rivera, *Aerodynamic collection efficiency of fog water collectors*, *Atmos. Res.*, **102**, 335–342, (2011).
- [131] O. Klemm, R. S. Schemenauer, A. Lummerich, P. Cereceda, V. Marzol, D. Corell, J. van Heerden, D. Reinhard, T. Gherezghiher, J. Olivier, P. Osses, J. Sarsour, E. Frost, M. J. Estrela, J. A. Valiente, and G. M. Fessehaye, *Fog as a fresh-water resource: Overview and perspectives*, *Ambio*, **41**, 221–234, (2012).
- [132] I. Langmuir and K. Blodgett, *A mathematical investigation of water droplet trajectories*. Army Air Forces Headquarters, Air Technical Service Command, (1946).
- [133] A. Moncuquet, A. Mitranescu, O. C. Marchand, S. Ramanananarivo, and C. Duprat, *Collecting fog with vertical fibres: combined laboratory and in-situ study*, *Atmos. Res.*, **277**, 106312, (2022).
- [134] W. Shi, M. J. Anderson, J. B. Tulkoff, B. S. Kennedy, and J. B. Boreyko, *Fog harvesting with harps*, *ACS Appl. Mater. Interfaces*, **10**, 11979–11986, (2018).
- [135] W. Shi, T. W. van der Sloot, B. J. Hart, B. J. Kennedy, and J. B. Boreyko, *Harps enable water harvesting under light fog conditions*, *Adv. Sust. Syst.*, **4**, 2000040, (2020).
- [136] N. G. Kowalski, W. Shi, B. S. Kennedy, and J. B. Boreyko, *Optimizing fog harps*, *ACS Appl. Mater. Interfaces*, **13**, 38826–38834, (2021).
- [137] R. Labbé and C. Duprat, *Capturing aerosol droplets with fibers*, *Soft Matter*, **15**, 6946–6951, (2019).
- [138] M. A. *et al.*, *Optimal design of multilayer fog collectors*, *ACS Appl. Mater. Interfaces*, **12**, 7736–7743, (2020).
- [139] J. Ju, K. Xiao, H. Bai, and L. Jiang, *Bioinspired conical copper wire with gradient wettability for continuous and efficient fog collection*, *Adv. Mater.*, **25**, 5937–5942, (2013).
- [140] H. Bai, T. Zhao, X. Wang, Y. Wu, K. Li, C. Yu, L. Jiang, and M. Cao, *Cactus kirigami for efficient fog harvesting: simplifying a 3D cactus into 2D paper art*, *J. Mater. Chem. A*, **8**, 13452–13458, (2020).
- [141] K. Zhang, H. Chen, T. Ran, L. Zhang, Y. Zhang, D. Chen, Y. Wang, Y. Guo, and G. Liu, *High-efficient fog harvest from a synergistic effect of coupling hierarchical structures*, *ACS Appl. Mater. Interfaces*, **14**, 33993–34001, (2022).

- [142] A. Olanrewaju, M. Beaugrand, M. Yafia, and D. Juncker, *Capillary microfluidics in microchannels: from microfluidic networks to capillarie circuits*, Lab Chip, **18**, 2323–2347, (2018).
- [143] M. M. Weislogel, *Some analytical tools for fluids management in space: Isothermal capillary flows along interior corners*, Adv. Space Res., **32**, 163–170, (2003).
- [144] J. Ha and H.-Y. Kim, *Capillarity in soft porous solids*, Annu. Rev. Fluid Mech., **52**, 263–284, (2020).
- [145] N. Kubochkin and T. Gambaryan-Roisman, *Capillary-driven flow in corner geometries*, Curr. Opin. Colloid Interface Sci., **59**, 101575, (2022).
- [146] M. Cao, J. Ju, K. Li, S. Dou, K. Liu, and L. Jiang, *Facile and large-scale fabrication of a cactus-inspired continuous fog collector*, Adv. Funct. Mater., **24**, 3235–3240, (2014).
- [147] M. Leonard, J. Van Hulle, F. Weyer, D. Terwagne, and N. Vandewalle, *Droplets sliding on single and multiple vertical fibers*, Phys. Rev. Fluids, **8**, 103601, (2023).
- [148] Y. Jiang, C. Machado, S. Savarirayan, N. A. Patankar, and K.-C. Park, *Onset time of fog collection*, Soft Matter, **15**, 6779–6783, (2019).
- [149] D. Quéré, J.-M. Di Meglio, and F. Brochard-Wyart, *Spreading of liquids on highly curved surfaces*, Science, **249**, 1256–1260, (1990).
- [150] L. Landau and B. Levich, *Dragging of a liquid by a moving plate*, in *Dynamics of Curved Fronts* (P. Pelcé, ed.), 141–153, San Diego: Academic Press, (1988).
- [151] K. Olsen and J. Bohr, *The generic geometry of helices and their close-packed structures*, Theor. Chem. Acc., **125**, 207–215, (2010).
- [152] J. M. Hanlan, G. E. Davis, and D. J. Durian, *Twist and measure: characterizing the effective radius of strings and bundles under twisting contraction*, Soft Matter, **19**, 4315–4322, (2023).
- [153] J. B. Segur and H. E. Oberstar, *Viscosity of glycerol and its aqueous solutions*, Ind. Eng. Chem., **43**, 2117–2120, (1951).
- [154] A. Sadeghpour, Z. Zeng, H. Ji, N. Dehdari Ebrahimi, A. L. Bertozzi, and Y. S. Ju, *Water vapor capturing using an array of traveling liquid beads for desalination and water treatment*, Sci. Adv., **5**, eaav7662, (2019).
- [155] H. Chinju, K. Uchiyama, and Y. H. Mori, *“String-of-beads” flow of liquids on vertical wires for gas absorption*, AIChE J., **46**, 937–945, (2000).
- [156] C. Lv, C. Chen, Y.-C. Chuang, F.-G. Tseng, Y. Yin, F. Grey, and Q. Zheng, *Substrate curvature gradient drives rapid droplet motion*, Phys. Rev. Lett., **113**, 026101, (2014).
- [157] C. A. Schneider, W. S. Rasband, and K. W. Eliceiri, *NIH Image to ImageJ: 25 years of image analysis*, Nature Methods, **9**, 671–675, (2012).

- [158] Y. Li, H. Wu, and F. Wang, *Stagnation of a droplet on a conical substrate determined by the critical curvature ratio*, J. Phys. D: Appl. Phys., **49**, 085304, (2016).
- [159] E. Ruiz-Gutiérrez, J. H. Guan, B. Xu, G. McHale, G. G. Wells, and R. Ledesma-Aguilar, *Energy invariance in capillary systems*, Phys. Rev. Lett., **118**, 218003, (2017).
- [160] E. Reyssat, *Drops and bubbles in wedges*, J. Fluid. Mech., **748**, 641–662, (2014).